The confinement and coherent generation of acoustic plasmons in photoexcited GaAs

by

Prashant Padmanabhan

A dissertation submitted in partial fulfillment
of the requirements for the degree of
Doctor of Philosophy
(Applied Physics)
in the University of Michigan
2014

Doctoral Committee:

Professor Roberto D. Merlin, Chair
Professor Roy Clarke
Professor Theodore B. Norris
Associate Professor Jennifer P. Ogilvie
Professor Roseanne J. Sension

If you can trust yourself when all men doubt you,
But make allowance for their doubting too;
. . .
If you can dream – and not make dreams your master;
If you can think – and not make thoughts your aim;
. . .
If you can fill the unforgiving minute
With sixty seconds' worth of distance run,
Yours is the Earth and everything that's in it,
And – which is more – you'll be a Man, my son!

– Rudyard Kiping

2014

To Mom and Dad

A C K N O W L E D G M E N T S

Over the past several years, I have relied upon the grace and wisdom of my coworkers, friends, and family. It seems unfathomable to sum up the enormity of their contributions to my life, both academic and personal, in a few short paragraphs, but I shall still endeavor to do so. I would like to begin by thanking Dr. Roberto Merlin for advising me over the last several years. He is both a brilliant physicist and committed educator. I thank him for always being available to patiently answer my questions, be they academic or existential, and for also teaching me how to adeptly wield the language of physics. I would like to also thank the members of my defense committee: Dr. Jennifer Ogilvie, Dr. Roseanne Sension, Dr. Theodore Norris, and Dr. Roy Clarke with whom I enjoyed discussing not only my research, but also Indian, Australian, and British cricket.

I also owe a great many thanks to Meredith Henstridge and Steve Young for their invaluable assistance with the experimental and theoretical aspects of this research. Further, I would like to recognize some past and present members of the Merlin group, including Alex Toulouse for helping to keep the spectrometers running, Ibrahim Boulares for insightful discussions on Raman scattering and Eastern culture, Andrea Bianchini and Jingjing Li for introducing me to pump-probe spectroscopy, and Ilya Vugmeyster for guiding me during my time in the Merlin Group. I would also like to extend my thanks to Steve Katnik for his assistance with all things laser-related, and Dr. Sishir Bhowmick and Dr. Pallab K. Bhattacharya for preparing the samples used in my research.

My friends have played a pivotal role, not just in my development as a student of physics, but also as a person. These words are dedicated to them. I met Pratik Rohatgi on my first day of undergrad at Michigan, and am a better person for it. I would like to

thank him for being like a brother to me, for listening when I was down, celebrating triumphs, and for his invaluable guidance when I needed it most. Channing Huntington has been an amazing friend and confidant over the last several years. I thank him for helping me to push past my own boundaries, fostering my sense of adventure, and introducing me to many of the life experiences that I will forever cherish. Jeffrey Herbstman is a person who has infused so much culture into my life during my time in graduate school. I am also grateful for his kindness, friendship, and sage advice that helped me through many a challenging time. Marc Witcher has been a truly wonderful friend since I met him during my first year of graduate school. Since that time, he has been a part of so many of my happiest memories of Ann Arbor. I thank him for always being willing to trade ridiculous stories, the ABC nights, and for his unwavering loyalty and support. Alexis Toulouse has wonderfully fulfilled the role of both labmate and friend. He is easily the most honest person I know and his insightful observations about my person have helped me to better understand and improve myself. I will miss our afternoon coffee sessions oh so much. Meredith Henstridge is simply an amazing person. She has not only been absolutely vital in the experimental aspects of this research, but also helped to bolster my confidence when it waned. I truly enjoyed our overnight data collection sessions, TNG marathons, and visits to the Aut. David Anderson always knows how to cheer me up. He helped me keep balance when the weight of graduate school threatened to shift the scales. Thank you for always giving me another perspective when I needed it most. Jessica Ames is the queen of the OPA and one of the most interesting people I will ever know. I am indebted to her for teaching me about lasers, mode-locking, and all things outdoors. I will greatly miss our Tuesday Taco nights and her superb company. Will Fisher and Meredith Brenner have been wonderful friends. I greatly enjoyed their fun game nights and potlucks, and have benefited from their prudent advice over the years. Charles Sutton, in my opinion, is the heart of the Applied Physics Program. Since my first day of graduate school, he has been a wonderful source of personal advice, football discussions, and all-around friendship. I will always look back fondly upon our

long chats in the AP office and summer coffee breaks on the stoop of Randall Lab. And finally, Jared Cantor, one of my oldest and dearest friends. I met him in Sophomore year of high school and from that moment, he has been the most caring and dependable person I could ever hope to know. I thank him for sharing so many of the milestones of my life and look forward to sharing many more.

The last of my acknowledgements is both the most important to me and the hardest to write. My family deserves more credit and gratitude than it seems possible to express with mere words. To Mummy's Mummy, Ravi Mama, Sudha Auntie, Usha Auntie, Amin Uncle, and Supriya: though we have always lived far apart, I thank you for always supporting me and keeping me in your prayers. I would also like to thank Karthik Padmanabhan for his ever-present love and support. Though he is my younger brother, over the years, he has demonstrated a wisdom far beyond his age and has always been there for me when I needed him most. Lastly, I wish to thank my parents. I am forever indebted to my father, Karur R. Padmanabhan. The time he invested in me, teaching me about science, taking me to his lab, reading to me from astronomy books as a child, and providing me with every opportunity a son could hope for are the reasons I became a scientist. And to my mother, Suguna Padmanabhan, who did everything a mother can do to nurture a child towards maturity. She has provided me with comfort and strength, and continues to be a spring of unconditional love and support. To my parents, I offer this work as a humble token of my immeasurable gratitude and love for their unending commitment to my future.

TABLE OF CONTENTS

LIST OF FIGURES

LIST OF APPENDICES

CHAPTER 1

Introduction

Physicists have long sought to come to terms with the nature of interactions between light and matter. In 1928, Chandrasekar V. Raman introduced a veritable revolution in the field when he demonstrated that sunlight could scatter inelastically from molecular vibrations in liquids [1]. Today, sophisticated laser sources and spectrometers capable of measuring fractions of a nanometer have allowed Raman's early methods to be refined into the spectroscopic techniques that are now the state-of-the-art in the analysis of the vibrational and electronic properties of gasses, liquids, and solids. We now have the ability to study the optical properties of materials in unprecedented detail, and are able to probe new phenomena with greater precision.

Bulk semiconductors are systems that are particularly well-suited to study with light scattering methods. The lattice dynamics of many semiconducting materials have been investigated in great detail using a variety of light scattering techniques. A particularly interesting system involves semiconductors with large carrier densities introduced via doping or photoexcitation. In both these cases, the carrier density can be controlled, and at large values, plasma effects become important and can manifest as new excitations in the system. Coulomb interactions between the carriers introduce collective phenomena which manifests as quantized longitudinal oscillations of the plasma known as optical plasmons. The properties of optical plasmons and their interactions with lattice oscillations in semiconductors have been extensively studied using both CW and ultrafast scattering techniques

(see for example [2, 3, 4, 5, 6, 7, 8, 9]).

The existence of multiple distinct charge species in a plasma, as is the the case for photexcited semiconductors, has a profound impact on the plasma excitations present within the system. Here, the intraspecies Coulomb effects are supplemented by interactions between the different charge species. As first postulated by Nozières and Pines [10], in certain cases, a strong screening of the Coulomb interaction can lead to a second type of collective phenomenon known as acoustic plasmons. These possess a linear dispersion, in contrast to the parabolically dispersed optical branch [11]. Theoretical work on high-T_c superconductors has shown that acoustic plasmons may mediate electron-electron interactions in these materials [12]. This aspect has been extensively studied by Ruvalds and coworkers in transition metal compounds [13, 11, 14]. In addition, acoustic plasmons are also thought to play a role in the superconductivity associated with layered materials [15, 16, 17, 18].

Light scattering from acoustic plasmons in a semiconductor was first demonstrated by Pinczuk et al. in the 1980s using spontaneous inelastic light scattering in GaAs [19]. They were able to show not only the excitation of the low energy acoustic plasmon, but also that experimental observations matched theoretical predictions calculated under the random phase approximation for a multi-component plasma. The success of these experiments was a remarkable achievement given the difficulties associated with the analysis of low energy excitations obscured by elastic scattering, resonance effects, and band-gap luminescence. More recently, the presence of acoustic plasmons has been demonstrated experimentally in metallic and low dimensional systems [20, 21, 22, 23], but here the excitations fundamentally differ from the bulk case [24], and involve screening of the surface electron state by the bulk electrons. To this day, bulk acoustic plasmons in semiconductors remain an elusive excitation, and a detailed analysis of their properties, particularly within the context of the supporting medium's geometry, merits further investigation. Furthermore, despite extensive research into the ultrafast excitation of semiconducting materials, coherent acoustic plasmon states have yet to be identified.

The aim of this dissertation is to provide new insights into the nature of acoustic plasmons in semiconductors, and address not only the properties of this excitation under confinement, but also to show that they can be coherently generated using pump-probe techniques. Beginning with a simple model of the two component plasma under the Drude and Thomas-Fermi approximations, I will present a full treatment of the problem under the random phase approximation (Chapter II). I will also discuss the effect of band structure subtleties on the acoustic plasmon properties. Further, using the fluid-description of the electron-hole plasma, I will show that when the plasma is confined to a finite slab, the acoustic plasmon exists as discretized standing waves. I have experimentally validated this theory using spontaneous light scattering, which shows that the acoustic plasmon spectral peak frequency possesses a thickness dependence characteristic of confinement effects (Chapter V). The coupling of light to these acoustic plasmon standing waves can be explained under the framework of the photoelastic model. Here the strain wave that accompanies the density fluctuation associated with the acoustic plasmon mode can mix with the incident light field to generate a nonlinear polarization. The relative intensities of the resulting scattered fields correspond to the scattering efficiency of a given acoustic plasmon mode. The experimental acoustic plasmon spectra is then theoretically reproduced as the weighted superposition of contributions from several standing wave modes. The success of this model, which is also used to describe light scattering from confined LA phonons, further solidifies the analogy between acoustic plasmons and longitudinal acoustic (LA) phonons. I have also investigated the properties of the acoustic plasmon in the time-domain using ultrafast pump-probe spectroscopy, where I generated a coherent acoustic plasmon state using an entirely optical technique (Chapter VI). This state exists as a discrete standing wave mode, in agreement with the spontaneous scattering experiments. In addition, the results reveal that the coherent acoustic plasmon is coupled to the lower frequency branch of the coherent LO phonon-plasmon coupled mode, and this can serve as a possible generation mechanism.

The importance of the experimental results contained within this dissertation are multifold. In a general sense, they add to the body of knowledge associated with bulk acoustic plasmons, and this may better allow for the assessment of their role in phenomena such as superconductivity. Further, heat conduction in semiconductors is associated with sound waves and, in general, with the acoustic phonons of the system [25]. However, the observation of a coherent acoustic plasmon state represents a fundamentally new type of sound wave that can be supported by the semiconductor. This is particularly intriguing as the group velocity of the acoustic plasmon is more than an order of magnitude larger than that associated with the LA phonon. This may then prove to be a pathway for more efficient heat transfer in semiconducting materials.

CHAPTER 2

Theory of acoustic plasmons

We can analyze the properties of both optical and acoustic plasmons in semiconductors by looking at the longitudinal dielectric function associated with the system. In order to do this, we must first construct the longitudinal dielectric function of a multi-component semiconductor plasma. The simplest way to do this is to use the framework of the Drude and Thomas-Fermi models. This is a limiting approximation and a more complex treatment begins with the Hamiltonian of the electron-hole plasma, from which we construct the dielectric function using the constituent susceptibilities associated with the various carrier species. In this chapter, I will begin by explaining the relationship between the dielectric function and plasmons and then present the simple treatment before discussing the microscopic theory of acoustic plasmons. I will conclude by discussing the form of the charge density fluctuations associated with the acoustic plasmons.

2.1 Plasmons and the dielectric function

Both optical and acoustic plasmons are essentially collective oscillations of the plasma system, and more specifically, they represent fluctuations about the mean plasma density. We can ascertain the properties of both optical and acoustic plasmons from the longitudinal dielectric function of the plasma system. Consider an electron gas in which we embed a weak external charge. Let this external charge be Z and the density be $n_{ext}\left(\mathbf{r},t\right)$. Then, the

charge density is simply $Zn_{ext}(\mathbf{r},t)$. From Maxwell's equations in media, we can write: [26]

$$\begin{aligned}
\nabla\cdot\mathbf{E}(\mathbf{r},t) = 4\pi\left[-e\left\langle n(\mathbf{r},t)\right\rangle\right. &\xrightarrow{\mathscr{F}} i\mathbf{k}\cdot\mathbf{E}(\mathbf{k},\omega) = 4\pi\left[-e\left\langle n(\mathbf{k},\omega)\right\rangle\right. \\
\left.+Zn_{ext}(\mathbf{r},t)\right] &\qquad\quad \left.+Zn_{ext}(\mathbf{k},\omega)\right] \qquad (2.1)\\
\nabla\cdot\mathbf{D}(\mathbf{r},t) = 4\pi Zn_{ext}(\mathbf{r},t) &\xrightarrow{\mathscr{F}} i\mathbf{k}\cdot\mathbf{D}(\mathbf{k},\omega) = 4\pi Zn_{ext}(\mathbf{k},\omega) \qquad (2.2)\\
\mathbf{E}(\mathbf{r},t) = -\nabla\phi(\mathbf{r},t) &\xrightarrow{\mathscr{F}} \mathbf{E}(\mathbf{k},\omega) = -i\mathbf{k}\phi(\mathbf{k},\omega) \qquad (2.3)\\
-\nabla^2\phi_{ext}(\mathbf{r},t) = 4\pi Zn_{ext}(\mathbf{r},t) &\xrightarrow{\mathscr{F}} k^2\phi_{ext}(\mathbf{k},\omega) = 4\pi Zn_{ext}(\mathbf{k},\omega)\,. \qquad (2.4)
\end{aligned}$$

In essence, the Fourier transform of the electric field is proportional to the Fourier transform of the external charge density and the expectation value of the electron plasma density fluctuation. In contrast, the displacement field is only proportional to the external charge density. Now, a spatio-temporally varying dielectric function leads to the relation

$$\mathbf{D}(\mathbf{k},\omega) = \epsilon(\mathbf{k},\omega)\,\mathbf{E}(\mathbf{k},\omega)\,. \qquad (2.5)$$

If we take $\mathbf{E}$ and $\mathbf{D}$ to be longitudinal ($\mathbf{E},\mathbf{D}\|\mathbf{k}$) and insert Equations (2.1) and (2.2) into (2.5), we obtain

$$\frac{1}{\epsilon(\mathbf{k},\omega)} - 1 = \frac{-e\left\langle n(\mathbf{k},\omega)\right\rangle}{Z\rho_{ext}(\mathbf{k},\omega)}. \qquad (2.6)$$

Inserting Equations (2.3) into (2.1) and using (2.6) gives us an equivalent form for the dielectric function, namely

$$\epsilon(\mathbf{k},\omega) - 1 = \frac{4\pi e}{k^2}\frac{\left\langle n(\mathbf{k},\omega)\right\rangle}{\phi(\mathbf{k},\omega)}. \qquad (2.7)$$

Equation (2.6) reveals that if $\epsilon = 0$, a vanishingly small perturbation ($\phi_{ext} \to 0$) will still yield a non-zero value for the density fluctuation. This is the condition for the existence of a plasmon. By finding the zeros of the dielectric function at various values of $\mathbf{k}$ and ω,

we can obtain the dispersion of the plasmon. For a single component plasma, the plasmon frequency has a quadratic dispersion. However, for a multi-component plasma, we will find that the screening of Coulomb interactions leads to a second root of ϵ that has an acoustic character.

2.2 A simple look at acoustic plasmons

A straight-forward way to find an expression for the dielectric function of a two-component plasma is to invoke the random phase approximation (RPA). As I will show in the following section, the RPA allows us to write the longitudinal dielectric function as the sum of the susceptibilities associated with the two charge species. The additional term in the dielectric function due to the second species has a profound impact on the collective oscillations of the plasma system. We find that in addition to the quadratically dispersed optical branch, a second branch emerges due to the interaction between the two charge species [11].

Let us consider a two-component plasma system where the two species have drastically different masses ($m_1 \ll m_2$). In this case, we can treat species 1 under the Thomas-Fermi approximation as they quasi-statically screen the Coulomb interactions between species 2 [11, 2]. We treat the second species in the dynamic limit using the Drude model. Then, the total dielectric function of the system under the RPA is given by [11]

$$\epsilon_{RPA}\left(\mathbf{k},\omega\right) = 1 - \frac{\omega_2^2}{\omega^2} + \frac{k_{TF,1}^2}{k^2}, \tag{2.8}$$

where $\omega_2 = \sqrt{4\pi n_2 e^2/m_2}$ is the plasma frequency of species 2, and $k_{TF,1} = \sqrt{3\omega_1^2/v_{F1}^2}$ is the Thomas-Fermi screening wave vector of species 1, where v_F and ω_1 are its Fermi velocity and plasma frequency, respectively. Setting $\epsilon_{RPA} = 0$ and taking the limit when k is small yields

$$\omega_{AP}\left(\mathbf{k}\right) = \frac{\omega_2}{k_{TF,1}}k. \tag{2.9}$$

This is the dispersion relation for the acoustic plasmon, and as expected it is linear in k with $\omega_{AP} \to 0$ as $k \to 0$.

2.3 Microscopic theory of acoustic plasmons

In deriving Equation (2.8), we have bypassed a great deal of subtlety by using the Drude and Thomas-Fermi approximations. Thus, even though we obtain a qualitative understanding of how the acoustic plasmon emerges, any calculations of properties would far too approximate to make meaningful comparisons to experiments. As I will discuss in subsequent chapters, the composition of the plasma, particularly the density, damping, temperature, and energy dispersion of the various species all have a profound effects on the properties of the acoustic plasmon. We therefore need to go beyond this simple description and develop a theory that allows us to incorporate the interplay of these parameters. To do this, we will begin by using the Hamiltonian of a single-component plasma to obtain the expression for the RPA susceptibility of the plasma species and the longitudinal dielectric function. We can then extend this treatment to the case of a two-component plasma. The procedure I will present follows the derivation by Bohm and Pines in the formalism of second quantization [27].

2.3.1 RPA χ and ϵ for a single-component plasma

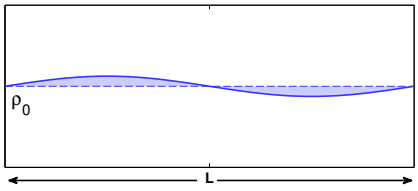

Figure 2.1: Schematic of a charge density fluctuation with $k = 2\pi/L$.

The main approach in deriving the susceptibility and dielectric function under the RPA will center on finding the expression for $\langle n(\mathbf{k},\omega)\rangle$ in Equation (2.7). To begin, let us consider an electron plasma with Coulomb interactions between the charge carriers and an added external time-varying potential. For the moment, we will disregard the spin of the electrons. The Hamiltonian for the system is given by

$$H = \sum_{\mathbf{p}} E(\mathbf{p})\, c^{\dagger}_{\mathbf{p}} c_{\mathbf{p}} + \sum_{\mathbf{k}',\mathbf{q},\mathbf{q}'} \left[\frac{V_{k'}}{2} c^{\dagger}_{\mathbf{q}-\mathbf{k}'} c^{\dagger}_{\mathbf{q}'+\mathbf{k}'} c_{\mathbf{q}'} c_{\mathbf{q}} - e n^{\dagger}_{\mathbf{k}} \phi_{ext}(\mathbf{k},\omega)\, e^{-i\omega t} e^{\delta t} + c.c \right]. \tag{2.10}$$

Here, $c_{\mathbf{k}}$ ($c^{\dagger}_{\mathbf{k}}$) is the annihilation (creation) operator for an electron in state $\mathbf{k}$, $V_{\mathbf{k}} = 4\pi e^2/k^2$, δ is an infinitesimal positive quantity that ensures the external perturbation is adiabatic, and $n_{\mathbf{k}} = \sum_{\mathbf{p}} c^{\dagger}_{\mathbf{p}} c_{\mathbf{p}+\mathbf{k}}$ is the density fluctuation operator. For $\mathbf{k} = 0$, n_0 simply represents the average density of electrons in the system. For $\mathbf{k} \neq 0$, we can interpret $n_{\mathbf{k}}$ by considering a box of electrons with average density n_0 and length L. If, for example, $k = 2\pi/L$, n_k represents a density fluctuation such as the one pictured in Figure 2.1, and essentially measures a quantity equivalent to the amplitude of the fluctuation. The first two terms on the right hand side of Equation (2.10) correspond to the kinetic and Coulomb interaction energy of the electrons. The third term describes the energy associated with the interactions between the electrons and the external potential. We obtain this term as follows:

$$\begin{aligned}
H_{int,ext} &= e \int d^3 r n(\mathbf{r})\, \phi_{ext}(\mathbf{r}) \\
&= e \int d^3 r \left[\int d^3 q e^{i\mathbf{q}\cdot\mathbf{r}} n_{\mathbf{q}} \right] \left[\int d^3 k e^{i\mathbf{k}\cdot\mathbf{r}} \phi_{ext}(\mathbf{k}) \right] \\
&= e \int d^3 k \phi_{ext}(\mathbf{k}) \int d^3 q n_{\mathbf{q}} \int d^3 r e^{i(\mathbf{k}+\mathbf{q})\cdot\mathbf{r}} \\
&= e \int d^3 k \phi_{ext}(\mathbf{k}) \int d^3 q n_{\mathbf{q}} \delta(\mathbf{k}+\mathbf{q}) \\
&= e \int d^3 k n^{\dagger}_{\mathbf{k}} \phi_{ext}(\mathbf{k}) \\
&= e \sum_{\mathbf{k}} n^{\dagger}_{\mathbf{k}} \phi_{ext}(\mathbf{k}).
\end{aligned} \tag{2.11}$$

In writing Equation (2.10), we have chosen the external potential to be harmonic in both space and time.

In order to determine the form of $\langle n(\mathbf{k},\omega)\rangle$, we must calculate the equation of motion of $n_{\mathbf{k}}$ by forming the commutator with the Hamiltonian. We can break the relevant commutator into 4 parts, each corresponding to one of the terms on the right hand side of Equation (2.10), and evaluate them as

$$\begin{aligned}
\left[c_{\mathbf{p}}^{\dagger}c_{\mathbf{p}+\mathbf{k}},\sum_{\mathbf{p}'}\frac{\hbar^2p'^2}{2m_e}c_{\mathbf{p}'}^{\dagger}c_{\mathbf{p}'}\right] &= \sum_{\mathbf{p}'}E\left(\mathbf{p}'\right)c_{\mathbf{p}}^{\dagger}c_{\mathbf{p}+\mathbf{k}}c_{\mathbf{p}'}^{\dagger}c_{\mathbf{p}'}-\sum_{\mathbf{p}'}E\left(\mathbf{p}'\right)c_{\mathbf{p}'}^{\dagger}c_{\mathbf{p}'}c_{\mathbf{p}}^{\dagger}c_{\mathbf{p}+\mathbf{k}}\\
&= \sum_{\mathbf{p}'}E\left(\mathbf{p}'\right)c_{\mathbf{p}}^{\dagger}\left(\delta_{\mathbf{p}+\mathbf{k},\mathbf{p}'}-c_{\mathbf{p}'}^{\dagger}c_{\mathbf{p}+\mathbf{k}}\right)c_{\mathbf{p}'}-\sum_{\mathbf{p}'}E\left(\mathbf{p}'\right)c_{\mathbf{p}'}^{\dagger}\left(\delta_{\mathbf{p},\mathbf{p}'}-c_{\mathbf{p}}^{\dagger}c_{\mathbf{p}'}\right)c_{\mathbf{p}+\mathbf{k}}\\
&= E\left(\mathbf{p}+\mathbf{k}\right)c_{\mathbf{p}}^{\dagger}c_{\mathbf{p}+\mathbf{k}}-E\left(\mathbf{p}\right)c_{\mathbf{p}}^{\dagger}c_{\mathbf{p}+\mathbf{k}}\\
&\quad -\sum_{\mathbf{p}'}E\left(\mathbf{p}'\right)c_{\mathbf{p}}^{\dagger}c_{\mathbf{p}'}^{\dagger}c_{\mathbf{p}+\mathbf{k}}c_{\mathbf{p}'}+\sum_{\mathbf{p}'}E\left(\mathbf{p}'\right)c_{\mathbf{p}}^{\dagger}c_{\mathbf{p}'}^{\dagger}c_{\mathbf{p}+\mathbf{k}}c_{\mathbf{p}'}\\
&= \left[E\left(\mathbf{p}+\mathbf{k}\right)-E\left(\mathbf{p}\right)\right]c_{\mathbf{p}}^{\dagger}c_{\mathbf{p}+\mathbf{k}}, \qquad (2.12)
\end{aligned}$$

$$\begin{aligned}
\left[c_{\mathbf{p}}^{\dagger}c_{\mathbf{p}+\mathbf{k}},-en_{\mathbf{k}}^{\dagger}\phi_{ext}\left(\mathbf{k},\omega\right)e^{-i\omega t}e^{\delta t}\right] &= \left[c_{\mathbf{p}}^{\dagger}c_{\mathbf{p}+\mathbf{k}},-e\sum_{\mathbf{p}'}c_{\mathbf{p}'}^{\dagger}c_{\mathbf{p}'-\mathbf{k}}\phi_{ext}\left(\mathbf{k},\omega\right)e^{-i\omega t}e^{\delta t}\right]\\
&= -e\left[c_{\mathbf{p}}^{\dagger}c_{\mathbf{p}+\mathbf{k}},\sum_{\mathbf{p}'}c_{\mathbf{p}'}^{\dagger}c_{\mathbf{p}'-\mathbf{k}}\right]\phi_{ext}\left(\mathbf{k},\omega\right)e^{-i\omega t}e^{\delta t}\\
&= -e\left\{\sum_{\mathbf{p}'}c_{\mathbf{p}}^{\dagger}c_{\mathbf{p}+\mathbf{k}}c_{\mathbf{p}'}^{\dagger}c_{\mathbf{p}'-\mathbf{k}}-\sum_{\mathbf{p}'}c_{\mathbf{p}'}^{\dagger}c_{\mathbf{p}'-\mathbf{k}}c_{\mathbf{p}}^{\dagger}c_{\mathbf{p}+\mathbf{k}}\right\}\phi_{ext}\left(\mathbf{k},\omega\right)e^{-i\omega t}e^{\delta t}\\
&= -e\left\{\sum_{\mathbf{p}'}c_{\mathbf{p}}^{\dagger}\left(\delta_{\mathbf{p}',\mathbf{p}+\mathbf{k}}-c_{\mathbf{p}'}^{\dagger}c_{\mathbf{p}+\mathbf{k}}\right)c_{\mathbf{p}'-\mathbf{k}}-\sum_{\mathbf{p}'}c_{\mathbf{p}'}^{\dagger}\left(\delta_{\mathbf{p}'-\mathbf{k},\mathbf{p}}-c_{\mathbf{p}}^{\dagger}c_{\mathbf{p}'-\mathbf{k}}\right)c_{\mathbf{p}+\mathbf{k}}\right\}\\
&\quad \times\phi_{ext}\left(\mathbf{k},\omega\right)e^{-i\omega t}e^{\delta t}\\
&= -e\left\{\sum_{\mathbf{p}'}c_{\mathbf{p}}^{\dagger}c_{\mathbf{p}'-\mathbf{k}}\delta_{\mathbf{p}',\mathbf{p}+\mathbf{k}}-c_{\mathbf{p}}^{\dagger}c_{\mathbf{p}'}^{\dagger}c_{\mathbf{p}+\mathbf{k}}c_{\mathbf{p}'-\mathbf{k}}\right.\\
&\quad \left.-\sum_{\mathbf{p}'}c_{\mathbf{p}'}^{\dagger}c_{\mathbf{p}+\mathbf{k}}\delta_{\mathbf{p}'-\mathbf{k},\mathbf{p}}-c_{\mathbf{p}'}^{\dagger}c_{\mathbf{p}}^{\dagger}c_{\mathbf{p}'-\mathbf{k}}c_{\mathbf{p}+\mathbf{k}}\right\}\phi_{ext}\left(\mathbf{k},\omega\right)e^{-i\omega t}e^{\delta t}\\
&= -\left\{c_{\mathbf{p}}^{\dagger}c_{\mathbf{p}}-c_{\mathbf{p}+\mathbf{k}}^{\dagger}c_{\mathbf{p}+\mathbf{k}}\right\}e\phi_{ext}\left(\mathbf{k},\omega\right)e^{-i\omega t}e^{\delta t}, \qquad (2.13)
\end{aligned}$$

$$\begin{aligned}
\left[c^\dagger_{\mathbf{p}}c_{\mathbf{p}+\mathbf{k}}, -en_{\mathbf{k}}\phi^\dagger_{ext}\left(\mathbf{k},\omega\right)e^{i\omega t}e^{\delta t}\right] &= \left[c^\dagger_{\mathbf{p}}c_{\mathbf{p}+\mathbf{k}}, -e\sum_{\mathbf{p}'}c^\dagger_{\mathbf{p}'}c_{\mathbf{p}'+\mathbf{k}}\phi^\dagger_{ext}\left(\mathbf{k},\omega\right)e^{i\omega t}e^{\delta t}\right] \\
&= -e\left[c^\dagger_{\mathbf{p}}c_{\mathbf{p}+\mathbf{k}}, \sum_{\mathbf{p}'}c^\dagger_{\mathbf{p}'}c_{\mathbf{p}'+\mathbf{k}}\right]\phi^\dagger_{ext}\left(\mathbf{k},\omega\right)e^{i\omega t}e^{\delta t} \\
&= -e\left\{\sum_{\mathbf{p}'}c^\dagger_{\mathbf{p}}c_{\mathbf{p}+\mathbf{k}}c^\dagger_{\mathbf{p}'}c_{\mathbf{p}'+\mathbf{k}} - \sum_{\mathbf{p}'}c^\dagger_{\mathbf{p}'}c_{\mathbf{p}'+\mathbf{k}}c^\dagger_{\mathbf{p}}c_{\mathbf{p}+\mathbf{k}}\right\}\phi^\dagger_{ext}\left(\mathbf{k},\omega\right)e^{i\omega t}e^{\delta t} \\
&= -e\left\{\sum_{\mathbf{p}'}c^\dagger_{\mathbf{p}}\left(\delta_{\mathbf{p}',\mathbf{p}+\mathbf{k}} - c^\dagger_{\mathbf{p}'}c_{\mathbf{p}+\mathbf{k}}\right)c_{\mathbf{p}'+\mathbf{k}}\right. \\
&\qquad \left. -\sum_{\mathbf{p}'}c^\dagger_{\mathbf{p}'}\left(\delta_{\mathbf{p}'+\mathbf{k},\mathbf{p}} - c^\dagger_{\mathbf{p}}c_{\mathbf{p}'+\mathbf{k}}\right)c_{\mathbf{p}+\mathbf{k}}\right\}\phi^\dagger_{ext}\left(\mathbf{k},\omega\right)e^{i\omega t}e^{\delta t} \\
&= -e\left\{\sum_{\mathbf{p}'}c^\dagger_{\mathbf{p}}c_{\mathbf{p}'+\mathbf{k}}\delta_{\mathbf{p}',\mathbf{p}+\mathbf{k}} - c^\dagger_{\mathbf{p}}c^\dagger_{\mathbf{p}'}c_{\mathbf{p}+\mathbf{k}}c_{\mathbf{p}'+\mathbf{k}}\right. \\
&\qquad \left. -\sum_{\mathbf{p}'}c^\dagger_{\mathbf{p}'}c_{\mathbf{p}+\mathbf{k}}\delta_{\mathbf{p}'+\mathbf{k},\mathbf{p}} - c^\dagger_{\mathbf{p}'}c^\dagger_{\mathbf{p}}c_{\mathbf{p}'+\mathbf{k}}c_{\mathbf{p}+\mathbf{k}}\right\}\phi^\dagger_{ext}\left(\mathbf{k},\omega\right)e^{i\omega t}e^{\delta t} \\
&= -\left\{c^\dagger_{\mathbf{p}}c_{\mathbf{p}+2\mathbf{k}} - c^\dagger_{\mathbf{p}-\mathbf{k}}c_{\mathbf{p}+\mathbf{k}}\right\}e\phi^\dagger_{ext}\left(\mathbf{k},\omega\right)e^{i\omega t}e^{\delta t}, \qquad (2.14)
\end{aligned}$$

and the contribution due to the interaction term (which requires a bit more perseverance)

$$\begin{aligned}
\left[c^\dagger_{\mathbf{p}}c_{\mathbf{p}+\mathbf{k}}, \sum_{\mathbf{k}',\mathbf{q},\mathbf{q}'}\frac{V_{k'}}{2}c^\dagger_{\mathbf{q}-\mathbf{k}'}c^\dagger_{\mathbf{q}'+\mathbf{k}'}c_{\mathbf{q}'}c_{\mathbf{q}}\right] &= \left[c^\dagger_{\mathbf{n}-\mathbf{k}}c_{\mathbf{n}}, \sum_{\mathbf{k}',\mathbf{q},\mathbf{q}'}\frac{V_{k'}}{2}c^\dagger_{\mathbf{q}-\mathbf{k}'}c^\dagger_{\mathbf{q}'+\mathbf{k}'}c_{\mathbf{q}'}c_{\mathbf{q}}\right] \\
&= \sum_{\mathbf{k}',\mathbf{q},\mathbf{q}'}\frac{V_{k'}}{2}\left\{c^\dagger_{\mathbf{n}-\mathbf{k}}c_{\mathbf{n}}c^\dagger_{\mathbf{q}-\mathbf{k}'}c^\dagger_{\mathbf{q}'+\mathbf{k}'}c_{\mathbf{q}'}c_{\mathbf{q}} + c^\dagger_{\mathbf{q}-\mathbf{k}'}c^\dagger_{\mathbf{q}'+\mathbf{k}'}c_{\mathbf{q}'}c_{\mathbf{q}}c^\dagger_{\mathbf{n}-\mathbf{k}}c_{\mathbf{n}}\right\} \\
&= -\sum_{\mathbf{k}',\mathbf{q}'}V_{k'}\left\{c^\dagger_{\mathbf{n}-\mathbf{k}}c^\dagger_{\mathbf{q}'-\mathbf{k}'}c_{\mathbf{n}-\mathbf{k}'}c_{\mathbf{q}'} + c^\dagger_{\mathbf{n}-\mathbf{k}-\mathbf{k}'}c^\dagger_{\mathbf{q}'+\mathbf{k}'}c_{\mathbf{q}'}c_{\mathbf{n}}\right\}. \qquad (2.15)
\end{aligned}$$

Making the change of variables $\mathbf{n} = \mathbf{p} + \mathbf{k}$, we obtain

$$\begin{aligned}
&\left[c^{\dagger}_{\mathbf{p}}c_{\mathbf{p}+\mathbf{k}}, \sum_{\mathbf{k}',\mathbf{q},\mathbf{q}'}\frac{V_{k'}}{2}c^{\dagger}_{\mathbf{q}-\mathbf{k}'}c^{\dagger}_{\mathbf{q}'+\mathbf{k}'}c_{\mathbf{q}'}c_{\mathbf{q}}\right] \\
&\quad = \quad -\sum_{\mathbf{k}',\mathbf{q}'}V_{k'}\left\{c^{\dagger}_{\mathbf{p}}c^{\dagger}_{\mathbf{q}'-\mathbf{k}'}c_{\mathbf{p}+\mathbf{k}-\mathbf{k}'}c_{\mathbf{q}'} + c^{\dagger}_{\mathbf{p}-\mathbf{k}'}c^{\dagger}_{\mathbf{q}'+\mathbf{k}'}c_{\mathbf{q}'}c_{\mathbf{p}+\mathbf{k}}\right\} \\
&\quad \overset{RPA}{\approx} \quad -\sum_{\mathbf{q}',s'}V_{k}\left\{c^{\dagger}_{\mathbf{p}}c^{\dagger}_{\mathbf{q}'-\mathbf{k}}c_{\mathbf{p}}c_{\mathbf{q}'} + c^{\dagger}_{\mathbf{p}+\mathbf{k}}c^{\dagger}_{\mathbf{q}'-\mathbf{k}}c_{\mathbf{q}'}c_{\mathbf{p}+\mathbf{k}}\right\}. \qquad (2.16)
\end{aligned}$$

In the last step, we have made the random phase approximation where we only keep terms with $\mathbf{k}' = \mathbf{k}$ in the first term and $\mathbf{k}' = -\mathbf{k}$ in the second term on the right hand side. Recall that $\mathbf{k}$ is the wave vector associated with the density fluctuation of interest. In essence then, the RPA is a statement identifying that the only important term in the spatial Fourier transform of the Coulomb potential is the one whose k-value coincides with the density fluctuation. If we rearrange the orders of the operators, we obtain

$$\begin{aligned}
&\left[c^{\dagger}_{\mathbf{p}}c_{\mathbf{p}+\mathbf{k}}, \sum_{\mathbf{k}',\mathbf{q},\mathbf{q}'}\frac{V_{k'}}{2}c^{\dagger}_{\mathbf{q}-\mathbf{k}'}c^{\dagger}_{\mathbf{q}'+\mathbf{k}'}c_{\mathbf{q}'}c_{\mathbf{q}}\right] \\
&\quad \overset{RPA}{\approx} \quad -\sum_{\mathbf{q}'}V_{k}\left\{c^{\dagger}_{\mathbf{p}}\left(\delta_{\mathbf{q}'-\mathbf{k},\mathbf{p}} - c_{\mathbf{p}}c^{\dagger}_{\mathbf{q}'-\mathbf{k}}\right)c_{\mathbf{q}'} - c^{\dagger}_{\mathbf{p}+\mathbf{k}}\left(\delta_{\mathbf{q}'-\mathbf{k},\mathbf{p}+\mathbf{k}} - c_{\mathbf{p}+\mathbf{k}}c^{\dagger}_{\mathbf{q}'-\mathbf{k}}\right)c_{\mathbf{q}'}\right\} \\
&\quad = \quad -\sum_{\mathbf{q}'}V_{k}\left\{c^{\dagger}_{\mathbf{p}}c_{\mathbf{p}+\mathbf{k}} - c^{\dagger}_{\mathbf{p}}c_{\mathbf{p}}c^{\dagger}_{\mathbf{q}'-\mathbf{k}}c_{\mathbf{q}'} - c^{\dagger}_{\mathbf{p}+\mathbf{k}}c_{\mathbf{p}+2\mathbf{k}} + c^{\dagger}_{\mathbf{p}+\mathbf{k}}c_{\mathbf{p}+\mathbf{k}}c^{\dagger}_{\mathbf{q}'-\mathbf{k}}c_{\mathbf{q}'}\right\} \qquad (2.17)
\end{aligned}$$

Within the RPA, we can now write the the equation of motion for the summand in the density fluctuation as

$$\begin{aligned}
i\hbar\dot{n}_{\mathbf{p},\mathbf{k}} &= \left[c^{\dagger}_{\mathbf{p}}c_{\mathbf{p}+\mathbf{k}}, H\right] \\
&= \left[E\left(\mathbf{p}+\mathbf{k}\right) - E\left(\mathbf{p}\right)\right]c^{\dagger}_{\mathbf{p}}c_{\mathbf{p}+\mathbf{k}} \\
&\quad - \left\{c^{\dagger}_{\mathbf{p}}c_{\mathbf{p}} - c^{\dagger}_{\mathbf{p}+\mathbf{k}}c_{\mathbf{p}+\mathbf{k}}\right\}e\phi_{ext}\left(\mathbf{k},\omega\right)e^{-i\omega t}e^{\delta t} \\
&\quad - \left\{c^{\dagger}_{\mathbf{p}}c_{\mathbf{p}+2\mathbf{k}} - c^{\dagger}_{\mathbf{p}-\mathbf{k}}c_{\mathbf{p}+\mathbf{k}}\right\}e\phi^{\dagger}_{ext}\left(\mathbf{k},\omega\right)e^{i\omega t}e^{\delta t} \\
&\quad + \left\{c^{\dagger}_{\mathbf{p}}c_{\mathbf{p}} - c^{\dagger}_{\mathbf{p}+\mathbf{k}}c_{\mathbf{p}+\mathbf{k}}\right\}V_{\mathbf{k}}n_{\mathbf{k}}, \qquad (2.18)
\end{aligned}$$

and summing over all $\mathbf{p}$ gives us the equation of motion for the density fluctuation operator. The third time on the right hand side vanishes if we take the expectation value of both sides with appropriate states of the Hamiltonian. Hence, we are left with

$$\begin{aligned} i\hbar \left\langle \dot{n}_{\mathbf{p},\mathbf{k}} \right\rangle &= \left[E\left(\mathbf{p}+\mathbf{k} \right) - E\left(\mathbf{p} \right) \right] \left\langle n_{\mathbf{p},\mathbf{k}} \right\rangle \\ &\quad + \left\{ \left\langle c_{\mathbf{p}}^{\dagger} c_{\mathbf{p}} \right\rangle - \left\langle c_{\mathbf{p}+\mathbf{k}}^{\dagger} c_{\mathbf{p}+\mathbf{k}} \right\rangle \right\} \\ &\quad \times \left\{ -e\phi_{ext}\left(\mathbf{k},\omega \right) e^{-i\omega t} e^{\delta t} + V_{\mathbf{k}} \left\langle n_{\mathbf{k}} \right\rangle \right\}. \end{aligned} \tag{2.19}$$

Taking the Fourier transform of both sides gives

$$\left\langle n_{\mathbf{p},\mathbf{k}}\left(\omega \right) \right\rangle = \frac{-\left\{ n_{\mathbf{p}} - n_{\mathbf{p}+\mathbf{k}} \right\} \left\{ e\phi_{ext}\left(\mathbf{k},\omega \right) - V_{\mathbf{k}} \left\langle n_{\mathbf{k}}\left(\omega \right) \right\rangle \right\}}{\hbar\left(\omega - \omega\left(\mathbf{k},p \right) + i\delta \right)} \tag{2.20}$$

where $\hbar\omega\left(\mathbf{k},p \right) = E\left(\mathbf{p}+\mathbf{k} \right) - E\left(\mathbf{p} \right)$. We may then sum over $\mathbf{p}$ to obtain

$$\begin{aligned} \left\langle n_{\mathbf{k}}\left(\omega \right) \right\rangle_{RPA} &= \sum_{\mathbf{p}} \frac{4\pi e^2}{k^2} \left(\frac{\bar{n}_{\mathbf{p}+\mathbf{k}} - \bar{n}_{\mathbf{p}}}{\hbar\left(\omega - \omega\left(\mathbf{k},p \right) + i\delta \right)} \right) \\ &\quad \times \left\{ \frac{k^2}{4\pi e} \phi_{ext}\left(\mathbf{k},\omega \right) - \frac{k^2}{4\pi e} \frac{4\pi e}{k^2} \left\langle n_{\mathbf{k}}\left(\omega \right) \right\rangle \right\} \\ &= 4\pi\chi_0\left(\mathbf{k},\omega \right) \frac{k^2}{4\pi e} \left\{ \phi_{ext}\left(\mathbf{k},\omega \right) - \frac{4\pi e}{k^2} \left\langle n_{\mathbf{k}}\left(\omega \right) \right\rangle \right\} \\ &= 4\pi\chi^0\left(\mathbf{k},\omega \right) \frac{k^2}{4\pi e} \phi\left(\mathbf{k},\omega \right). \end{aligned} \tag{2.21}$$

In the final step, I have introduced the function χ^0, which is the susceptibility of the electron gas. Inserting this relation into Equation (2.7) gives

$$\epsilon\left(\mathbf{k},\omega \right)_{RPA} = 1 + \frac{4\pi e}{k^2} \frac{\left\langle n\left(\mathbf{k},\omega \right) \right\rangle_{RPA}}{\phi\left(\mathbf{k},\omega \right)} = 1 + 4\pi\chi^0\left(\mathbf{k},\omega \right), \tag{2.22}$$

with

$$\chi^0\left(\mathbf{k},\omega \right) = \frac{e^2}{k^2} \sum_{\mathbf{p}} \frac{\bar{n}_{\mathbf{p}+\mathbf{k}} - \bar{n}_{\mathbf{p}}}{\hbar\omega + E\left(\mathbf{p} \right) - E\left(\mathbf{p}+\mathbf{k} \right) + i\hbar\delta}. \tag{2.23}$$

Equations (2.22) and (2.23) are the two central results for the one-component plasma under the RPA.

2.3.2 RPA χ and ϵ for a two-component plasma

With the results of the previous section in hand, we are now ready to consider a plasma composed of both electrons and holes. The charge density fluctuation operator of the system is now given by the sum of the operators for electrons and holes:

$$n_{\mathbf{k}} = \sum_{\mathbf{p}} c^{\dagger}_{\mathbf{p}} c_{\mathbf{p}+\mathbf{k}} + \sum_{\mathbf{p}} d^{\dagger}_{\mathbf{p}} d_{\mathbf{p}+\mathbf{k}}. \tag{2.24}$$

The interaction portion of the Hamiltonian is given by $H_{int} = \frac{V_k}{2}\left\{n_{\mathbf{k}} n_{-\mathbf{k}} - n_e - n_h\right\}$ where n_e and n_h are the average densities of electrons and holes, respectively. Inserting Equation (2.24) into the expression for the interaction hamiltonian gives

$$\begin{aligned} H_{int} \;=\; & \sum_{\mathbf{k},\mathbf{p},\mathbf{p}'} \frac{V_k}{2} c^{\dagger}_{\mathbf{p}-\mathbf{k}} c^{\dagger}_{\mathbf{p}'+\mathbf{k}} c_{\mathbf{p}} c_{\mathbf{p}'} + \sum_{\mathbf{k},\mathbf{p},\mathbf{p}'} \frac{V_k}{2} d^{\dagger}_{\mathbf{p}-\mathbf{k}} d^{\dagger}_{\mathbf{p}'+\mathbf{k}} d_{\mathbf{p}} d_{\mathbf{p}'} \\ & + \sum_{\mathbf{k},\mathbf{p},\mathbf{p}'} V_k c^{\dagger}_{\mathbf{p}} c_{\mathbf{p}-\mathbf{k}} d^{\dagger}_{\mathbf{p}'} d_{\mathbf{p}'+\mathbf{k}}. \end{aligned} \tag{2.25}$$

The three terms represent the coulomb interaction between the electrons, holes, and electrons with holes. The first two terms give results identical to what we already derived and only the equation of motion for the third term remains to be found:

$$\left[c^{\dagger}_{\mathbf{p}}c_{\mathbf{p+k}},\sum_{\mathbf{k}',\mathbf{q},\mathbf{q}'}V_{k'}c^{\dagger}_{\mathbf{q}}c_{\mathbf{q-k}'}d^{\dagger}_{\mathbf{q}'}d_{\mathbf{q}'+\mathbf{k}'}\right] = \left[c^{\dagger}_{\mathbf{n-k}}c_{\mathbf{n}},\sum_{\mathbf{k}',\mathbf{q},\mathbf{q}'}V_{k'}c^{\dagger}_{\mathbf{q}}c_{\mathbf{q-k}'}d^{\dagger}_{\mathbf{q}'}d_{\mathbf{q}'+\mathbf{k}'}\right]$$

$$\begin{aligned}
&= \sum_{\mathbf{k}',\mathbf{q},\mathbf{q}'}V_{k'}\left\{c^{\dagger}_{\mathbf{n-k}}c_{\mathbf{n}}c^{\dagger}_{\mathbf{q}}c_{\mathbf{q-k}'}d^{\dagger}_{\mathbf{q}'}d_{\mathbf{q}'+\mathbf{k}'} - c^{\dagger}_{\mathbf{q}}c_{\mathbf{q-k}'}d^{\dagger}_{\mathbf{q}'}d_{\mathbf{q}'+\mathbf{k}'}c^{\dagger}_{\mathbf{n-k}}c_{\mathbf{n}}\right\}\\
&= \sum_{\mathbf{k}',\mathbf{q},\mathbf{q}'}V_{k'}\left\{c^{\dagger}_{\mathbf{n-k}}c_{\mathbf{n}}c^{\dagger}_{\mathbf{q}}c_{\mathbf{q-k}'}d^{\dagger}_{\mathbf{q}'}d_{\mathbf{q}'+\mathbf{k}'} - c^{\dagger}_{\mathbf{n-k}}c_{\mathbf{n}}c^{\dagger}_{\mathbf{q}}c_{\mathbf{q-k}'}d^{\dagger}_{\mathbf{q}'}d_{\mathbf{q}'+\mathbf{k}'}\right.\\
&\qquad \left. + c^{\dagger}_{\mathbf{n-k}}c_{\mathbf{q-k}'}d^{\dagger}_{\mathbf{q}'}d_{\mathbf{q}'+\mathbf{k}'}\delta_{\mathbf{n},\mathbf{q}} - c^{\dagger}_{\mathbf{q}}c_{\mathbf{n}}d^{\dagger}_{\mathbf{q}'}d_{\mathbf{q}'+\mathbf{k}'}\delta_{\mathbf{n-k},\mathbf{q-k}'}\right\}\\
&= \sum_{\mathbf{k}',\mathbf{q}',s'}V_{k'}\left\{c^{\dagger}_{\mathbf{n-k}}c_{\mathbf{n-k}'}d^{\dagger}_{\mathbf{q}'}d_{\mathbf{q}'+\mathbf{k}'} - c^{\dagger}_{\mathbf{n-k}+\mathbf{k}'}c_{\mathbf{n}}d^{\dagger}_{\mathbf{q}'}d_{\mathbf{q}'+\mathbf{k}'}\right\}\\
&\overset{RPA}{\approx} \sum_{\mathbf{q},s'}V_{k}\left\{c^{\dagger}_{\mathbf{n-k}}c_{\mathbf{n-k}}d^{\dagger}_{\mathbf{q}'}d_{\mathbf{q}'+\mathbf{k}} - c^{\dagger}_{\mathbf{n}}c_{\mathbf{n}}d^{\dagger}_{\mathbf{q}'}d_{\mathbf{q}'+\mathbf{k}}\right\}
\end{aligned} \tag{2.26}$$

Finally, we make the change of variables $\mathbf{p} = \mathbf{n} - \mathbf{k}$:

$$\begin{aligned}
\left[c^{\dagger}_{\mathbf{p}}c_{\mathbf{p+k}},\sum_{\mathbf{k}',\mathbf{q},\mathbf{q}'}V_{k'}c^{\dagger}_{\mathbf{q}}c_{\mathbf{q-k}'}d^{\dagger}_{\mathbf{q}'}d_{\mathbf{q}'+\mathbf{k}'}\right] &\overset{RPA}{\approx} \sum_{\mathbf{q}'}V_{k}\left\{c^{\dagger}_{\mathbf{p}}c_{\mathbf{p}}d^{\dagger}_{\mathbf{q}'}d_{\mathbf{q}'+\mathbf{k}}\right.\\
&\qquad \left. - c^{\dagger}_{\mathbf{p+k}}c_{\mathbf{p+k}}d^{\dagger}_{\mathbf{q}'}d_{\mathbf{q}'+\mathbf{k}}\right\}
\end{aligned} \tag{2.27}$$

Upon summing over $\mathbf{p}$, both terms in the bracket on the right hand side will cancel each other, and consequently, we may neglect the third term in Equation (2.25). As a result, the form of $\langle n(\mathbf{k},\omega)\rangle_{RPA}$ for the two-component plasma will simply have an additional term for holes equivalent in form to the electronic term. Therefore,

$$\epsilon(\mathbf{k},\omega)_{RPA} = 1 + 4\pi\chi^{0}_{e}(\mathbf{k},\omega) + 4\pi\chi^{0}_{h}(\mathbf{k},\omega), \tag{2.28}$$

where

$$\chi^{0}_{j}(\mathbf{k},\omega) = \frac{e^2}{k^2}\sum_{\mathbf{p}}\frac{\bar{n}^{j}_{\mathbf{p+k}} - \bar{n}^{j}_{\mathbf{p}}}{\hbar\omega + E_j(\mathbf{p}) - E_j(\mathbf{p}+\mathbf{k}) + i\hbar\delta}, \tag{2.29}$$

and $j = e, h$. These are the RPA dielectric function of the two-component plasma and the susceptibility of species j, respectively. Plasmas consisting of more than 2 species can be treated identically by simply adding the individual susceptibility contributions for each

species.

2.4 Visualizing the dielectric functions

Having covered the microscopic theory of acoustic plasmons, it is beneficial for us to spend some time visualizing the dielectric functions that we derived. Specifically, let us treat the case where the plasma is within a semiconductor. In order to do this, we will need to modify the dielectric function expression slightly to account for the background dielectric constant of the semiconductor. That is,

$$\epsilon_{RPA}\left(\mathbf{q},\omega\right)=\epsilon_{\infty}+4\pi\chi_{e}\left(\mathbf{q},\omega\right)+4\pi\chi_{h}\left(\mathbf{q},\omega\right). \tag{2.30}$$

In order to evaluate the susceptibility terms, we can assume we are in quasi-equilibrium and use the Fermi-Dirac distribution function for the expectation values of the number operators appearing in (2.29). Converting the sum to an integral by letting $\sum_{\mathbf{k}}\rightarrow\left(1/8\pi^{3}\right)\int d^{3}k$, we can write

$$\chi_{j}^{0}\left(\mathbf{q},\omega\right)=\frac{2e^{2}}{k^{2}}\frac{1}{8\pi^{3}}\int d^{3}k\left[\frac{f_{j}\left(\mathbf{k},T\right)-f_{j}\left(\mathbf{k}+\mathbf{q},T\right)}{E_{j}\left(\mathbf{k}+\mathbf{q}\right)-E_{j}\left(\mathbf{k}\right)-\hbar\omega}\right], \tag{2.31}$$

with

$$f_{j}\left(\mathbf{k},T\right)=\frac{1}{\exp\left(E_{j}\left(\mathbf{k}\right)/k_{B}T\right)\exp\left(-\mu_{j}/k_{B}T\right)+1}, \tag{2.32}$$

and where μ_j is the quasi-chemical potential of species j. The factor of 2 in Equation (2.31) comes from taking into account the the two spin states. Calculating the dielectric function now seems like a simple application of Equations (2.30) and (2.31), but doing so would be incorrect. First and foremost, we need to include the effects of collision damping within the plasma. Ostensibly, the way to do this would be to pass $\omega\rightarrow\omega+i\Gamma$ where $\tau=\Gamma^{-1}$ is the lifetime of the carrier. Unfortunately, this approach does not conserve the local density of the plasma. N.D. Mermin solved this problem by requiring that the plasma system relax toward a local equilibrium rather than the thermodynamic equilibrium [28]. The result is

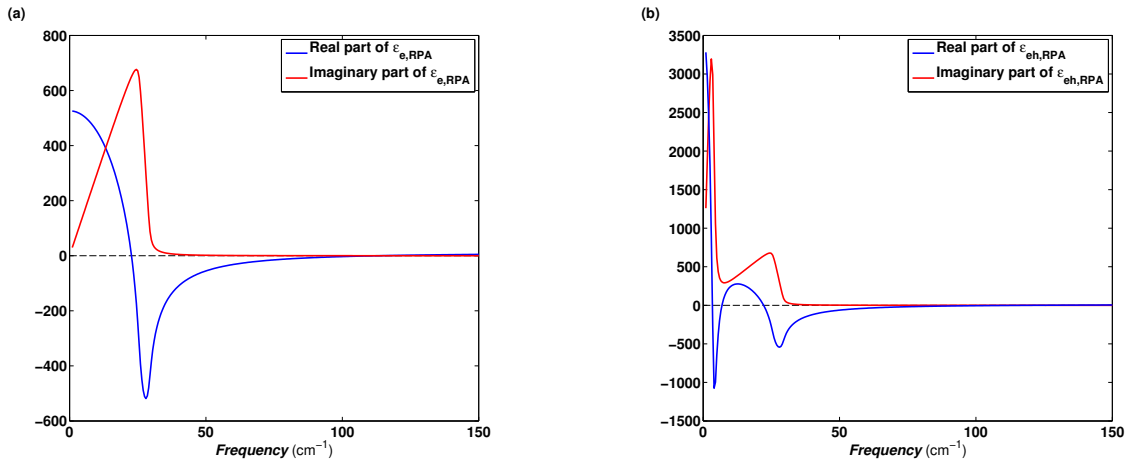

Figure 2.2: (a) The real and imaginary part of the dielectric function for a one-component plasma, and (b) the real and imaginary part of the dielectric function for a two-component plasma.

the so-called Lindhard-Mermin susceptibility given by [29]

$$\chi_j(\mathbf{q},\omega) = \frac{(1+i\Gamma/\omega)\left[\chi_j^0(\mathbf{q},\omega+i\Gamma)\right]}{1+(i\Gamma/\omega)\left[\chi_j^0(\mathbf{q},\omega+i\Gamma)/\chi_j^0(\mathbf{q},0)\right]}. \tag{2.33}$$

As we would expect, when $\Gamma \to 0$, we recover Equation (2.31). We now have an expression for the susceptibility that is dependent on carrier density (through μ in $f_j(\mathbf{k},T)$), temperature, and damping.

Computing (2.33) is straightforward, provided we know the energy dispersion associated with the two plasma species. This is a major caveat, but for the moment, lets use the simplest approximation and treat the two charge species as free-particle-like. In this case, the energies will be parabolic in k with the curvature defined by some effective mass. This is known as the Lindhard approximation, and with it, we can evaluate and plot Equation (2.30) and also see how the roots behave upon changing $\mathbf{q}$ and the average carrier density $n_0 = n_e = n_h$. Figure 2.2(a) shows the real and imaginary parts of the dielectric function for a one-component plasma composed of electrons. We can see that the real part of the dielectric function has two roots, but only one of these is at a frequency where the imaginary part of the dielectric function is small. Physically, the lower frequency root corresponds

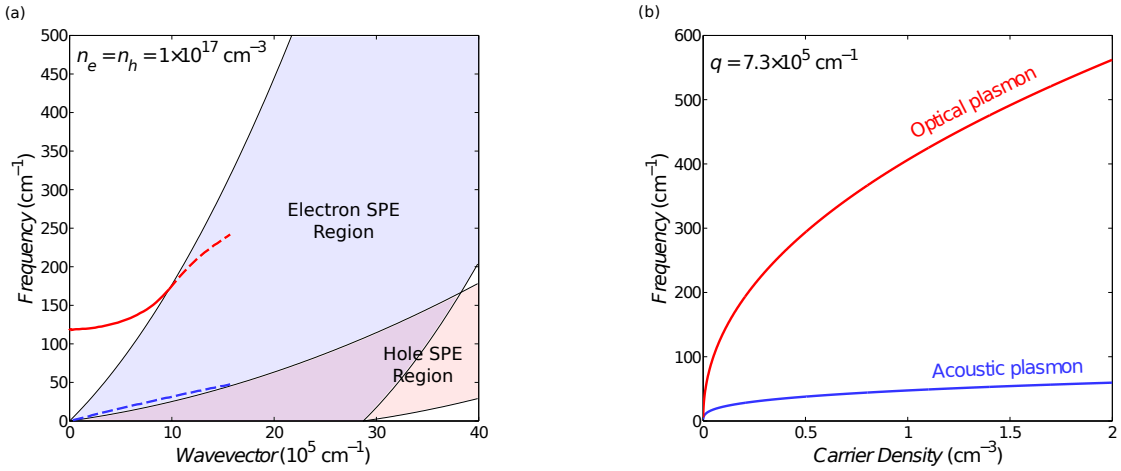

Figure 2.3: (a) The optical and acoustic plasmon dispersion under the Lindhard approximation. These curves were obtained using a carrier density of $N_e = N_h = 1 \times 10^{17}$ cm^{-3} at $T = 10$ K. (b) The carrier density dependence of the optical and acoustic plasmon under the Lindhard approximation for $q = 7.3 \times 10^5$ cm^{-1} at $T = 10$ K.

to single particle excitations (SPE) of the electrons from a state just inside to outside the Fermi sphere. These excitations form a continuum, and play a significant role in the damping of the collective excitations of the plasma. The higher frequency root corresponds to the optical plasmon. Figure 2.2(b) shows the real and imaginary parts of the dielectric function for an EHP. We see that the real part now has four zeros. The lowest frequency root, which coincides with the first peak in the imaginary part of the dielectric function, represents the SPE of holes. The second root coincides with the minima in the imaginary part of the dielectric function, and it is this root that gives rise to acoustic plasmons. The last two roots in the real part of the dielectric function have the same interpretation as those in Figure 2.2(a).

The optical and acoustic plasmon frequencies depend on $\mathbf{q}$ and more subtly upon the carrier density, n_0, which enters through the Fermi-Dirac term in Equation (2.31) where it changes the quasi-chemical potential. Figure 2.3(a) shows the dispersion of the optical and acoustic plasmon in the Lindhard approximation. As expected, the optical plasmon has a quadratic dispersion, while the acoustic plasmon's is nearly linear with $\omega \to 0$ as $q \to 0$. The two shaded regions correspond to the continuum of single particle excitations

for the electrons (blue) and holes (red). The optical plasmon only intersects with electron continuum after a certain value of q. At wave vectors lower than this, the lack of overlap means that the optical plasmon is not coupled to any single particle excitations. In contrast, the acoustic plasmon is embedded in the SPE region for low q. This means that in light scattering experiments, the branch will usually be coupled to at least one continuum of single particle excitations in a process known as Landau damping. As a result, spectral lines associated with acoustic plasmons can be very broad and the lifetimes short in the time domain [30]. Figure 2.3(b) shows a plot of the carrier density dependence of the plasmons, both exhibit a fractional power law dependence, albeit with different exponential factors. Both the wave vector and density dependence of the acoustic plasmon played an important role in my experiments, as I will discuss in Chapters 5 and 6.

2.5 Dealing with transitions

Thus far, we have used the RPA to find the longitudinal dielectric function of for a multi-component plasma, and in the previous section we have explored the simple case of parabolic energy dispersion. However in the preceding discussion, we have not considered the nature of the crystal lattice and how it may affect the calculation of the dielectric function (apart from the inclusion of ϵ_∞). Since I use GaAs in my experiments, we must in fact play close attention to three bands (i.e. three charge species), namely the conduction band electrons, heavy hole, and light hole. We now have to contend with two issues. First, we must determine the likelihood with which a charge species will make an intraband transition. Strictly speaking, in writing the susceptibility in Equation (2.31) we have assumed this probability to be unity. However, for GaAs and other similar semiconductors, this is only valid for the conduction band electrons. For both the heavy and light holes, the structure of the eigenstates depends on the direction of the wave vector [31, 32]. As a result, the intraband transition probability depends upon the direction of the excitation. In light of

this fact, we must modify Equation (2.31) as [33, 34]

$$\chi_j^0\left(\mathbf{q},\omega+i\Gamma\right)=\frac{e^2}{4\pi^3q^2}\int d^3k\overleftrightarrow{\mathbf{M}}_j\frac{f_j\left(\mathbf{k},T\right)-f_j\left(\mathbf{k}+\mathbf{q},T\right)}{E_j\left(\mathbf{k}+\mathbf{q}\right)-E_j\left(\mathbf{k}\right)-\hbar\omega-i\hbar\Gamma} \tag{2.34}$$

where $\overleftrightarrow{\mathbf{M}}_j$ is the intraband matrix element given by

$$\overleftrightarrow{\mathbf{M}}_j=\begin{cases}1, & j=e\\ \frac{1}{4}+\frac{3\left(k^2+\mathbf{q}\cdot\mathbf{k}\right)^2}{4k^2\left(q^2+k^2+2\mathbf{q}\cdot\mathbf{k}\right)}, & j=hh \text{ or } lh.\end{cases} \tag{2.35}$$

The second consideration involves interband transitions. If we were dealing with a system composed of just two bands, say the conduction band and the heavy hole, there would be no real need to worry about interband transitions and their impact on the longitudinal dielectric function. This is because in the wave vector regime we are concerned with ($\sim 10^5$ cm^{-1}), the band gap is far too large to allow for interband transitions through the creation or annihilation of a quasiparticle such as a plasmon or phonon. However, when the light holes are included in the system, the energy gap between the heavy hole and light hole bands around $\mathbf{k}=0$ (the Γ-point) is small enough to allow interband scattering via quasiparticles. As a result, if we want to make quantitative comparisons between experiment and theory, we must include the susceptibility contribution due to $hh\leftrightarrow lh$ interband transitions in the dielectric function calculations. In order to do this, we use an expression similar to Equation (2.34), where the energy denominator and matrix element take into account the fact that the initial and final states are in different bands. Namely[33, 34],

$$\begin{aligned}\chi_{inter}^0\left(\mathbf{q},\omega+i\Gamma\right) &= \frac{e^2}{4\pi^3q^2}\int d^3k\times\overleftrightarrow{\mathbf{M}}_{inter}\\ &\left[\frac{f_{lh}\left(\mathbf{k},T\right)-f_{hh}\left(\mathbf{k}+\mathbf{q},T\right)}{E_{hh}\left(\mathbf{k}+\mathbf{q}\right)-E_{lh}\left(\mathbf{k}\right)+\hbar\omega+i\hbar\Gamma}\right.\\ &\left.+\frac{f_{lh}\left(\mathbf{k},T\right)-f_{hh}\left(\mathbf{k}+\mathbf{q},T\right)}{E_{hh}\left(\mathbf{k}+\mathbf{q}\right)-E_{lh}\left(\mathbf{k}\right)-\hbar\omega-i\hbar\Gamma}\right],\end{aligned} \tag{2.36}$$

where

$$\overleftrightarrow{\mathrm{M}}_{inter} = \frac{3}{4} - \frac{3\left(k^2 + \mathbf{q}\cdot\mathbf{k}\right)^2}{4k^2\left(q^2 + k^2 + 2\mathbf{q}\cdot\mathbf{k}\right)}. \tag{2.37}$$

The first term in the brackets in Equation (2.36) represents $lh \rightarrow hh$ transitions and the second term to $hh \rightarrow lh$ transitions. Equations (2.34)-(2.37) are the final forms of the electron and hole susceptibility expressions that I will use in theoretical calculations of the acoustic plasmon properties.

2.6 Acoustic plasmon standing waves

The final aspect we must consider involves the form of the acoustic plasmon when the supporting plasma is constrained to a slab. Recall that an acoustic plasmon represents a density fluctuation of the EHP. As such, in order to determine the form of this fluctuation, we can treat the EHP as a hydrodynamic fluid confined to a layer of GaAs, and use the hydrodynamic equations to derive the boundary conditions on the density fluctuation in order to determine its form.

2.6.1 Momentum equation for a plasma

There are three major forces that act on the plasma that we must consider in developing an equation governing momentum conservation. They are the Lorentz force due to external fields, the force associated with the "pressure", and finally the force due to collisions between the different species of the plasma. Each of these can be written as [35]

$$\mathbf{F}_L = e\left(\mathbf{E} + \mathbf{v}\times\mathbf{B}\right) \tag{2.38}$$

$$\mathbf{F}_p = \frac{-\nabla P}{n} \tag{2.39}$$

$$\mathbf{F}_c = -m\sum_{a,b}\nu_{a,b}\left(\mathbf{v}_a - \mathbf{v}_b\right) \tag{2.40}$$

where n is the plasma density, m is the mass density, and a and b are plasma species labels. The net force must be equivalent to m times the total time derivative of the fluid velocity. If we ignore the collision term, we obtain [35]

$$m\left[\frac{\partial \mathbf{v}}{\partial t}+(\mathbf{v}\cdot\nabla)\,\mathbf{v}\right] \;=\; e\,(\mathbf{E}+\mathbf{v}\times\mathbf{B})-\frac{\nabla P}{n}. \tag{2.41}$$

If we further assume that $v_z = v_z\,(z)$, then the z-component of (2.41) is

$$\frac{\partial v_z}{\partial t}+v_z\frac{\partial v_z}{\partial z}=eE_z+v_xB_y-v_yB_x-\frac{1}{n}\frac{\partial P}{\partial z} \tag{2.42}$$

In my experiment, I deal with a photoexcited EHP in a layer of GaAs cladded by AlAs layers. In the z-direction (normal to the sample plane), the plasma is confined to the GaAs layer since the AlAs layers serve as potential barriers preventing photoexcited carriers from crossing the interface. This means that $v_z = 0$ at the interface, so the second term on the left hand side of Equation (2.41) must go to zero. Also, since the local velocity of the fluid at the interfaces must be zero at *all times*, the partial derivative with time must vanish at the interfaces as well. If we assume no magnetic fields are present, Equation (2.42) now becomes

$$\left.\frac{1}{n}\,\frac{\partial P}{\partial z}\right|_{z=0,d} = e\;E_z|_{z=0,d}\,. \tag{2.43}$$

There are two major electric fields that are present in the photoexcited volume. The first is due to the LO phonon, but due to the mismatch in the AlAs and GaAs phonon energies, it will not propagate from the GaAs layer into the AlAs cladding [36]. As a result, the lattice displacement in the cladding must be zero as well, so it and the associated electric field must vanish at the interface to preserve continuity. The second source of an electric field comes from a non-zero net charge density on the interface. The difference in the electric displacement between the two layers must be equal to the interface charge density. At equilibrium, it is net neutral, and in the absence of any other fields, the carrier induced

electric field must be zero. All this means that the right hand side of Equation (2.43) must vanish at the interfaces. Furthermore, in the adiabatic limit [35]

$$P \propto n^{\gamma},$$

where γ is the polytropic index. This means that $\partial P/\partial z \propto \partial n/\partial z$, so we are left with

$$\left.\frac{dn}{dz}\right|_{z=0,d} = 0.$$

This condition, coupled with the assumption that the density fluctuation is small, is sufficient to show the form of the acoustic plasmon exists as a set of standing waves confined to the active layer of GaAs.

2.6.2 Standing waves

Since we are treating the plasma as a fluid, we must also satisfy particle conservation through the continuity equation given by [35]

$$\frac{\partial n}{\partial t} + (\mathbf{v} \cdot \nabla)\, n + n \nabla \cdot \mathbf{v} = 0. \tag{2.44}$$

This can be expanded as

$$\frac{\partial n}{\partial t} + v_x \frac{\partial n}{\partial x} + v_y \frac{\partial n}{\partial y} + v_z \frac{\partial n}{\partial z} + n \frac{\partial v_x}{\partial x} + n \frac{\partial v_y}{\partial y} + n \frac{\partial v_z}{\partial z} = 0. \tag{2.45}$$

Now, let us write the particle density term as $n = n_0 + \Delta n$ and make the reasonable assumption that the density fluctuation is small (i.e. $\Delta n \ll n_0$). Further, if we assume that the average density (n_0) does not vary in time and is uniform, and that $v_x = v_y = 0$, we

can approximate the continuity equation to

$$\frac{\partial \Delta n}{\partial t} + n_0 \frac{\partial v_z}{\partial z} = 0. \tag{2.46}$$

We can solve this partial differential equation by assuming a general (complex) solution of the form

$$\Delta \widetilde{n} = a e^{iqz} e^{-i\omega t} + b e^{-iqz} e^{-i\omega t} + a^* e^{-iqz} e^{i\omega t} + b^* e^{iqz} e^{i\omega t}. \tag{2.47}$$

Inserting Equation (2.47) into (2.46) and integrating gives

$$v_z(z) = \frac{\omega a}{n_0 q} e^{-i\omega t} e^{iqz} - \frac{\omega b}{n_0 q} e^{-i\omega t} e^{-iqz} + \frac{\omega a^*}{n_0 q} e^{i\omega t} e^{-iqz} - \frac{\omega b^*}{n_0 q} e^{i\omega t} e^{iqz} + C. \tag{2.48}$$

The z-component of the velocity must vanish at the interfaces between the active GaAs layer and the AlAs claddings. Imposing these conditions on Equation (2.48) yield

$$\begin{cases} \frac{\omega}{n_0 q} e^{-i\omega t}(a-b) + \frac{\omega}{n_0 q} e^{i\omega t}(a^* - b^*) + C = 0 \\ \frac{\omega}{n_0 q} e^{-i\omega t}\left(a e^{iqd} - b e^{-iqd}\right) + \frac{\omega}{n_0 q} e^{i\omega t}\left(a^* e^{-iqd} - b^* e^{iqd}\right) + C = 0 \end{cases} \tag{2.49}$$

We also know that $\partial n / \partial z = 0$ at the interfaces, and we may impose these conditions on Equation (2.47):

$$\begin{cases} e^{-i\omega t}(a-b) - e^{i\omega t}(a^* - b^*) = 0 \\ e^{-i\omega t}\left(a e^{iqd} - b e^{-iqd}\right) - e^{i\omega t}\left(a^* e^{-iqd} - b^* e^{iqd}\right) = 0 \end{cases} \tag{2.50}$$

Equations (2.49) and (2.50) can only be simultaneously satisfied when $C = 0$ and $a = b$. With these, the density fluctuation takes the form

$$\begin{aligned} \Delta \widetilde{n} &= a e^{iqz} e^{-i\omega t} + a e^{-iqz} e^{-i\omega t} + a^* e^{-iqz} e^{i\omega t} + a^* e^{iqz} e^{i\omega t} \qquad \therefore \\ \Delta n &\approx \cos(qz)\cos(\omega t + \phi). \end{aligned} \tag{2.51}$$

The fact that $\partial n/\partial z = 0$ at $z = 0$ and $z = d$ is satisfied by Equation (2.51) as long as

$$q = q_m = \frac{m\pi}{d}, m = 1, 2, 3... \tag{2.52}$$

Thus, if the carriers are confined to a finite slab, the acoustic plasmon exists as standing wave modes with discrete wavevectors. The separation between these wavevectors is dependent upon the thickness of the layer. We shall see, in Chapters 5 and 6, that the discretization of the acoustic plasmon into standing waves will have a significant effect on light scattering spectra and time-domain dynamics in thin samples.

2.7 Summary

Acoustic plasmons represent the density fluctuation of a multi-component plasma due to screening of Coulomb interactions. While a simplified description using the Thomas-Fermi and Drude models provides us with a qualitative understanding of the phenomenon, it is only through a rigorous treatment under the random phase approximation that we can obtain a more complete description of the phenomenon. In particular, this approach gives us a means to understand the effects of plasma density, temperature, and damping. In addition, we can incorporate the intraband and interband transition probabilities into theoretical predictions. As I will show in the subsequent chapters, these parameters play an important part in determining not only the properties of the acoustic plasmon, but also its light scattering cross section. Furthermore, when confined to a finite slab, the acoustic plasmon exists as a set of standing waves, each with a unique wavevector defined by an integer multiple of a fundamental value proportional to the inverse sample thickness. This discretization has a significant impact on the interpretation of light scattering spectra and also the observed time-domain dynamics seen in pump-probe experiments.

CHAPTER 3

Light scattering from semiconductor plasmas

Inelastic light scattering is a versatile tool well-suited to the investigation of a wide range of material properties. As this work focuses upon the study of acoustic plasmons in GaAs, this requires us to consider the nature of light scattering from semiconductor plasmas. This forces us to consider not only how a plasma interacts with light, but also how the crystal structure and resonant photoexcitation can affect the process. Several approaches have been used to address this problem, beginning with simple models of the plasma as a free-electron gas, to more complex theories that allow us to take into account the Bloch periodicity, multi-component composition, and resonant effects within a photoexcited semiconductor plasma.

In this chapter, I will review the development of the relevant scattering cross sections for various classes of plasma and light field configurations. After developing the general form of the scattering cross section from a simple plasma, we will see how the inclusion of multiple carrier species introduces resonant scattering from LO phonon-optical plasmon coupled modes and single particle excitations, both of which can be used to determine the plasma parameters. I will then discuss the scattering associated with acoustic plasmons, and conclude with a discussion of how to calculate the necessary susceptibilities given the band structure of GaAs.

3.1 Inelastic light scattering

Before looking at the details of light scattering from semiconductor plasmas, let us take a moment to discuss inelastic light scattering in general terms. We are interested in is a process by which an incident photon of frequency ω_I is scattered to a frequency ω_S by some type of excitation (plasmon, phonon, etc.). In the case that $\omega_I > \omega_S$, the process is known as Stokes scattering, and energy and momentum conservation require that

$$\begin{cases} \omega & = \omega_I - \omega_S \\ \mathbf{q} & = \mathbf{k}_I - \mathbf{k}_S \end{cases}, \tag{3.1}$$

where ω and $\mathbf{q}$ are the frequency and wavevector of the Stokes excitation.

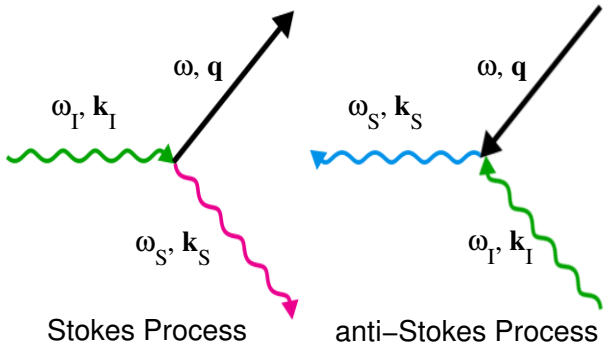

Figure 3.1: Schematic diagram of the Stokes and anti-Stokes scattering processes.

There is also a second process in which $\omega_I < \omega_S$, and this is known as anti-Stokes scattering. In this case, the conservation conditions are

$$\begin{cases} \omega & = \omega_S - \omega_I \\ \mathbf{q} & = \mathbf{k}_S - \mathbf{k}_I \end{cases}, \tag{3.2}$$

Schematically, we can diagram the two processes as in Figure 3.1.

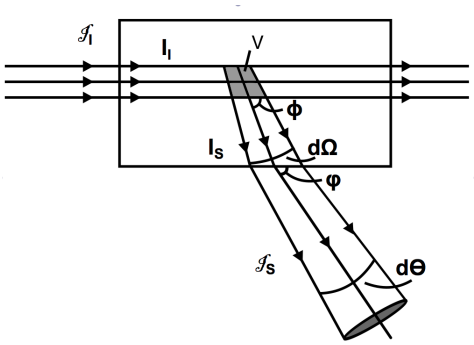

Figure 3.2: Schematic of an idealized scattering experiment, reproduced from [37]

An idealized schematic of the the inelastic light scattering experiment is shown in Figure 3.2. We shine light with intensity $\mathscr{I}_I$ on the sample from a given direction and then measure the scattered light intensity $\mathscr{I}_S$ emanating from a scattering volume V in the sample. It is typically impractical to collect light in all directions, so instead, we restrict our attention to light scattered at some angle φ. Also, since the lens we use to do this has a finite aperture, we are only able to collect light over a solid angle $d\Theta$. We then convert the measured quantities into their counterparts within the sample using the optical properties of the scatterer. If we use a spectrometer to interrogate the spectral composition of the scattered light, we are measuring what is known as the double differential spectral scattering cross section associated with this process, or $d^2\sigma/d\Omega d\omega$. Physically, this quantity represents the rate of removal of energy from the incident beam as a result of scattering within some volume V into a differential solid angle element $d\Omega$ with a scattered light frequency between ω and $\omega + d\omega$ divided by $I_I d\Omega d\omega$ [37].

In a typical light scattering experiment, we obtain spectra such as the one shown in Figure 3.3. The central peak corresponds to elastic scattering of light from the sample. The high and low energy side peaks correspond to the the anti-Stokes and Stokes scattering from an excitation, respectively. When not on resonance with the sample, the ratio of anti-Stokes to Stokes intensity is related by

$$\frac{I_{as}}{I_{stokes}} = \frac{n\left(\omega\right)}{n\left(\omega\right)+1}, \tag{3.3}$$

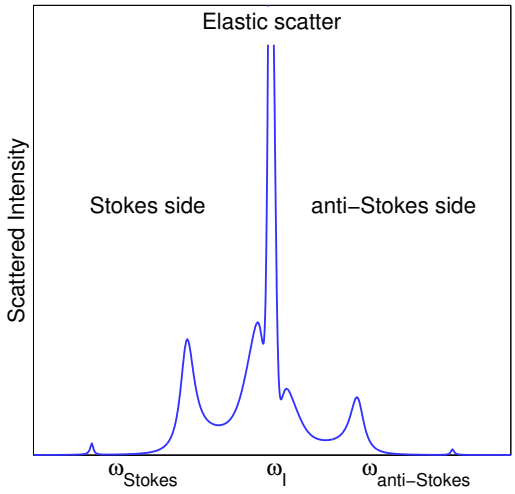

Figure 3.3: Typical light scattering spectra

where $n(\omega)$ is the Bose-Einstein factor defined as

$$n(\omega) = \frac{1}{e^{\hbar\omega/k_B T} - 1}. \tag{3.4}$$

where T is the temperature associated with the excitation. Therefore, measuring the anti-Stokes-Stokes ratio allows us to measure the excitation temperature. In general, for low temperature experiments, the Stokes scattering intensity will be much larger than the anti-Stokes intensity. Additionally, the presence of the Stokes and anti-Stokes peaks are often dependent upon satisfying certain selection rules pertinent to the scattering process. For scattering from semiconductor plasmas, these involve the orientation of the incident and scattered electric field polarizations with respect to the tensor describing the mass of the carrier in the crystal.

3.2 Fermi's Golden Rule and the scattering cross section

Our goal is to obtain expressions that describe the situation in which an incident photon of some momentum and polarization scatters from a plasma into another photon while causing

the plasma to transition to a new state. In order to derive an expression for the scattering cross section, we need to construct a Hamiltonian for the relevant process. In our case, we can begin with the interaction between a radiation field and a gas of free electrons defined by [2]

$$H_{e-R} = \frac{e^2}{2m_0c^2}\sum_j \left|\mathbf{A}\left(\mathbf{r}_j,t\right)\right|^2 + \frac{e}{2m_0c}\sum_j \left[\mathbf{p}_j\cdot\mathbf{A}\left(\mathbf{r}_j,t\right)+\mathbf{A}\left(\mathbf{r}_j,t\right)\cdot\mathbf{p}_j\right]. \tag{3.5}$$

Here, $\mathbf{r}_j$ and $\mathbf{p}_j$ are the j-th electron's position and momentum, respectively. $\mathbf{A}$ is the vector potential of the light-field, which when quantized, is given by

$$\begin{aligned}\mathbf{A}\left(\mathbf{r}_j,t\right) &= \sum_{\mathbf{k}}\hat{\epsilon}_{\mathbf{k}}\left\{\hat{A}\exp\left(i\mathbf{k}\cdot\mathbf{r}-i\omega t\right)+\hat{A}^{\dagger}\exp\left(-i\mathbf{k}\cdot\mathbf{r}+i\omega t\right)\right\}\\ &= \sum_{\mathbf{k}}\hat{\epsilon}_{\mathbf{k}}\left(\frac{2\pi\hbar c^2}{n_\omega^2 V\omega}\right)^{1/2}\\ &\quad\times\left\{\hat{a}_{\mathbf{k}}\exp\left(i\mathbf{k}\cdot\mathbf{r}-i\omega t\right)+\hat{a}_{\mathbf{k}}^{\dagger}\exp\left(-i\mathbf{k}\cdot\mathbf{r}+i\omega t\right)\right\},\end{aligned} \tag{3.6}$$

where n_ω is the refractive index of the scatterer at ω, $\hat{a}_{\mathbf{k}}$ ($\hat{a}_{\mathbf{k}}^{\dagger}$) is the annihilation (creation) operator for a photon with wave vector $\mathbf{k}$, and $\hat{\epsilon}_{\mathbf{k}}$ is the polarization. For now, let us only consider the first term on the right hand side of Equation (3.5), since this is the important term for the simplest case of scattering from a free electron gas [38, 37]. Here, the lack of band-band transitions leads to a ratio of $\mathbf{A}\cdot\mathbf{p}$ to $\mathbf{A}^2$ terms approximately equal to $\hbar\omega_I/m_0c^2$, which is negligibly small at visible incident frequencies (ω_I). If we take the scattered frequency as ω_S, we can rewrite the $\mathbf{A}^2$ term as [38]

$$H_{e-R}^1 = \left(\frac{e^2}{m_0c^2}\right)\left(\hat{\epsilon}_I\cdot\hat{\epsilon}_S\right)\hat{A}_I\hat{A}_S^{\dagger}\exp\left(-i\omega t\right)\sum_j\exp\left(i\mathbf{q}\cdot\mathbf{r}_j\right)+H.C., \tag{3.7}$$

where $\omega=\omega_I-\omega_S$, $\mathbf{q}=\mathbf{k}_I-\mathbf{k}_S$, and $\sum_j\exp\left(i\mathbf{q}\cdot\mathbf{r}_j\right)=\hat{n}_{-\mathbf{q}}=\sum_{\mathbf{k}}\hat{c}_{\mathbf{k}+\mathbf{q}}^{\dagger}\hat{c}_{\mathbf{k}}$ is the density fluctuation operator. We consider the initial and final states of the system of electrons and

photons as

$$|n\rangle = |\alpha\rangle |i\rangle = |n_I, n_S\rangle |i\rangle \tag{3.8}$$

$$|m\rangle = |\beta\rangle |f\rangle = |n_I - 1, n_S + 1\rangle |f\rangle , \tag{3.9}$$

where n_I and n_S are the occupation numbers of the incident and scattered photon states, and $|i\rangle$ and $|f\rangle$ are the initial and final many-body states of the electron gas. As such, we are interested in the process where an incident photon is annihilated and a scattered photon is created as the plasma transitions from the initial to final state. Using Equation (3.5) and Fermi's Golden Rule, given by

$$W_{i\to f} = \frac{2\pi}{\hbar} \left|\langle m| H^1_{e-R} |n\rangle\right|^2 \delta \left(E_i + \hbar\omega_I - E_f - \hbar\omega_S\right) \tag{3.10}$$

we can write the scattering cross section as [39]

$$\begin{aligned} \frac{\partial^2\sigma}{\partial\Omega\partial\omega} &= \left(\frac{e^2}{m_0c^2}\right)^2 \left(\frac{\omega_S}{\omega_I}\right)^2 (\hat{\epsilon}_I \cdot \hat{\epsilon}_S)^2 \\ &\quad \times \sum_f \left|\langle f| \hat{n}_{-\mathbf{q}} |i\rangle\right|^2 \delta \left(\hbar\omega + E_i - E_f\right). \end{aligned} \tag{3.11}$$

Equation (3.11) is the general form of the scattering cross section due to the A^2 term of the electron-radiation hamiltonian. We can actually put this into a more useful form by converting the δ-function term into an integral. Since

$$\delta \left(\hbar\omega + E_i - E_f\right) = \frac{1}{2\pi} \int_{-\infty}^{\infty} \exp\left[i \left(E_i + \hbar\omega - E_f\right) t\right] dt, \tag{3.12}$$

we can re-write the scattering cross section as [40]

$$\begin{aligned}
\frac{\partial^2\sigma}{\partial\Omega\partial\omega} &= \left(\frac{e^2}{m_0c^2}\right)^2\left(\frac{\omega_S}{\omega_I}\right)^2(\hat{\epsilon}_I\cdot\hat{\epsilon}_S)^2 \\
&\quad\times\frac{1}{2\pi}\int_{-\infty}^{\infty}dte^{i\omega t}\sum_f\langle i|\,\hat{n}_{\mathbf{q}}\,|f\rangle\,e^{i\left(E_i-E_f\right)t}\,\langle f|\,\hat{n}_{-\mathbf{q}}\,|i\rangle \\
&= \left(\frac{e^2}{m_0c^2}\right)^2\left(\frac{\omega_S}{\omega_I}\right)^2(\hat{\epsilon}_I\cdot\hat{\epsilon}_S)^2 \\
&\quad\times\frac{1}{2\pi}\int_{-\infty}^{\infty}dte^{i\omega t}\sum_f\langle i|\,e^{iHt}\hat{n}_{\mathbf{q}}e^{-iHt}\,|f\rangle\,\langle f|\,\hat{n}_{-\mathbf{q}}\,|i\rangle \\
&= \left(\frac{e^2}{m_0c^2}\right)^2\left(\frac{\omega_S}{\omega_I}\right)^2(\hat{\epsilon}_I\cdot\hat{\epsilon}_S)^2 \\
&\quad\times\frac{1}{2\pi}\int_{-\infty}^{\infty}dte^{i\omega t}\,\langle\hat{n}\,(\mathbf{q},t)\,\hat{n}\,(\mathbf{q},0)\rangle\,, \qquad (3.13)
\end{aligned}$$

and finally we get

$$\frac{\partial^2\sigma}{\partial\Omega\partial\omega}=\left(\frac{e^2}{m_0c^2}\right)^2\left(\frac{\omega_S}{\omega_I}\right)^2(\hat{\epsilon}_I\cdot\hat{\epsilon}_S)^2\,S\,(\mathbf{q},\omega)\,, \qquad (3.14)$$

where

$$S\,(\mathbf{q},\omega)=\frac{1}{2\pi}\int_{-\infty}^{\infty}dte^{i\omega t}\,\langle\hat{n}\,(\mathbf{q},t)\,\hat{n}\,(\mathbf{q},0)\rangle\,. \qquad (3.15)$$

$S\,(\mathbf{q},\omega)$ is known as the dynamic structure factor, and it explicitly shows that density fluctuations are responsible for light scattering in a plasma.

The situation of light scattering from a semiconductor plasma is slightly more complicated. The periodicity of the lattice leads to the formation of many electronic energy bands, and in second order perturbation theory, electrons in these bands can undergo transitions through $\mathbf{A}\cdot\mathbf{p}$ term. In semiconductors, this scattering process can become significant, and we must therefore include it in any discussion of the scattering cross section. Let us assume we are dealing with a semiconductor that has a parabolic conduction band; this is a

reasonable assumption for a material like GaAs. If we are non-resonantly photo-exciting the semiconductor we may write an effective Hamiltonian that essentially combines the $\mathbf{A}^2$ and $\mathbf{A} \cdot \mathbf{p}$ contributions as [38]:

$$\hat{H}_{eff} = \frac{e^2}{m_0 c^2} \left(\hat{\epsilon}_I \cdot m_0 \mathbf{m}^{-1} \cdot \hat{\epsilon}_S \right) \hat{A}_I \hat{A}_S^{\dagger} \exp\left(-i\omega t\right) \hat{n}_{-\mathbf{q}} + H.C., \tag{3.16}$$

where $\mathbf{m}^{-1}$ is the inverse effective mass tensor describing the conduction band. The scattering cross section is now [2]

$$\frac{\partial^2 \sigma}{\partial \Omega \partial \omega} = \left(\frac{e^2}{m_0 c^2} \right)^2 m_0^2 \left(\frac{\omega_S}{\omega_I} \right)^2 \left(\hat{\epsilon}_I \cdot \mathbf{m}^{-1} \cdot \hat{\epsilon}_S \right)^2 S\left(\mathbf{q}, \omega\right). \tag{3.17}$$

$S\left(\mathbf{q}, \omega\right)$ is again given by Equation (3.15). The key to understanding light scattering from a plasma lies in evaluating the dynamic structure factor given the nature of the plasma under consideration.

3.3 The fluctuation dissipation theorem

The $\left\langle \hat{n}\left(\mathbf{q}, t\right) \hat{n}^{\dagger}\left(\mathbf{q}, 0\right) \right\rangle$ term appearing in Equation (3.15) is taken over initial and final many-electron states. However, because the exact form of these states is unknown, we cannot calculate an exact analytical solution for the structure factor. What we can do, however, is relate the thermal fluctuations of the plasma density to the dielectric function of the plasma using the fluctuation dissipation theorem. In general, in the absence of an applied force, an observable in a system will vary randomly about it's mean value; we refer to these as thermal fluctuations. Now, if we were to apply a force to the system, the observable would be subject to a driven force that must be dissipated by some systematic resistance. It turns out that this resistive response originates from the same source as the thermal fluctuations of the system. As such, the fluctuation dissipation theorem allows us to relate the systematic response to the thermal fluctuations of the observable.

The mathematical formulation of the fluctuation dissipation theorem was first done by Callen and Welton [41]. In general, we wish to connect some generalized "force" to the thermal fluctuations of an observable that occur in the absence of any perturbations. Our ability to do this is contingent on the observable and "force" being conjugates of each other such that, when multiplied, they represent a Hamiltonian such as [42],

$$H = X\left(\mathbf{r}, t\right) F\left(\mathbf{r}, t\right). \tag{3.18}$$

In Fourier space, the observable and force are linked as [42]

$$X\left(\mathbf{q}, \omega\right) = T(\mathbf{q}, \omega) F\left(\mathbf{q}, \omega\right), \tag{3.19}$$

where $T\left(\mathbf{q}, \omega\right)$ is the linear response function of the system. The central result of the fluctuation dissipation theorem is that, for Stokes scattering [42, 43],

$$\frac{1}{2\pi} \int_{-\infty}^{\infty} dt \exp\left(i\omega t\right) \left\langle \hat{X}\left(\mathbf{q}, t\right) \hat{X}^{\dagger}\left(\mathbf{q}, 0\right) \right\rangle = \frac{\hbar}{\pi} \left(n\left(\omega\right) + 1\right) \Im\left\{T\left(\mathbf{q}, \omega\right)\right\}, \tag{3.20}$$

where $n\left(\omega\right)$ is the Bose-Einstein factor. Equation (3.20) allows us to relate the power spectrum of the thermal fluctuation of the observable X to the imaginary, or dissipative, part of the response function T.

3.4 The single-component plasma

In order to apply the fluctuation dissipation theorem to evaluate the structure factor for a single component plasma, I will follow the treatment in Ref. [2]. Poisson's equation tells us that the polarization and plasma density operators are related by

$$\nabla \cdot \mathbf{P}\left(\mathbf{r}, t\right) = -e\hat{n}\left(\mathbf{r}, t\right). \tag{3.21}$$

Taking the spatial Fourier transform of the both sides of Equation (3.21) allows us to write

$$\hat{n}\left(\mathbf{q},t\right)=-\frac{i}{e}\mathbf{q}\cdot\mathbf{P}\left(\mathbf{q},t\right). \tag{3.22}$$

We can then re-write the structure factor in (3.15) as

$$\begin{aligned} S\left(\mathbf{q},\omega\right) &= \frac{1}{2\pi}\int_{-\infty}^{\infty}dt\exp\left(i\omega t\right)\left\langle \hat{n}\left(\mathbf{q},t\right)\hat{n}^{\dagger}\left(\mathbf{q},0\right)\right\rangle \\ &= \frac{1}{2\pi e^{2}}\int_{-\infty}^{\infty}dt\exp\left(i\omega t\right)\left\langle \mathbf{q}\cdot\mathbf{P}\left(\mathbf{q},t\right)\mathbf{q}\cdot\mathbf{P}^{\dagger}\left(\mathbf{q},t\right)\right\rangle \\ &= \frac{q^{2}}{2\pi e^{2}}\int_{-\infty}^{\infty}dt\exp\left(i\omega t\right)\left\langle \hat{P}\left(\mathbf{q},t\right)\hat{P}^{\dagger}\left(\mathbf{q},t\right)\right\rangle . \end{aligned} \tag{3.23}$$

In the last step, we have assumed that $\mathbf{q}$ is parallel to $\mathbf{P}$. Let us set $\hat{X}=\mathbf{P}$ and $F=\mathbf{D}$ (the externally applied field). Then, using Equation (3.20) and assuming that $\mathbf{P}$, $\mathbf{D}$, and $\mathbf{q}$ are parallel, we can write

$$V\hat{P}\left(\mathbf{q},\omega\right)=T\left(\mathbf{q},\omega\right)D\left(\mathbf{q},\omega\right). \tag{3.24}$$

The electric displacement is related to the total field and polarization by the constitutive relation:

$$\mathbf{D}\left(\mathbf{q},\omega\right)=\epsilon_{\infty}\mathbf{E}\left(\mathbf{q},\omega\right)+4\pi\mathbf{P}\left(\mathbf{q},\omega\right). \tag{3.25}$$

Also, by using the susceptibility of the plasma, we can relate the polarization to the total field by writing

$$\mathbf{P}\left(\mathbf{q},\omega\right)=\chi\left(\mathbf{q},\omega\right)\mathbf{E}\left(\mathbf{q},\omega\right). \tag{3.26}$$

Combining (3.24)-(3.27), we obtain

$$T\left(\mathbf{q},\omega\right)=\frac{\chi\left(\mathbf{q},\omega\right)}{\epsilon_{\infty}+4\pi\chi\left(\mathbf{q},\omega\right)}=\frac{\chi\left(\mathbf{q},\omega\right)}{\epsilon\left(\mathbf{q},\omega\right)}. \tag{3.27}$$

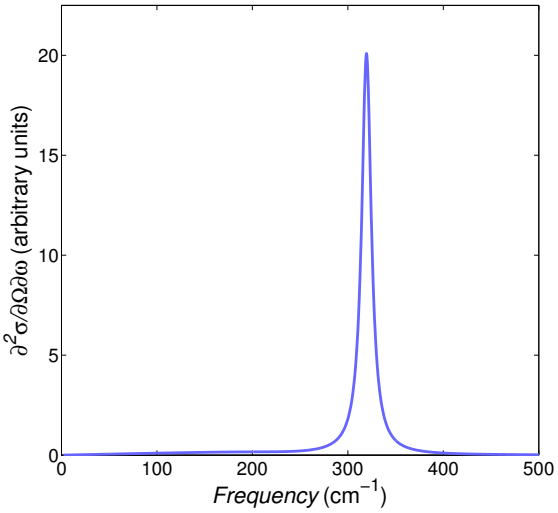

Figure 3.4: The scattering cross section for a one component plasma $n = 7 \times 10^{17}$ cm^{-3}, $q = 7.33 \times 10^5$ cm^{-1}, $T = 100$ K, $\Gamma = 1.3$ meV.

Finally, we can write the expression for the scattering cross section of a single component plasma by combining (3.17), (3.20), and (3.23)-(3.27) to get

$$\frac{\partial^2\sigma}{\partial\Omega\partial\omega} = \left(\frac{e^2}{m_0c^2}\right)^2 m_0^2 \left(\frac{\omega_S}{\omega_I}\right)^2 \left(\hat{\epsilon}_S \cdot \mathbf{m}^{-1} \cdot \hat{\epsilon}_I\right)^2 \frac{\hbar q^2}{\pi e^2} \left(n\left(\omega\right)+1\right) \Im\left\{\frac{\chi\left(\mathbf{q},\omega\right)}{\epsilon\left(\mathbf{q},\omega\right)}\right\}. \quad (3.28)$$

We can evaluate the susceptibility and dielectric function appearing in Equation (3.28) using the RPA expressions developed in Chapter 2. Since we are interested in the Γ-point electron behavior in GaAs, we can assume that the conduction band is parabolic and we can take $\mathbf{m}^{-1}$ to be a diagonal matrix if we orient the cartesian coordinate system with the principal axis. Accordingly, the scattering cross-section can be non-zero only for polarized configurations in which $\hat{\epsilon_L} = \hat{\epsilon_S}$. In Figure 3.4, I have plotted the scattering cross section for a simple electron plasma in GaAs. As expected, since the system is only a free-particle-like plasma comprised of electrons, there should be only one collective oscillation branch, and accordingly, we see a single well defined peak corresponding to the optical plasmon.

3.5 The multi-component plasma

Thus far, we have restricted ourselves to the consideration of a plasma composed of a single charge species. Furthermore, despite dealing with a plasma in a crystal structure, we have not considered the susceptibility due to lattice oscillations, and how this may affect the scattering cross section. In order to do this, we have to extend our treatment of the scattering cross section to the case of a plasma comprised of many charge species. The generalization of (3.17) was put forth by McWhorter and is given by [2]

$$\frac{\partial^2\sigma}{\partial\Omega\partial\omega} = \left(\frac{e^2}{c^2}\right)^2 \left(\frac{\omega_S}{\omega_I}\right)^2 \sum_{a,b} \left(\hat{\epsilon}_I \cdot \mathbf{m}_a^{-1} \cdot \hat{\epsilon}_S\right) \left(\hat{\epsilon}_I \cdot \mathbf{m}_b^{-1} \cdot \hat{\epsilon}_S\right) S_{ab}\left(\mathbf{q},\omega\right), \tag{3.29}$$

with

$$S_{ab}\left(\mathbf{q},\omega\right) = \frac{1}{2\pi} \int_{-\infty}^{\infty} dt \exp\left(i\omega t\right) \left\langle \hat{n}_a\left(\mathbf{q},t\right) \hat{n}_b^{\dagger}\left(\mathbf{q},0\right) \right\rangle, \tag{3.30}$$

where a and b label the charge species. The structure factor is now a tensor, each element corresponding to the contribution of a particular species combination. We can now apply the fluctuation dissipation theorem. The polarization of the plasma will be the sum of contributions due to each plasma species. Likewise, the response function will also be a tensor linking the polarization of a species a with the displacement field associated with species b (a and b may be the same species). Specifically, we can write [2]

$$\mathbf{P}_a\left(\mathbf{q},\omega\right) = \sum_b \mathbf{T}_{ab}\left(\mathbf{q},\omega\right) \mathbf{D}_b\left(\mathbf{q},\omega\right) \tag{3.31}$$

and

$$\mathbf{D}_a\left(\mathbf{q},\omega\right) = \epsilon_\infty \mathbf{E}_a\left(\mathbf{q},\omega\right) + 4\pi \sum_b \mathbf{P}_b\left(\mathbf{q},\omega\right). \tag{3.32}$$

Each species' polarization is still proportional to the corresponding field through the species susceptibility as [2]

$$\mathbf{P}_a\left(\mathbf{q},\omega\right) = \chi_a\left(\mathbf{q},\omega\right) \mathbf{E}_a\left(\mathbf{q},\omega\right). \tag{3.33}$$

In general, the evaluation of the response function can be quite complicated, particularly for cases where the different species are defined by different principal axes as is the case for materials like n-Ge and n-Si [38, 44]. However, for the conduction band of GaAs, this is not an issue since the effective mass tensor is diagonal near the Γ-point. In this case, the response function between species a and b is given by [2]

$$T_{ab}\left(\mathbf{q},\omega\right)=\left[\chi_{a}\left(\mathbf{q},\omega\right)-4\pi\frac{\chi_{a}\left(\mathbf{q},\omega\right)\chi_{b}\left(\mathbf{q},\omega\right)}{\epsilon\left(\mathbf{q},\omega\right)}\right], \tag{3.34}$$

where

$$\epsilon\left(\mathbf{q},\omega\right)=\epsilon_{\infty}+4\pi\sum_{a}\chi_{a}\left(\mathbf{q},\omega\right) \tag{3.35}$$

can be found using the RPA susceptibility functions.

In theory, the scattering cross section in Equation (3.29) can be evaluated for each combination of species in the multi-component plasma. However, since I am working with GaAs, we can take advantage of certain material properties to simplify the problem. In particular, the conduction band electrons have a much smaller effective mass than the heavy and light holes. Since the scattering process is the result of an effective $\mathbf{A}^2$ term, the smaller effective mass of the electrons will greatly enhance their contribution to the scattering relative to the holes through the inverse effective mass terms. For this reason, the scattering cross section will be dominated by the electronic response.

3.6 A note on resonance

In deriving the preceding expression, we began with the assumption that we were not using light on resonance with any gap of the semiconductor. This, however, is typically not valid when generating a high density photoexcited plasma. Blum, Hamilton, and McWhorter have developed the theory to deal with scattering cross sections in near-resonant conditions [45, 46]. The primary result is that the scattering spectrum is enhanced under resonant

photoexcitation. This introduces a few problems. Primarily, we need a whole new set of scattering cross section expressions to treat resonant phenomena. The approach typically taken is to define a new effective Hamiltonian for the scattering process; one that takes into account both band anisotropy and spin orbit effects that play a role in certain single particle excitations. This is done by changing the density fluctuation to a generalized pair operator defined as [45]

$$\hat{n}' = \sum_{\alpha,\beta} \gamma_{\alpha,\beta} \hat{c}_\beta^\dagger \hat{c}_\alpha, \tag{3.36}$$

allowing us to write the scattering cross section as [2]

$$\frac{\partial^2 \sigma}{\partial \Omega \partial \omega} = \left(\frac{e^2}{m_0 c^2}\right)^2 \frac{\omega_S}{\omega_I} \frac{V^2}{2\pi} \int_{-\infty}^{\infty} e^{i\omega t} \left\langle \hat{n}'(t)\, \hat{n}'(t) \right\rangle dt, \tag{3.37}$$

with

$$\begin{aligned} \gamma_{\alpha,\beta} &= (\hat{\epsilon}_I \cdot \hat{\epsilon}_S) \left\langle \alpha \right| e^{i\mathbf{q}\cdot\mathbf{r}} \left| \beta \right\rangle \\ &\quad + \frac{1}{m_0} \sum_{\beta'} \left[\frac{\left\langle \alpha \right| \hat{\epsilon}_S \cdot \mathbf{p} e^{-i\mathbf{k}_S\cdot\mathbf{r}} \left| \beta' \right\rangle \left\langle \beta' \right| \hat{\epsilon}_I \cdot \mathbf{p} e^{-i\mathbf{k}_I\cdot\mathbf{r}} \left| \beta \right\rangle}{\hbar\omega_I + E_\beta - E_{\beta'}} \right| \\ &\quad \left| + \frac{\left\langle \alpha \right| \hat{\epsilon}_I \cdot \mathbf{p} e^{-i\mathbf{k}_I\cdot\mathbf{r}} \left| \beta' \right\rangle \left\langle \beta' \right| \hat{\epsilon}_S \cdot \mathbf{p} e^{-i\mathbf{k}_S\cdot\mathbf{r}} \left| \beta \right\rangle}{E_\beta - E_{\beta'} - \hbar\omega_S} \right]. \end{aligned} \tag{3.38}$$

In general, the dynamic structure factors of the from of (3.37) are very difficult to calculate. However, if we make the assumptions that $\omega_I \approx \omega_S$ and $E_{\beta'} - E_\beta$ is approximately equal to the band gap, then we can separate $\gamma_{\alpha,\beta}$ into

$$\begin{aligned} \gamma_{\alpha,\beta} &= \hat{\epsilon}_I \cdot \overleftrightarrow{\mathbf{R}} \cdot \hat{\epsilon}_S \left\langle \alpha \right| e^{i\mathbf{q}\cdot\mathbf{r}} \left| \beta \right\rangle \\ &\quad i\left(\hat{\epsilon}_I \times \hat{\epsilon}_S\right) \cdot \overleftrightarrow{\mathbf{B}} \left\langle \alpha \right| e^{i\mathbf{q}\cdot\mathbf{r}} \hat{\sigma} \left| \beta \right\rangle \end{aligned}$$

where $\hat{\sigma}$ is the Pauli spin matrix and $\overleftrightarrow{\mathbf{R}}$ and $\overleftrightarrow{\mathbf{B}}$ describe the resonance enhancement. The result is that we will now have two separate contributions to the scattering cross section, one

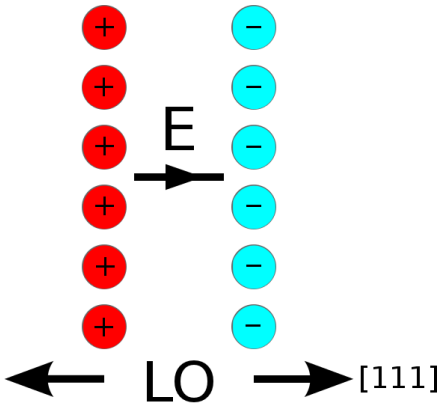

Figure 3.5: Schematic of the longitudinal electric field associated with LO phonons in GaAs.

for polarized and the other for depolarized scattering. In this case, the polarized scattering cross sections are simply modified versions of the one's we have already derived, where the inverse effective mass tensor is replaced by $\overleftrightarrow{\mathbf{R}}/m_0$. The depolarized term is associated with a particular class of single particle excitations, that are quite useful in determining the parameters of the plasma.

3.7 LO phonon-optical plasmon coupled modes

One of the notable features of light scattering spectra in resonantly photoexcited GaAs is related to LO phonon-optical plasmon coupled modes. In polar semiconductors, the LO phonons (see Appendix A) carry a macroscopic longitudinal electric field resulting from displacements of planes of positively and negative charged ions relative to each other as shown in Figure 3.5. The optical plasmon also carries a longitudinal electric field and when the plasmon frequency approaches the phonon frequency at sufficiently high carrier densities, the two oscillators can interact through their macroscopic fields; the optical plasmon screens the longitudinal electric field of the LO phonon [47]. The result of this interaction are two repulsive phonon-plasmon coupled mode branches. In GaAs, the scattering spectrum due to the coupled modes are visible in the polarized configuration (i.e. $\hat{\epsilon}_I \parallel \hat{\epsilon}_S$) if the polarization vector is parallel to the $[0\bar{1}1]$ or $[0\bar{1}\bar{1}]$ crystallographic directions.

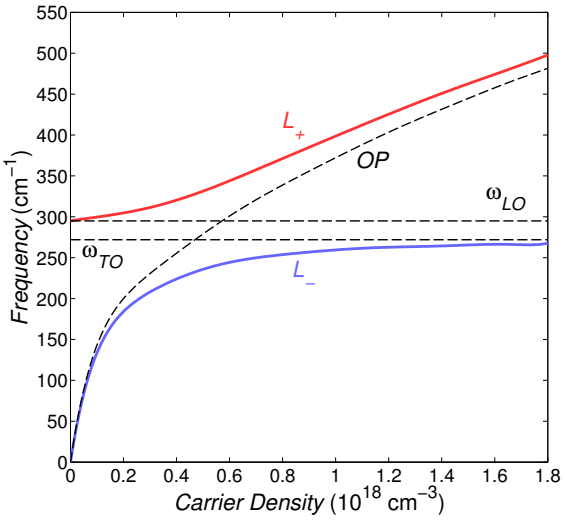

Figure 3.6: The carrier density dependence of the L_- (blue) and L_+ (red) frequencies as a function of carrier density. The conditions used in the theoretical calculation are $q = 7.30 \times 10^5$ cm^{-1}, $T = 100$ K, $\omega_{LO} = 296$ cm^{-1}, $\omega_{TO} = 273$ cm^{-1}, and $\Gamma = 1.3$ meV.

Strictly speaking, the coupled modes exist in a semiconductor even in the absence of a significant hole density. In fact, much of the early experimental work on coupled modes was performed on n-type GaAs where the only significant contributions to the longitudinal dielectric functions come from conduction band electrons and the lattice [5, 4, 3]. In such a system, the dielectric function is

$$\epsilon\left(\mathbf{q},\omega\right) = \epsilon_\infty + 4\pi\chi_e\left(\mathbf{q},\omega\right) + 4\pi\chi_L\left(\mathbf{q},\omega\right), \tag{3.39}$$

where $\chi_e\left(\mathbf{q},\omega\right)$ is calculated from Equations (2.33) and (2.35), and , and $\chi_L\left(\mathbf{q},\omega\right)$ is the lattice susceptibility given by [48]

$$\chi_L = \frac{1}{4\pi}\frac{\omega_{TO}^2\left(\epsilon\left(0\right)-\epsilon_\infty\right)}{\omega_{TO}^2-\left(\omega+i\Gamma_{ph}\right)^2}. \tag{3.40}$$

ω_{LO} and ω_{TO} are the LO and TO phonon frequencies, respectively, Γ_{ph} is the damping of the phonon, and $\epsilon\left(0\right)$ is the static dielectric constant. Since the coupled modes still

involve a collective excitation of the electrons in GaAs (albeit with frequencies different from the optical plasmon), the peak locations of $\Im\{1/\epsilon\}$ correspond to the frequencies of the lower (L_-) and upper (L_+) branch of the coupled modes. Figure3.6 shows the change in ω_{L_-} and ω_{L_+} as a function of carrier density for the specified values of wavevector, carrier temperature, and damping. For lower carrier densities, the L_- mode exhibits plasmon-like behavior while the L_+ is phonon-like slightly up-shifted from LO phonon frequency. At higher carrier densities however, the behavior flips, with the L_- mode behaving as a phonon and the L_+ appearing plasmon-like. As expected, the coupled modes frequencies change significantly with carrier density with the lower and upper branch asymptotically approaching the TO phonon and plasmon frequencies, respectively. This behavior is due to the quasi-chemical potential's effect on the susceptibility. In my experiment, the shift in ω_{L_-} and ω_{L_+} with carrier density served as a metric to assign the density of the photoexcited plasma, which was a necessary step in investigating the acoustic plasmon.

In theory, we can calculate and plot the electronic contribution to the scattering from the coupled modes using (3.29) and (3.34). However, there are two important points that we must consider. First, the plasma consists of conduction band electrons, heavy holes, and light holes. Furthermore, the longitudinal dielectric function of the system has contributions not just from the three carrier species and lattice, but one also due to interband transitions between the light and heavy hole bands [19, 49]. For this reason, we need to construct the dielectric function as

$$\begin{aligned}\epsilon(\mathbf{q},\omega) &= \epsilon_\infty + 4\pi\chi_e(\mathbf{q},\omega) + 4\pi\chi_{hh}(\mathbf{q},\omega) \\ &\quad +4\pi\chi_{lh}(\mathbf{q},\omega) + 4\pi\chi_{inter}(\mathbf{q},\omega) + 4\pi\chi_L(\mathbf{q},\omega).\end{aligned} \tag{3.41}$$

The species susceptibilities are calculated using Equations (2.33)-(2.37) and the lattice susceptibility using Equation (3.40).

We can write the polarized scattering cross section by modifying Equation (3.29), re-

placing the inverse effective mass tensor with a resonance factor given by [46]

$$\overleftrightarrow{\mathbf{R}} = \overleftrightarrow{\mathbf{I}} \left[1 + \frac{3P^2}{m_0} \left(\frac{E_{G1}}{E_{G1}^2 - (\hbar\omega_L)^2} + \frac{E_{G2}}{E_{G2}^2 - (\hbar\omega_L)^2} + \frac{E_{G3}}{E_{G3}^2 - (\hbar\omega_L)^2} \right) \right]. \quad (3.42)$$

Here, $\overleftrightarrow{\mathbf{I}}$ is the identity matrix, P is the interband matrix element, and E_{G1}, E_{G2}, and E_{G3} are the band gap energies between the conduction band and the heavy hole, light hole, and split-off bands, respectively. Since the laser wavelength is very close to E_{G3} in my experiment, only the third term in (3.42) makes a significant contribution to the enhancement effect. Moreover, since the range of wave vectors we are dealing with is small (compared to the edge of the Brillouin zone), we can treat the enhancement term as a constant factor independent of wave vector. Accordingly, we can write the Stokes scattering cross section as

$$\frac{\partial^2\sigma}{\partial\Omega\partial\omega} = \frac{1}{m_0} \left(\frac{e^2}{c^2} \right)^2 \left(\frac{\omega_S}{\omega_L} \right)^2 \left(\hat{\epsilon}_L \cdot \overleftrightarrow{\mathbf{R}} \cdot \hat{\epsilon}_S \right)^2 \frac{\hbar q^2}{\pi e^2} \left(n\left(\omega\right) + 1 \right) \Im \left\{ T_{ee}\left(\mathbf{q}, \omega\right) \right\}, \quad (3.43)$$

where

$$T_{ee}\left(\mathbf{q}, \omega\right) = \left[\chi_e\left(\mathbf{q}, \omega\right) - 4\pi \frac{\chi_e^2\left(\mathbf{q}, \omega\right)}{\epsilon\left(\mathbf{q}, \omega\right)} \right]. \quad (3.44)$$

Just as before, since $\overleftrightarrow{\mathbf{R}}$ is diagonal, the coupled modes only appear in the polarized configuration. Equations (3.43) and (3.44) are the expressions that I used to model the polarized light scattering spectra in my experiment.

In Figure 3.7, I have plotted the electronic component of the scattering cross section due to the L_- and L_+ modes for a plasma of just electrons and the lattice, the inclusion of heavy and light holes, and the subsequent inclusion of interband transitions between the hole bands. We can see that the holes cause a noticeable shift in the coupled mode frequencies and also a broadening effect in the peak associated with the L_+ mode. The former is due to the intraband hole terms, while the latter is due to the interband hole term. The primary conclusion is that in order to compare theoretical predictions of the coupled

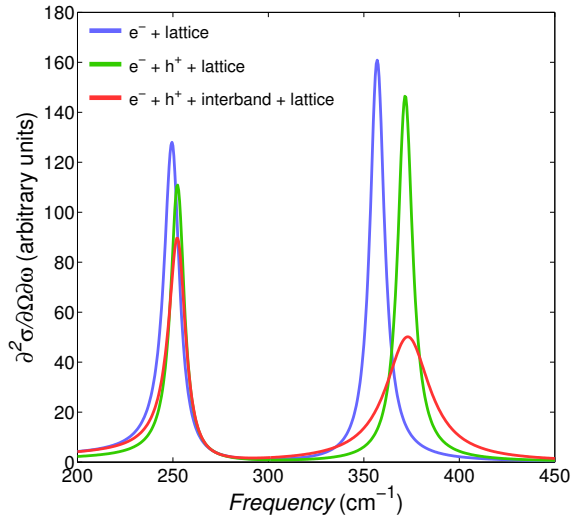

Figure 3.7: Calculated electronic scattering cross sections due to the L_- and L_+ modes for electrons and the lattice (blue), with holes (green), and also with hole interband transitions (red). The inclusion of the hole terms causes a shift in the peak locations and the interband term causes a broadening of the L_+ peak. The conditions used in the theoretical calculation are $q = 7.30\times10^5\text{cm}^{-1}$, $T = 100\text{K}$, $\omega_{LO} = 296\text{cm}^{-1}$, $\omega_{TO} = 273\text{cm}^{-1}$, and $\Gamma = 1.3\text{meV}$.

mode behavior to experimental results, we must include the contributions of holes to the dielectric function.

3.8 Single particle excitations

Single particle excitations are the second major class of phenomenon that are visible in resonant light scattering experiments. In general, single particle excitations are those where a carrier just below the quasi-Fermi energy level is excited to a state just above the level. In light scattering spectra, there are generally two major contributions to the SPE: spin density (SDF) and energy density fluctuations (EDF). The former is particularly important since, at the large carrier densities typically created under resonant photoexcitation, they are unscreened and the associated scattering cross section can be very large [46]. As we shall see, scattering from SDFs appears in the depolarized configuration and we can use it to extract several important plasma parameters, chief among them the carrier temperature.

Scattering from spin density fluctuations occurs through spin-orbit coupling. Here, the $\mathbf{p} \cdot \mathbf{A}$ terms in the electron-radiation Hamiltonian allows light to induce spin flips in electrons via virtual transitions. Much like Equation (3.16), we can write the effective Hamiltonian for the process in the absence of magnetic fields as [2]

$$\hat{H}_{eff}^{SDF} = i\frac{e^2}{2m_0}\left(\hat{\epsilon}_I \times \hat{\epsilon}_S\right) \cdot \overleftrightarrow{\mathbf{B}} \cdot \hat{\epsilon}_\mu \left(\frac{\hat{n}_{\mathbf{q}\uparrow} - \hat{n}_{\mathbf{q}\downarrow}}{2}\right) \hat{A}_I \hat{A}_S^\dagger, \tag{3.45}$$

where $\hat{\epsilon}_\mu$ is a unit vector along a cartesian direction and $\hat{n}_{\mathbf{q}\uparrow}$ ($\hat{n}_{\mathbf{q}\downarrow}$) is the number density operator for up (down) spins. $\overleftrightarrow{\mathbf{B}}$ is a resonance enhancement term that is analogous to $\overleftrightarrow{\mathbf{R}}$ appearing in (3.43). given by [46]

$$\overleftrightarrow{\mathbf{B}} = \frac{P^2 \hbar\omega_I}{3m_0} \overleftrightarrow{\mathbf{I}} \left\{ \frac{1}{E_{G1}^2 - (\hbar\omega_L)^2} + \frac{1}{E_{G2}^2 - (\hbar\omega_L)^2} - \frac{2}{E_{G3}^2 - (\hbar\omega_L)^2} \right\}. \tag{3.46}$$

Equation (3.45) tells us that SDF scattering should only appear when the incident and scattered light polarizations are orthogonal. Also, since any spin flip up reduces the occupation number of a spin down electron, the net electron density fluctuation $\hat{n}_{\mathbf{q}} = \hat{n}_{\mathbf{q}\uparrow} + \hat{n}_{\mathbf{q}\downarrow}$ does not change. As a result, there is no collective excitation involved in SDFs, and the scattering process has a single particle character.

The general expression for the scattering cross section from spin density fluctuations was developed by Hamilton and McWhorter [46]. If the wavevector dependence of the resonance term is ignored, the electronic SDF Stokes scattering cross section is [2]

$$\begin{aligned} \frac{\partial^2 \sigma}{\partial\Omega \partial\omega} &= \left(\frac{e^2}{m_0 c^2}\right)^2 \left(\frac{\omega_S}{\omega_L}\right)^2 \frac{1}{4e^2} \frac{\hbar}{\pi^2} q^2 \left| \left(\hat{\epsilon}_L \times \hat{\epsilon}_S\right) \cdot \overleftrightarrow{\mathbf{B}} \cdot \hat{\epsilon}_\mu \right|^2 \\ &\quad \cdot \left(n\left(\omega\right) + 1\right) \Im\left\{\chi_e\left(\mathbf{q}, \omega\right)\right\}. \end{aligned} \tag{3.47}$$

Pinczuk et al. have noted that treating the resonance term as a constant does lead to shifts in the calculated spectrum relative to experimental results [50]. However, these shifts are small enough that taking the simplified expression given by (3.47) is a reasonable approx-

imation. Light scattering from SDFs is useful in my case for three main reasons. First, scattering from SDFs occur in the depolarized configuration. As a result, there is no need to contend with the subtraction of the coupled mode scattering component prior to extracting the relevant plasma parameters. Second, the lineshape of the SDFs provides a direct measure of the carrier temperature from the anti-Stokes-Stokes ratio. Lastly, it provides another method by which we can assign the carrier density and damping since we can calculate χ_e to see how it depends on these parameters.

There is also a polarized component of SPE, and the usually weak polarized signal can become quite strong in cases where the carrier density and temperature are sufficiently high [50]. Additionally, the lineshape of the polarized SPE can be affected, since the anisotropies in the band can have a significant effect on the resonance enhancement term. Unfortunately, analytical treatments of polarized SPE are complicated and most methods only allow for a qualitative description of the enhancement effects [51].

3.9 Acoustic plasmons

The last major feature in the scattered light spectra, the one central to this work, comes from acoustic plasmons. Since acoustic plasmons are another branch of collective plasma oscillations the scattering cross section is determined by expressions developed for the electronic contribution to polarized scattering from the multicomponent plasma. For the purposes of this work, the main question lies in how the wavevector and plasma parameters change the scattering cross section associated with the acoustic plasmon. Figure 3.8(a) shows a contour plot of the carrier density dependence of the scattering cross section of an EHP in GaAs. As expected, the L_- and L_+ modes show behavior commensurate with Figure 3.6 and the acoustic plasmon shows a fractional power law behavior with carrier density as discussed in Chapter 2. Figure 3.8(b) shows the scattering cross section's dependence on the wavevector. While we see that the coupled modes cross sections do not

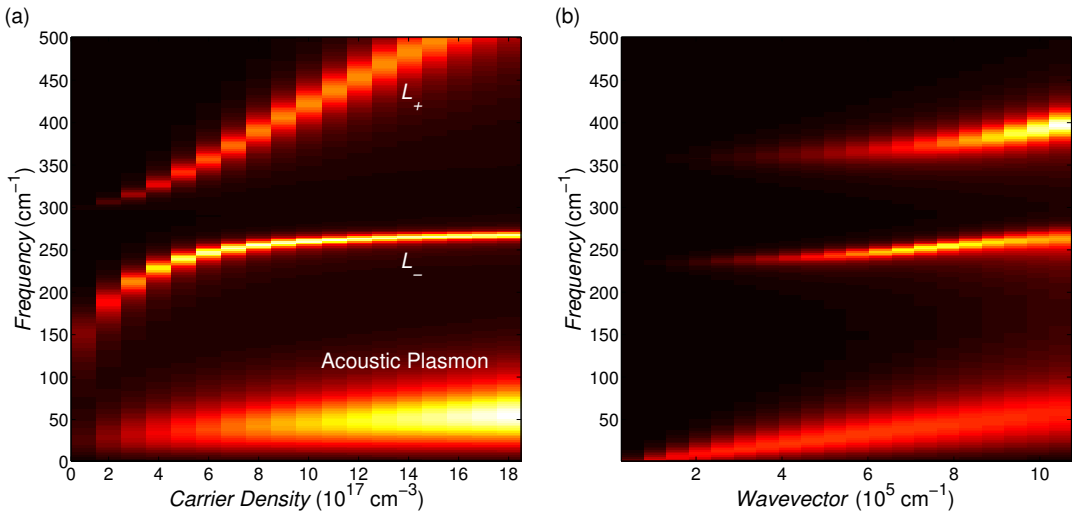

Figure 3.8: (a) Contour plot showing the carrier density dependence of the scattering cross section for $q = 7.3\times10^5$ cm^{-1}, $T = 100$ K, and $\Gamma = 1.3$ meV and (b) contour plot showing the dispersion of the scattering cross section for $N = 7.0 \times 10^{17}$ cm^{-3}, $T = 100$ K, and $\Gamma = 1.3$ meV

vary significantly for small q, the acoustic plasmon cross section shows a linear dependence with wavevector.

Having identified how the scattering cross section varies with wave vector and plasma density, it is now necessary for us to consider the wavevector, q, appearing in the cross section expressions. For a thick sample, finite size effects are irrelevant and, subsequently, we can disregard confinement of the modes. In this case, the relevant wavevector in the scattering process is determined by k-conservation. For backscattering, this means that $q = 2k_I = 4\pi n/\lambda_I$, where n is the index of material and λ_I is the wavelength of the incident light. Moreover, for an optical mode, the dispersion is virtually flat near the center of the Brillouin zone, so the choice of q is all but irrelevant near the Γ-point.

The acoustic plasmon, however, is entirely another matter. As I showed in Chapter 2, the form of the density fluctuation associated with acoustic plasmons in a slab are standing waves with $q = m\pi/d$, where d is the slab thickness. As a result, in a thick layer, the spacing between adjacent modes is small, and light may couple strongly to a mode that satisfies k-conservation. However, for a thin sample, the large spacing between the modes causes

wavevector conservation to breakdown since there may not be a mode with appropriate q. This allows the light to couple to "forbidden" modes over a range of q values [52]. Now, if the dispersion of the excitation was flat, the frequency variation between these modes would be negligible and spectrally, we would see nothing different from the case of a thick sample. However, since the acoustic plasmon has a linear dispersion with a relatively large group velocity, the frequency separation can become quite large between adjacent modes. As a result, we would see spectra that differs from the bulk-case. The number of accessible "forbidden" modes and the efficiency with which light couples to them is determined by the details of the scattering process. In Chapter 5, I will demonstrate that we can exploit an analogy between LA phonons and acoustic plasmons to determine the scattering spectra from acoustic plasmons in thin samples.

3.10 Calculating the susceptibilities

In the preceding sections, we have seen several scattering cross sections for GaAs given a set of electron-hole plasma parameters. However, we have yet to consider the energy denominators appearing in the susceptibility functions used to form the longitudinal dielectric function. The simplest approach is to treat the electron and hole bands as parabolic, defined by some effective mass. When combined with the RPA expressions we derived in Chapter 2, the resulting functions are known as the Lindhard susceptibilities. In general, this approach, though qualitatively sound, fails to reproduce the substantive effects of band anisotropies and non-parabolicities on the acoustic plasmon and coupled mode scattering cross sections. In Figure 3.9 I have plotted the band structure of GaAs calculated with a 30-band model using a direct diagonalization of the $\mathbf{k} \cdot \mathbf{p}$ Hamiltonian [53, 54]. As we can see, the conduction band electrons and light holes are isotropic near the Γ-point, though the latter is non-parabolic. In contrast, the heavy hole band, though parabolic, is anisotropic and depends strongly upon the crystallographic direction. Thus, it is clear that in order to

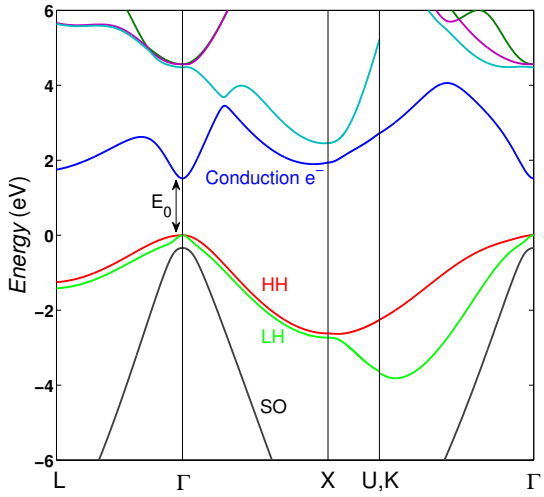

Figure 3.9: Band structure of GaAs at $T = 0$ K calculated using a direct diagonalization of a 30-band $\mathbf{k} \cdot \mathbf{p}$ model.

make accurate quantitative comparisons between my experiment and theory, I must take into account the complexity in the band structure of GaAs.

There are many effective approaches to compute susceptibility integrals of the form of Equations (2.34) and (2.36) that extend over the entire Brillouin zone. In one such method, the Brillouin zone is adaptively meshed and divided into tetrahedral elements [55, 56]. The relevant band energies are evaluated at the vertices of each tetrahedron (using, for example, the $\mathbf{k} \cdot \mathbf{p}$ method) and these values are used to analytically sum the integrand over the Brillouin zone using interpolation inside each tetrahedron. By all accounts, this method is as exact as computationally permissible. It does, however, suffer from a major drawback. This has to do with the difficulty in handling situations where the temperature is non-zero. In this case, the quasi-Fermi surface is diffuse due to the smearing of the edge by the Fermi-Dirac distribution. Several methods exist to adapt the tetrahedron method to account for finite temperature effects, but in general, they are difficult to implement and computationally intensive [57].

Another approach to computing the susceptibility integrals, one I have chosen to implement in my work, takes advantage of the particular structure of the 3 bands in question.

Since the conduction band of GaAs is isotropic near the Γ-point, the energy of an electron in this band is only dependent on the magnitude of the wave vector. In this case, performing a full 3D integral is unnecessary. If the wave vector of the excitation ($\mathbf{q}$) is chosen to be along the lab x-axis (the crystallographic $[100]$ direction) then we can reduce the integral to 2π (from the azimuthal integral) times the integrals over k (radial magnitude) and θ (the polar angle). This is because in this case

$$E\left(\mathbf{k}+\mathbf{q}\right) = E\left(k^2+q^2+2kq\cos\theta\right). \tag{3.48}$$

We can then calculate the energy dispersion function using the 30-band $\mathbf{k}\cdot\mathbf{p}$ method along one of the high symmetry directions of GaAs (e.g. $\Gamma \to X$), and since the shape will be the same in any direction from the Γ-point, we can cubically interpolate the band dispersion as necessary by the an adaptive 2D integration method ($integral2$, see [58]). We choose the k-space bounds of the integration so that it extends to the point where the Fermi-Dirac distributions appearing in Equations (2.34) and (2.36) sufficiently suppress the integrand to negligible values. Of course, if the bounds of integration were very large (i.e. a significant fraction of the Brillouin zone edge), then this method would fail since the assumption of isotropy becomes invalid. However, for the region of k-space I was dealing with, this was not an issue, and comparisons with the tetrahedron method showed good agreement. The advantage of this method is that temperature can easily be introduced since the smearing of the quasi-Fermi level is handled adaptively by the integration method. Moreover, this computation is significantly faster than the tetrahedron method allowing for virtually on-the-fly susceptibility calculations that are particularly useful in implementing the iterative method I employ to determine the plasma parameters (discussed in the Chapter 5). Finally, since this method is only contingent upon the band being isotropic, it was also applied to the susceptibility calculations for the light hole.

The case of the heavy hole is more complicated due to the anisotropy of the band. In

this case, since the band energy is not just dictated by the magnitude of the wave vector, we would in fact need to compute a full 3D integral and interpolate the $\mathbf{k}\cdot\mathbf{p}$ calculation in 3 dimensions. This, in fact, is merely a stripped down version of the tetrahedron method and is not as accurate and quite slow. Instead we make use of the fact that, though anisotropic, the heavy hole band is parabolic in the vicinity of the Γ-point for any given direction. Dresselhaus and coworkers proposed an analytical expression for the heavy hole band dispersion based on the assumption that the fermi surface was an elongated spheroid [59]. In this case, the energy band is given by [60]

$$E\left(\mathbf{k}\right) = \frac{\left|A\right|\hbar^2 k^2}{2m_0}\left(1 - g\left(\theta,\phi\right)\right),$$

where

$$g\left(\theta,\phi\right) = \left[\left(\frac{B}{A}\right)^2 + \left(\frac{C}{A}\right)^2 \sin^2\theta\cos^2\theta + \sin^4\theta\cos^2\phi\sin^2\phi\right]^{1/2},$$

and A, B, and C are material specific parameters. With this analytical function, the 3D integral is performed using standard methods. In using this approach for the susceptibility, we are approximating the band more significantly than in the case of the electrons and light holes. However, the enormously reduced computation time, and the still relatively good agreement with the tetrahedron method make this a worthwhile tradeoff.

3.11 Summary

In this Chapter, we have developed the theory of light scattering from plasmas assuming systems comprised of either one or many charge species in a crystal lattice. The scattering cross sections show the emergence of spectral peaks associated with several different phenomena. One involves the interaction of the optical plasmon with LO phonon modes. These are known as the coupled modes and both the frequency and spectral lineshape are

strongly affected by the composition and parameters of the plasma. Additionally, on resonance, we see spectral features associate single particle excitations of electrons, which can emerge in both the polarized and depolarized configurations due to different mechanisms. In plasmas comprised of both electrons and holes, a spectral peak associated with acoustic plasmon emerges. Finally, when modeling these spectra, particularly for comparison to experiments, we must be sure to take into account the shape of the band structure as this may have a significant impact on both peak locations and spectral lineshapes.

CHAPTER 4

Experimental equipment and methods

Most experimental physicists can attest that the collection of data is far from a trivial matter. One would imagine that interpreting the results would be the challenging part, but often, merely obtaining data to analyze can prove to be a most arduous task. Certainly, advancements in equipment and experimental methodologies have made the job easier, but as is often the case, the complex nature of the tools of the trade can sometimes introduce unforeseen subtleties into an otherwise well conceived experiment. In an effort to expose these subtle considerations, I will provide an overview of the various equipment and methods that make light scattering experiments possible. In particular I will focus on CW and pulsed laser systems, and when discussing the latter I will present an overview of the nonlinear phenomena associated with their operation. I will also discuss the issues surrounding pulse width measurement and techniques to combat temporal broadening of ultrashort pulses. Finally, I will provide an overview of the experimental configurations that we typically use in spontaneous and stimulated light scattering studies.

4.1 Laser systems

The most important element in any light scattering experiment is the light source. Today, laser systems are the backbone of the field, used in either a continuous wave (CW) configuration for spontaneous scattering or pulsed configuration for pump-probe studies. As lasers have been in use for decades, the physics and operational theory are well documented.

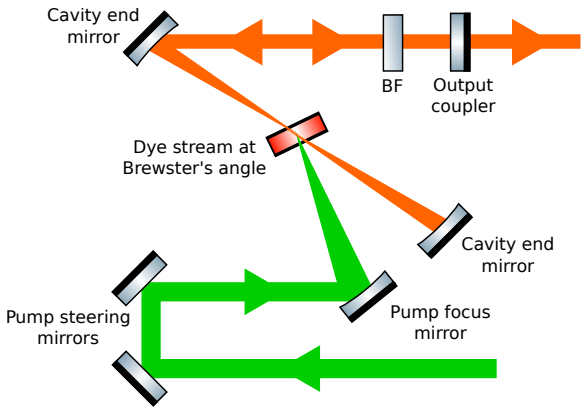

Figure 4.1: Schematic of the CW dye laser system.

However, as they play such an important role in my work, it is worth discussing them in order to gain insight into their operation. As part of my research, I used a tunable CW dye laser for spontaneous scattering and a Ti:Sapphire oscillator, regenerative amplifier, and optical parametric amplifier for pump-probe experiments.

4.1.1 Continuous wave dye laser

CW dye lasers allow us to generate coherent light that we can tune across a wide wavelength range. Figure 4.1 shows a schematic of the laser cavity. The gain medium is a pigment suspended in an appropriate solvent. This solution circulates in a closed loop system through a nozzle which produces a laminar dye stream oriented at Brewster's angle relative to a focused pump beam supplied by another laser source. We can set the operating wavelength range through the choice of dye chemistry. In my experiments, I used DCM dissolved in a 3:2 mixture of ethylene glycol and benzyl alcohol. This mixture provided a tuning range of 608-727 nm with a maximum at 655 nm [61]. The pump source was an Argon-ion gas laser (Spectra-Physics Beamlok 2060) operating in multiline mode, which supplied approximately 5W of CW power.

The basic cavity supports multiple longitudinal modes with a frequency separation of approximately 400 MHz. As a result of this and the spectrally broad gain curve, the un-

tuned laser has a bandwidth that is broad and highly structured. This is unsuitable for spectroscopy, particularly in cases where the features of interest are very close to the central frequency of the laser. To resolve this issue, a birefringent filter is placed in the cavity to both narrow the linewidth and allow for continuous wavelength tuning across most of the gain curve. In practice, at 647 nm, the FWHM of the laser line was approximately 2.5 cm^{-1}.

4.1.2 The Ti:Sapphire Oscillator

In order to perform typical pump probe experiments, we need a source of femtosecond laser pulses. In the last several years, Ti:Sapphire oscillators have become a widely used system for this purpose, routinely producing sub-80 fs pulses tunable in the 780-820 nm range with MHz repetition rates.

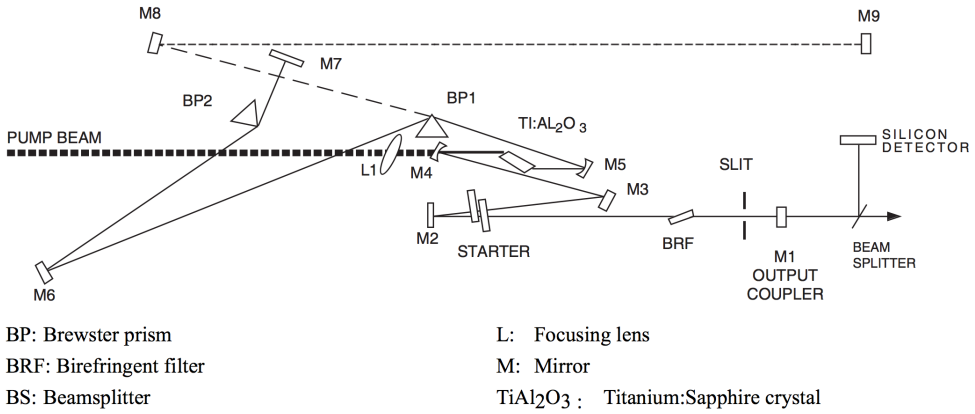

Figure 4.2: A schematic of the MIRA Ti:Sapphire oscillator, reproduced from [62].

Figure 4.2 shows a schematic of the oscillator I use in my experiments (Coherent MIRA). A diode pumped solid state (DPSS) laser (Coherent Verdi G-5) excites the Ti:Sapphire crystal and light circulating within the cavity intensifies via stimulated emission. Since light propagating perpendicular to the reflectors does not walk out of the bounds of the cavity after multiple trips, it is preferentially amplified; this accounts for the strong

directionality of the laser's output. The optical distance between the high reflector and the output coupler defines the length of the optical cavity. The cavity supports many longitudinal modes, akin to the standing modes of a string, that satisfy the condition that the cavity length is equivalent to an integer multiple of the half-wavelength of the mode. In practice, the lasing cavity supports many of these modes simultaneously, and this fact is integral to the concept of mode-locking. If the phase relationships between these modes are random, then the output will be CW-like with random fluctuations. If, however, the various modes have a particular phase relationship with respect to one another, they can constructively and destructively interfere in such a way as to generate pulses of light. This phase relationship can be established either actively or passively; the MIRA uses the latter technique.

Passive mode-locking takes advantage the nonlinear optical properties of the Ti:Sapphire crystal. In pulsed operation, the peak intensity of the pulse is large enough to cause a local change in the refractive index of the gain medium (through the intensity dependence of the refractive index). As a result, the pulsed beam focuses as though it were passing through a gradient index lens; this effect is known as Kerr lensing. Kerr lensing causes the pulsed beam to have a smaller diameter within the cavity compared to the CW beam, since the intensity of the latter is too low to trigger the effect. An adjustable mechanical slit in the optical cavity can then block the CW beam, while still passing the pulsed beam. In this way, only the pulsed beam circulates through the cavity and the output of the laser system will be a pulse train with a repetition rate defined by the cavity length.

In order to initiate mode-locking, the random fluctuations that exist in the cavity prior to mode-locking must be large enough to cause Kerr lensing. This can only occur if many longitudinal modes exist simultaneously. In the transient regime, this can be accomplished by quickly changing the angle of a piece of glass in the optical cavity, effectively changing the path length and briefly allowing more modes to exist. Once the fluctuations caused by the addition of these modes is sufficient to cause Kerr lensing, mode-locking initiates and the starting mechanism can be deactivated [62]. The Coherent MIRA is able to generate a

sub-80 fs 76 MHz pulse train in the 780-820 nm range with an average power of 350 mW.

4.1.3 The regenerative amplifier

In my experiments, I need to generate high carrier densities, and this is easiest to accomplish by using light that is on resonance with a direct gap of GaAs. However, the limited wavelength range of the oscillator makes it impossible to do this using the MIRA pulses directly. For this reason, I used an optical parametric amplifier (Coherent OPA 9400) to generate pulses that can be tuned across the visible spectrum. Since the OPA requires a high energy input pulse, the MIRA pulses must be regeneratively amplified (using a Coherent RegA 9000). Figure 4.3 shows a schematic of the RegA 9000 system. A diode pumped

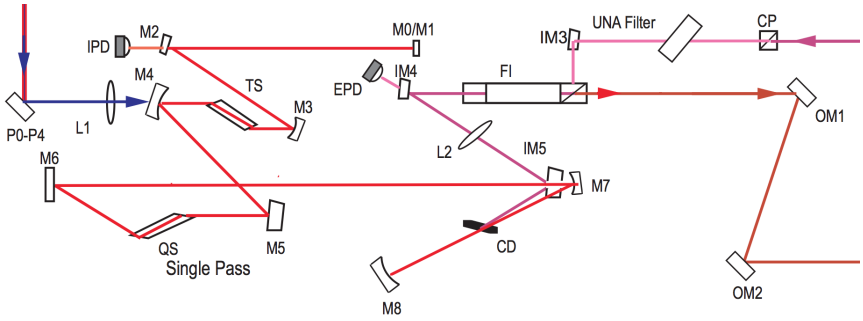

Figure 4.3: Schematic of the RegA 9000, reproduced from [63].

solid state laser (Coherent Verdi V10) supplies a 10W beam used to pump the Ti:Sapphire crystal in the cavity. The Q-switch prevents spontaneous lasing in the cavity. At a certain time, the Q-switch is deactivated and a single pulse from the MIRA is injected into the amplifier by the cavity dumper. This pulse makes several round trips of the cavity and amplifies on each pass through the Ti:Sapphire crystal. Once the pulse has depleted the gain of the crystal, the cavity dumper ejects the pulse. A Faraday isolator separates the injected and ejected pulses. In my experiment, I operated the RegA at a repetition rate of 250 kHz to produce 800 nm pulses with a temporal width less than 80 fs. The average power of the pulse train was approximately 1.2 W corresponding to a pulse energy of 4.8 μJ.

Figure 4.4 shows a temporal schematic of the Q-switch and cavity dumper timing. The

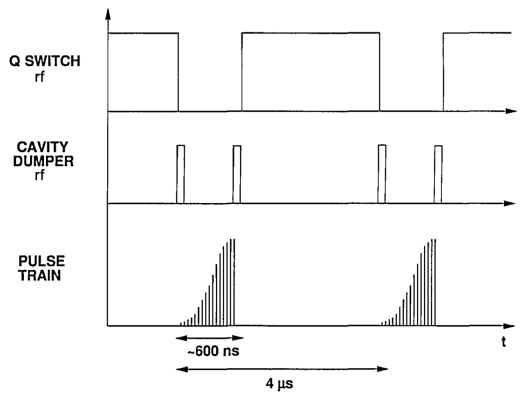

Figure 4.4: Timing of the Q-switch and cavity dumper in the RegA, reproduced from [64].

Q-switch ensures that lasing within the amplifier cavity only occurs when a pulse is injected. It consists of a TeO_2 crystal fitted with a PZT transducer that generates an 80 MHz acoustic wave within the crystal. This wave is aligned at the Bragg-angle with respect to the incident beam so that some of the light is Bragg-diffracted out of the optical path by the acoustic wave; this small loss is sufficient to prevent spontaneous lasing. When a pulse is injected by the cavity dumper, the RF signal to the Q-switch is tuned off and the pulse is amplified as it makes numerous round trips through the cavity. Once the amplification process is complete, the pulse is ejected, the RF signal to the Q-switch is restored, and the gain of the Ti:sapphire crystal is reestablished.

The cavity dumper controls pulse injection and ejection of the seed pulse. It is also TeO_2 crystal fitted with a PZT transducer aligned at the Bragg-angle. A 380 MHz RF signal supplied to the transducer Bragg-diffracts the pulses in and out of the cavity. At a given time, the controller sends two 380 MHz RF pulses with a 4 µs delay to the cavity dumper. This signal is phase locked to the 76 MHz pulse train generated by the oscillator. The first RF pulse signals the injection of a single optical pulse, and this pulse is amplified on successive round trips through the cavity. Upon gain depletion, the second RF pulse signals the cavity dumper to eject the optical pulse. The number of round trips through the amplifier cavity can be tuned by adjusting the delay between the RF pulses [63].

4.1.4 Optical parametric amplifier

The optical parametric amplifier converts the 800 nm pulse from the RegA into one that can be tuned across the visible and near-IR spectrum. Figure 4.5 shows a schematic of the OPA,

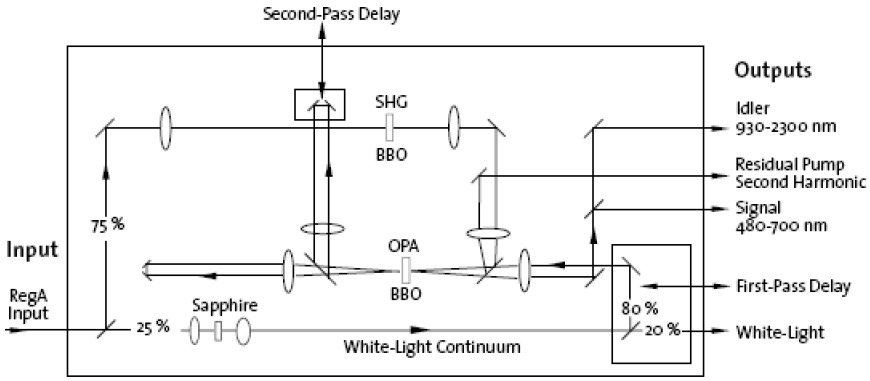

Figure 4.5: A Schematic of the Coherent OPA 9400, reproduced from [65].

which consists of two main paths. The first converts 25% of the 800 nm input pulse into a white light continuum that serves as the seed pulse for the parametric process. The white light continuum has a bandwidth that spans the ultraviolet to the infrared, from which the desired wavelength (the signal) can be amplified. The second path in the OPA serves as the pump for the parametric process. Here, 75% of the 800 nm input pulse is converted to 400 nm through second harmonic generation (SHG) using a ß-Barium-Borate (BBO) crystal. Both the seed and pump then focus onto a second BBO crystal and through parametric amplification, energy is transferred from the pump to the signal. The output of the OPA consists of an amplified signal, a residual pump, and an idler at the frequency difference between the signal and pump [66]. The OPA is capable of generating visible pulses between 400-700 nm with pulse widths less than 75 fs. The pulse train has an average power of 30 - 90 mW at a repetition rate that matches the regenerative amplifier. Below, I will provide a brief description of second harmonic generation, white light continuum generation, and optical parametric amplification.

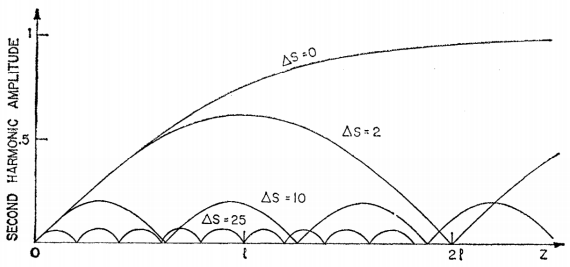

Figure 4.6: Second harmonic amplitude as a function as a function of propagation distance for various phase differences, reproduced from [68]. Here, Δs is a dimensionless phase-difference.

4.1.4.1 Second harmonic generation

Second harmonic generation is a non-linear process in which an input beam at frequency ω (fundamental) is doubled to 2ω (second harmonic). We achieve this frequency doubling by mixing the light-field with itself though the second order susceptibility of a non-centrosymmetric crystal such as BBO. For a light-field of the form $E^{\omega} = A^{\omega} \exp(ik_{\omega}z)$, the coupled wave equations describing the first and second harmonic beams in the slowly varying envelope approximation are [67]

$$\begin{aligned} \frac{dA^{\omega}}{dz} &= i\frac{\omega}{n_{\omega}c}\chi^{(2)}A^{\omega}A^{2\omega *}\exp\left[-i\Delta kz\right] \\ \frac{dA^{2\omega}}{dz} &= i\frac{\omega}{n_{2\omega}c}\chi^{(2)}\left(A^{\omega}\right)^{2}\exp\left[i\Delta kz\right], \end{aligned}$$

where $\Delta k = 2k_{\omega} - k_{2\omega}$ is the wave vector mismatch between the fundamental and second harmonic. The value of Δk plays a crucial role in the efficiency of the second harmonic process. In Figure 4.6, we can see that the maximal amplitude of the second harmonic increases as $\Delta k \to 0$, a limit that we refer to as perfect phase matching. Moreover, in the absence of perfect phase matching, the amplitude of the second harmonic is periodically dependent on the distance z through the crystal.

The perfect phase matching condition for SHG is satisfied when $n_{\omega} = n_{2\omega}$. In the OPA, this condition is satisfied using the fact that the BBO is also a negative uniaxial

crystal. As such, a wave propagating at some angle γ, relative to the optical axis has two eigenpolarizations. The first, known as the ordinary wave, sees a fixed index of refraction as it propagates regardless of the value of γ. The second is the extraordinary wave and it sees a varying refractive index that changes with γ according to [67]

$$\frac{1}{n_e^2(\gamma)} = \frac{\cos^2(\gamma)}{n_o^2} + \frac{\sin^2(\gamma)}{n_E^2}, \tag{4.1}$$

where n_o is the ordinary index and n_E is the maximum value of the extraordinary index. If we choose the fundamental to be the ordinary wave and the the second harmonic to be the extraordinary wave, we must satisfy $n_o^{\omega} = n_e^{2\omega}(\gamma)$, and combining this with (4.1) gives [67]

$$\sin^2\gamma_m = \frac{[n_o^{\omega}]^{-2} - [n_o^{2\omega}]^{-2}}{[n_e^{2\omega}]^{-2} - [n_o^{2\omega}]^{-2}},$$

where γ_m is the phase matching angle. As we shall see later, angle phase matching of this sort is also used to satisfy the condition for the parametric amplification process as well.

4.1.4.2 White light continuum generation

We choose the signal frequency we want to amplify in the optical parametric process from a white light continuum. In the OPA, 25% of the RegA beam focuses onto the surface of a sapphire crystal, with an intensity sufficient to induce self-focusing (SF) of the beam through Kerr lensing. As the beam diameter reduces, diffraction begins to counteract the effects of SF. However, if the intensity of the beam is sufficiently high, the two effects can balance each other leading to the formation of an optical filament with a radius on the order of the wavelength.

The extremely high intensity in the filament causes a further increase in the refractive index through its intensity dependence. This leads to a nonlinear phase change in the pulse given by [67]

$$\phi_{NL}(t) = -\frac{n_2 I(t)\,\omega_0 L}{c},$$

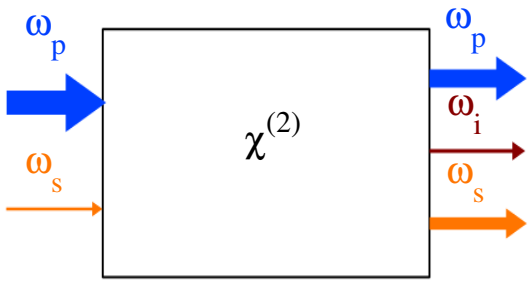

Figure 4.7: Schematic of parametric amplification process.

where ω_0 is the central frequency and L is the length of the crystal. The corresponding time-dependent instantaneous frequency is $\omega(t) = \omega_0 + d\phi/dt$, and given a gaussian intensity of the form $I(t) = I_0 e^{-t^2/\tau^2}$, we can write

$$\omega(t) = \omega_0 + \frac{2n\omega_0 I_0 L}{c\tau^2} t \exp\left(-\frac{t^2}{\tau^2}\right).$$

This means that the leading side of the pulse ($t < 0$) is shifted to lower frequencies, while the trailing side ($t > 0$) is shifted to higher frequencies. Moreover, if the intensity of the pulse is large enough, this effect can broaden the spectrum of the pulse beyond its initial bandwidth. In practice, this broadening is large enough to add wavelength components from 400-700 nm and results in a white light continuum, from which we can select the desired signal frequency.

4.1.4.3 Optical parametric amplification

Once the second harmonic pump and white light continuum have been generated, both beams are used to complete optical parametric amplification. Figure 4.7 shows a schematic of the parametric amplification process. Here, energy is transferred from the pump to the signal. The output of the process is an amplified signal (ω_s) and an idler (ω_i) at the difference frequency between the pump (ω_p) and the signal. The phase matching condition

for parametric amplification is [67]

$$n^{\omega_p} = \frac{\omega_i n^{\omega_i} + \omega_s n^{\omega_s}}{\omega_i + \omega_s}.$$

In the OPA, this phase matching is accomplished by focusing the 400 nm pump and white light seed onto a thin BBO crystal. Setting the idler and signal as the ordinary waves and the pump beam as the extraordinary wave, we can tune the angle of the BBO according to (4.1) to phase match to the signal frequency. In the schematic shown in Figure 4.5, we see that the parametric process is in a two pass configuration to maximize power. In the first pass, the delay between the pump and seed sets the central frequency of the signal, while the second pass delay ensures correct pulse timing.

4.2 Pulse width measurement and compression

The measurement of pulse width is the first step in any ultrafast experiment. This is necessary because we need to characterize the light used in the experiment and verify that the optical pulse is indeed temporally compressed to a sufficient degree. This is particularly important since the optical components we use to manipulate the beam typically broaden the pulses in time. As such, we need to not only be able to measure the pulsewidth, but also correct for the temporal expansion incurred in experimental setups.

4.2.1 Pulse width measurement

While there are a many of methods available to measure the pulse width [69], the most accessible is autocorrelation. Figure 4.8 shows the typical non-collinear intensity autocorrelation configuration. Here, we focus two input pulses of equal energy density onto a BBO crystal with matching angles of incidence. We send one of these pulses through a delay line so that it's relative delay with respect to the other pulse can be changed. When we adjust

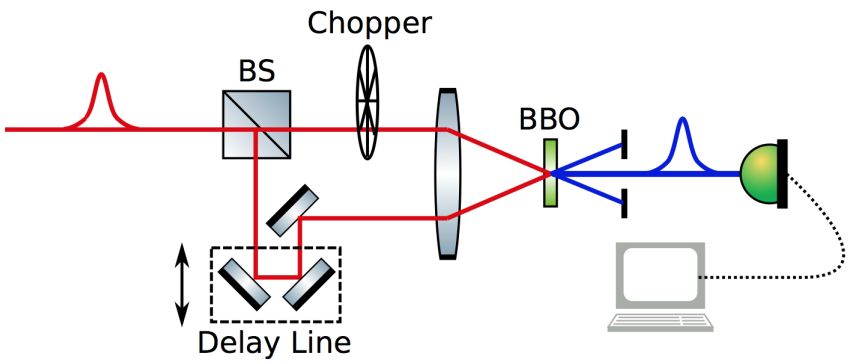

Figure 4.8: A schematic of a typical autocorrelation using a BBO crystal to measure pulse width.

the delay so that the pulses overlap in time at the BBO, a portion of the light will behave like a pulse with no net in-plane wave vector. We can adjust the crystal to phase match to the second harmonic of this beam, resulting in a frequency doubled pulse that propagates orthogonal to the plane of the crystal. We measure the intensity of the second harmonic pulse using a photodetector by scanning the delay from negative to positive values. This trace corresponds to the convolution of the input pulse intensities. Provided the two input pulses are identical and have a Gaussian profile, the temporal width of each is

$$\Delta\tau_{FWHM} = \frac{\Delta\tau^{A}_{FWHM}}{\sqrt{2}}$$

where $\Delta\tau^{A}_{FWHM}$ is the full-width-half-maximum of the the autocorrelated intensity.

This method of autocorrelation does have two down sides. First, we get no phase information, so we know nothing about the pulse chirp. Second, if the input pulses have some asymmetric temporal structure, the autocorrelation trace will still be symmetric. This means that it is very difficult to back out the real temporal profile of the input pulse from the autocorrelated intensity. If these issues are of great concern, they can be overcome by using other techniques such as frequency resolved optical gating (FROG) [70]. In my experiments, however, autocorrelation was sufficient and FROG was only necessary when re-aligning the laser components.

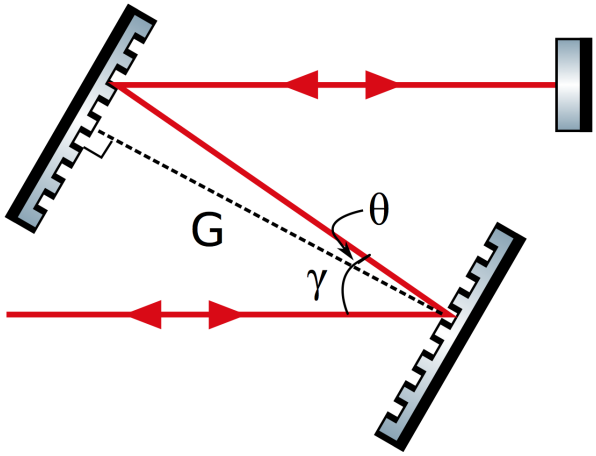

Figure 4.9: A schematic of a diffraction grating based compressor.

4.2.2 Dispersion and temporal pulse broadening

In ultrafast experiments, we typically use optical pulses < 100 fs in temporal width, and as these pulses pass through various optical elements, their pulse width changes. The reason for this has to do with the dispersive properties of materials, which causes the group velocity of light to change with frequency. This is known as group velocity dispersion (GVD), and away from resonances, most materials have positive GVD. Here, the higher frequency components of a pulse move more slowly through the material than the lower frequency components, so a chirpless or positively chirped pulse will broaden each time it passes through the material [71]. This is a major problem for ultrafast experiments where the excitation amplitude is often highly dependent on the pulse's width. We therefore need some way to balance the positive GVD in order to recompress the pulse. The two most commonly used methods are grating compressors and prism compressors. In discussing these techniques, I will refer to group delay dispersion (GDD) which is the GVD multiplied by the path length.

A grating compressor exploits the fact that spectrally dispersing a pulse can force different wavelengths to travel slightly different path lengths, thereby introducing a delay between different wavelength components. Figure 4.9 shows a schematic of a grating com-

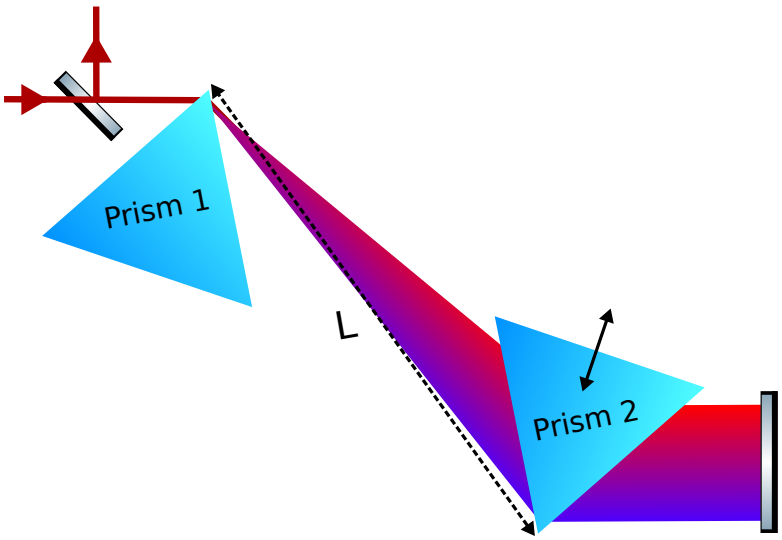

Figure 4.10: A schematic of a folded prism pair compressor.

pressor in the folded configuration. The path lengths of the redder frequencies are longer than that of bluer frequencies, and accordingly the grating compressor has negative GDD. For any given groove spacing, the separation distance G between the gratings controls the degree to which a prism compressor can compensate for positive material GDD. In general, grating can introduce large amounts of negative GDD but are lossy due to their limited diffraction efficiency. I use a grating system to stretch the pulse before injection into the RegA and then to re-compress the pulse after ejection to maximize the power of the signal from the OPA.

Another method to compensate positive GDD is through the use of prisms. Figure 4.10 shows a prism pair compressor in the folded configuration. Here there are two sources of GDD. The first is due to the angular dispersion and is negative. The second is due to the material dispersion of the prism material and is positive, but typically smaller in magnitude than that introduced through angular dispersion. When both contributions are added together, the typical prism compressor has negative GDD. The GDD can be adjusted coarsely by changing the separation length L between the prisms, or finely by translating the second prism in and out of the optical path. The utility of prism compressors lies in the

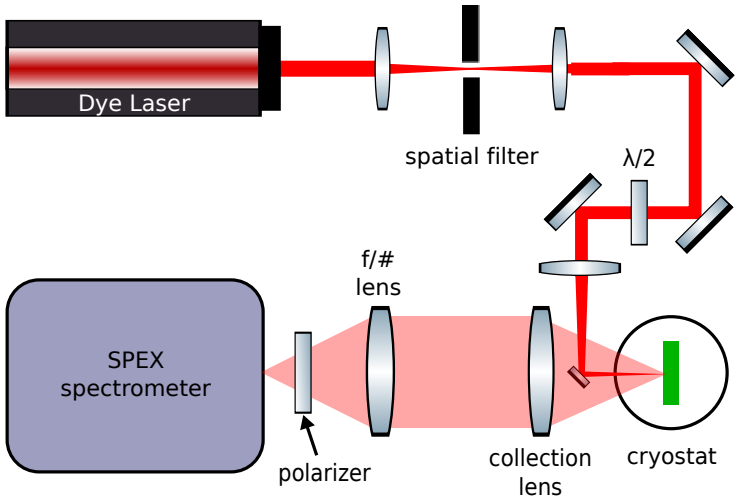

Figure 4.11: Schematic of spontaneous scattering experiment.

fact that it is virtually lossless if the prisms are cut at Brewster's angle. The MIRA uses an internal prism pair compressor for dispersion compensation. Additionally, I use two external prism compressors to minimize the pulse widths of the OPA and pick-off RegA pulses that I use in my experiments.

The preceding discussion deals exclusively with second order dispersion. There are also higher order dispersion terms that can play a role in cases where the pulse width requirements are more demanding. In these cases grating and prism compressors can be used in tandem since their third order dispersions have opposite signs. As such, with careful choices of geometry and materials, both second and third order dispersion can be simultaneously compensated.

4.3 Experimental configuration

4.3.1 Spontaneous light scattering

When dealing with opaque materials, we typically use the backscattering geometry to study the optical properties as in Figure 4.11. Here, we use a light source to photoexcite the sample, and collect the resulting scattered light along the opposite direction. The scattered

light is passed through a polarizer and then into a spectrometer with a resolution capable of resolving the features of interest. Passing the incident beam through a separate polarizer allows us to study the selection rules of the scattering process. In order to ensure accurate measurements, the scattered light must be focused through the entrance slit of the spectrometer using a lens f/# matched to the internal parabolic mirror. This can be done in one of two ways, either using a single lens for collection and focusing or two lenses dedicated to each task. The latter approach was more useful in my case since I could place the collection lens very close to the cryostat containing my sample, maximizing the amount of scattered light I was able to collect.

Since I was using a dye laser, the mode of the raw beam was, at best, elliptical. As I needed a tight focal spot on the sample, I used a spatial filter to clean the beam. Here a lens focuses the beam onto a circular pinhole placed at the focal plane. The radius of the pinhole is smaller than the beam waist. As a result of diffraction, the beam emanating from the other side has an Airy pattern, the central lobe of which is nearly-Gaussian. Thus, by passing it through an iris and re-collimating, I obtain a beam that is a good approximation of a Gaussian beam. Using this method, I was able to obtain an approximately $20\ \mu$m focal spot at the sample.

4.3.2 Pump-probe spectroscopy

Ultrafast pump-probe spectroscopy is widely used to study the time-domain dynamics of materials, and has been used to investigate a variety of fundamental excitations and systems [72, 73, 74, 75, 76, 77]. In general, the method relies upon an ultrafast pump pulse to excite the sample, and a probe pulse to measure the dynamics of the system at some time after the arrival of the pump. The experiment can be configured to measure pump-induced effects through the changes in reflectivity, transmittivity, or birefringence.

Figure 4.12(a) shows the simplest pump-probe configuration where the pump and probe originate from the same source beam, commonly referred to as a degenerate configuration.

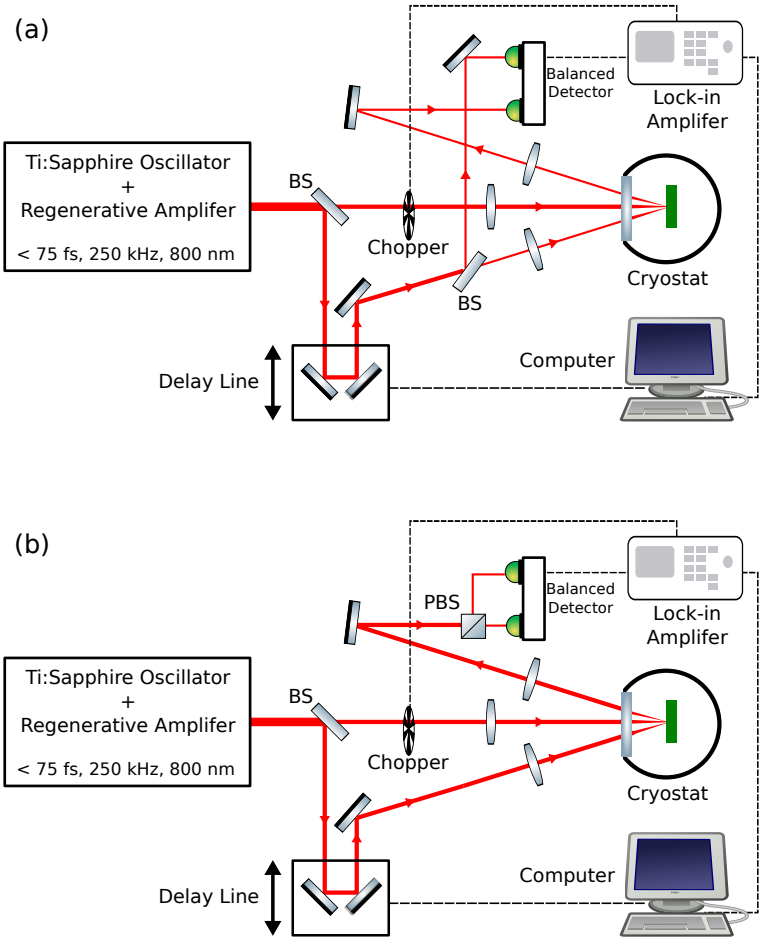

Figure 4.12: (a) The standard pump-probe scheme and (b) polarization sensitive scheme.

Here, we send the 800 nm pump pulse from the RegA through an optical chopper to modulate the beam at some frequency ω_{ref}. We send the probe beam through a mechanical delay stage, and then focus both beams onto the sample after appropriate modification of their polarizations to meet the experimental criteria. The delay stage allows us to adjust the time delay, $\Delta\tau$, between the pump and probe so that we can measure the dynamics of the system. We measure the signal in the probe using a balanced photodetector that can be used in one of two ways. In the first, we split a portion of the probe beam off before it strikes the sample, and send this beam into the first channel of the detector. The reflected probe beam is sent into the second channel and the detector outputs the difference signal. In this way we can eliminate the low frequency noise in the probe beam. We filter the signal from the detector using a 10 kHz low-pass preamplifier to eliminate the signal modulation associated with the repetition rate of the RegA and any other high frequency noise. We then use phase-sensitive detection to extract the Fourier component of the probe signal at ω_{ref}. A second detection approach, pictured in Figure 4.12(b), is to polarize the probe beam at 45° relative to the horizontal and use a polarizing beam splitter to split the vertical and horizontal components. We can then send these to the two channels of the detector. This scheme is commonly used in techniques that exploit birefringent effects induced in the material, and can sometimes be useful in isolating particularly weak signals.

In my pump-probe experiments, I modify the second method by using a double-pump probe scheme, where a second non-degenerate pump beam excites the sample at a fixed delay relative to the initial pump. The reasons for these changes are tied to the nature of my experiment and phase-sensitive detection. For this reason, I will leave the discussion of both these details to Chapter 6 when discussing my experiments involving coherent acoustic plasmons.

CHAPTER 5

Spontaneous scattering from confined acoustic plasmons

In this Chapter, I will discuss the first of two experiments designed to study acoustic plasmons in a semiconductor. The focus here will be on spontaneous light scattering experiments designed to investigate acoustic plasmons in a system in which they are confined to a layer as a set of discrete standing waves. Here, we need to consider how efficiently light couples to any given standing wave as the measured spectra will be some superposition of the contributions from each of the modes. In the first section, I will begin by describing the model used to determine the relative coupling efficiency of each mode, followed in the second section by my experimental results and analysis.

5.1 Photoelastic Model

In Chapter 2, we saw that the form of the density fluctuations associated with acoustic plasmons that have a wavevector normal to the surface are standing wave harmonics. Each mode has a discrete wavevector that is an integer multiple of the one associated with the fundamental mode. The magnitude of the fundamental wavevector is proportional to the inverse sample thickness, and as such, the spacing between adjacent modes in thin samples can be quite large. In this case, wavevector conservation in the light scattering process breaks down in the normal direction leading to scattering from "forbidden" modes [78].

In the back scattering geometry, this means that the acoustic plasmon peak is no longer strictly associated with a wavevector $q = 2k_I = 4\pi n/\lambda_I$. Instead, the spectra will be the superposition of the contribution of several modes, and we must determine the relative weight of the the contributions from each mode under an appropriate framework.

In order to determine the inelastic scattering efficiency of acoustic plasmon standing wave modes, we can exploit the analogy between acoustic plasmons and LA phonons, and employ the photoelastic model used to describe the scattering spectra of the latter in heterostructures. This approach has proven successful in describing the Raman efficiency of LA phonon scattering in semiconductor superlattices [79] and free standing membranes [80, 81].

In the photoelastic model, an incident electric field induces a polarization in a material by coupling to an acoustic strain wave. This polarization radiates an electric field which is frequency shifted from the incident field by the frequency of the strain wave. Theoretical treatments of scattering under the photoelastic model were developed by Loudon [42] for simple film on substrate structures and extended to heterostructures by He et al. [82].

5.1.1 Strain waves and polarization from acoustic plasmons

As a first step, we need to determine the form of the strain wave associated with acoustic plasmons. For LA phonons, there is a physical displacement of the lattice ions leading to an extension or contraction of the sample. The resulting strain wave is given by the derivative of the lattice displacement wave [42]. In the case of acoustic plasmons, however, we are dealing with acoustic waves of carrier density, so we need to connect oscillations in the density with oscillations in strain within the crystal. Photostriction can be used to explain this relationship. The introduction of excess charge carriers into a semiconductor leads to a change in the lattice constant of the crystal due to holes in the valence band decreasing covalent bond energy, and electrons in the conduction band increasing the bonding or anti-bonding energy. If $\Delta n\,(z,t)$ is the excess charge density at a given depth z into a sample at

time t, the corresponding strain is [83]

$$s(z,t) = \frac{\Delta n(z,t)\,(dE/dP)_T}{\beta\,(C_{11}+2C_{12})} \tag{5.1}$$

where $(dE/dP)_T$ is the pressure coefficient of the band gap at lattice temperature T, β is the material's volume compressibility coefficient, and C_{ij} are elements of the material's elasticity tensor. We see that the carrier density is directly proportion to the associated strain wave in the crystal.

We can use the photoelastic effect to link the strain wave in (5.1) to an induced polarization. Here an acoustic mode causes a modulation in the electronic susceptibility of the crystal. This allows an incident electric field to mix with the strain wave associated with the acoustic mode through the photoelastic constant, inducing a nonlinear polarization that can radiate an electromagnetic field. The polarization is [42]

$$\mathbf{P_S}(z,t) = ps(z,t)\,\mathbf{E}_i(z,t) \tag{5.2}$$

where we have assumed that the incident driving field propagates in the z-direction.

5.1.2 Driving field in multilayered structure

To determine the driving field ($\mathbf{E}_i(z,t)$) in an embedded polarizable layer, we must take into account both the sample geometry and composition. Figure 5.1 shows a schematic of the sample used in both my spontaneous light scattering and pump-probe experiments. The active layer of GaAs is cladded by AlAs layers that prevent carrier diffusion into the GaAs substrate. The $Al_{0.80}Ga_{0.20}As$ and top GaAs are lattice matching and protective cap layers, respectively. As Table 5.1 indicates, each layer has a different complex refractive index. We must therefore account for both internal reflections and absorption as the wave propagates through the heterostructure. This leads to both forward and backward propagating fields in the active GaAs layer. We can determine these using the transfer matrix formalism [84].

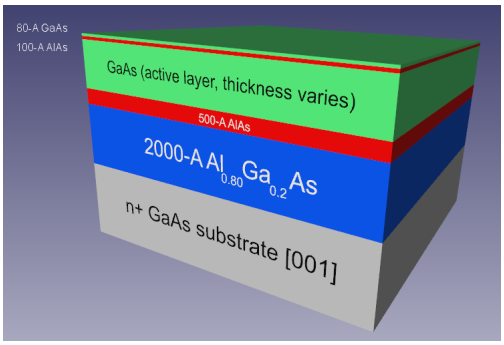

Figure 5.1: Schematic of the sample used in my experiments, grown using standard molecular beam epitaxy. The GaAs active layer thickness varies from sample to sample.

Table 5.1: Complex refractive indices of GaAs, AlAs, and $Al_{0.80}GaAs$. The † represents the value at 647 nm and the * at 800 nm.

	Refractive index ($\tilde{n}$)
GaAs	$^{\dagger}3.76 + 0.18i$
	$^{*}3.62 + 0.08i$
AlAs	$^{\dagger}3.11$
	$^{*}3.02$
$Al_{0.80}Ga_{0.20}$	$^{\dagger}3.24$
	$^{*}3.14$

Assume that the incident field is a monochromatic TE wave propagating in the positive z-direction at normal incidence. As the incident wave propagates through the material, it will encounter a different refractive index in each layer, leading to fractional reflection and transmission at each interface. Since we know the complex refractive indices of each layer, we can write the complex reflection and transmission coefficients for a normally incident TE wave as

$$r_{jk} = \frac{\tilde{n}_j - \tilde{n}_k}{n_j + n_k}, \tag{5.3}$$

$$t_{jk} = \frac{2\tilde{n}_j}{\tilde{n}_j + \tilde{n}_k}, \tag{5.4}$$

where j and k are indices that label adjacent matrices and $\tilde{n}_i$ is the complex index of layer i. Using these, we can write the interface transfer matrix that governs transmitted and

reflected amplitudes as

$$\mathbf{I}_{jk} = \frac{1}{t_{jk}} \begin{bmatrix} 1 & r_{jk} \\ r_{jk} & 1 \end{bmatrix}. \tag{5.5}$$

The interface matrix has the property $\mathbf{I}_{kj} = \mathbf{I}_{jk}^{-1}$. In addition, as the wave propagates through the structure it acquires a phase that is dependent upon the index of the layer. This propagation matrix is given by

$$\mathbf{L}_j = \begin{bmatrix} e^{-i\tilde{k}_j d_j} & 0 \\ 0 & e^{i\tilde{k}_j d_j} \end{bmatrix}, \tag{5.6}$$

where d_i is the thickness of the i^{th} layer and $\tilde{k}_i = 2\pi\tilde{n}_i/\lambda_I$ with λ_I being the vacuum wavelength of the incident field. For an m layer structure, we can relate the incident field on the input side ($i = 0$) to the field at the output side ($i = m + 1$) by successive products of the interface transfer and propagation matrices. That is,

$$\begin{aligned} \begin{bmatrix} \mathbf{E}_0^+ \\ \mathbf{E}_0^- \end{bmatrix} &= \left(\prod_{i=1}^{m} \mathbf{I}_{(i-1)i} \mathbf{L}_i \right) \mathbf{I}_{m(m+1)} \begin{bmatrix} \mathbf{E}_{\mathrm{m+1}}^+ \\ \mathbf{E}_{\mathrm{m+1}}^+ \end{bmatrix}. \\ &= \begin{bmatrix} S_{11} & S_{12} \\ S_{21} & S_{22} \end{bmatrix} \begin{bmatrix} \mathbf{E}_{\mathrm{m+1}}^+ \\ \mathbf{E}_{\mathrm{m+1}}^+ \end{bmatrix} = \mathbf{S} \begin{bmatrix} \mathbf{E}_{\mathrm{m+1}}^+ \\ \mathbf{E}_{\mathrm{m+1}}^+ \end{bmatrix}. \end{aligned} \tag{5.7}$$

Here $\mathbf{S}$ is the total transfer matrix of the structure. Using an analogous definition, we can define intermediate transfer matrices of the system that will give the forward and backward fields in a layer j:

$$\mathbf{S}_{\mathrm{j}}^{'} = \left(\prod_{i=1}^{j-1} \mathbf{I}_{(i-1)i} \mathbf{L}_i \right) \mathbf{I}_{(j-1)j} \tag{5.8}$$

$$\mathbf{S}_{\mathrm{j}}^{''} = \left(\prod_{i=j+1}^{m} \mathbf{I}_{(i-1)i} \mathbf{L}_i \right) \mathbf{I}_{m(m+1)}. \tag{5.9}$$

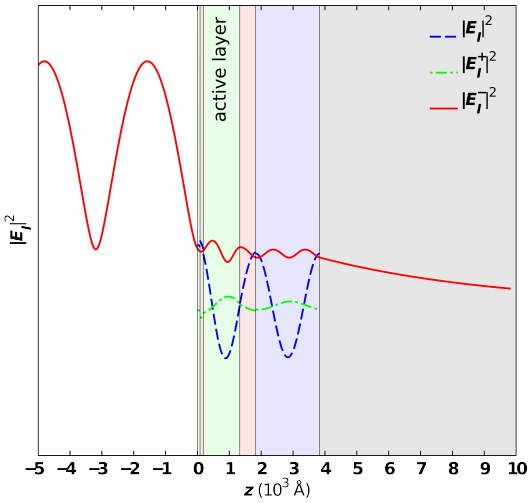

Figure 5.2: The squared incident field for the heterostructure. The shaded regions are colored to indicate the corresponding layer in Figure 5.1.

The electric field in layer j is then

$$\mathbf{E}_j(z,t) = \frac{S''_{j11}e^{-i\tilde{k}_j(d_j-z_j)} + S''_{j21}e^{i\tilde{k}_j(d_j-z_j)}}{S'_{j11}S''_{j11}e^{-i\tilde{k}_j d_j} + S'_{j12}S''_{j21}e^{i\tilde{k}_j d_j}}\mathbf{E}_0^+ \tag{5.10}$$

where $z_j = 0 \leq z \leq d_j$. Equation (5.10) is the field that can drive a polarization within layer j according to (5.2). Figure 5.2 shows the squared incident electric field in my sample.

5.1.3 Scattered field in a multilayered structure

In order to calculate the scattered field, we make use of a transfer matrix method developed by Bethune to deal with radiation from nonlinear polarization sources in embedded layers [85]. To begin, let us consider the active layer alone. For simplicity we assume that the applied electric field is polarized in the x-direction and is given by

$$\mathbf{E}_j(z,t) = \left[Ae^{ik_j z_j} + Be^{-ik_j z_j}\right] e^{-i\omega_I t}\hat{\mathbf{x}}. \tag{5.11}$$

Taking a general strain wave of the form

$$s_m(z,t) = \left[ae^{iq_m z} + be^{-iq_m z}\right] e^{-i\omega_m t},$$

we can insert Equation (5.11) into (5.2) to obtain the photoelastically induced polarization in the active layer:

$$\begin{aligned}\mathbf{P}_S(z,t) &= p\Big[aAe^{i\left(\tilde{k_j}+q_m\right)z_j} + bBe^{-i\left(\tilde{k_j}+q_m\right)z_j} \\ &\quad + bAe^{i\left(\tilde{k_j}-q_m\right)z_j} + aBe^{-i\left(\tilde{k_j}-q_m\right)z_j}\Big]\hat{\mathbf{x}}. \end{aligned} \tag{5.12}$$

The polarization will be the source term in the wave equation such that

$$\frac{\partial^2 E_S(z,t)}{\partial z^2} - \frac{\tilde{n_j}}{c^2}\frac{\partial^2 E_S(z,t)}{\partial t^2} = \frac{1}{\epsilon_0 c^2}\frac{\partial^2 P_S(z,t)}{\partial t^2}. \tag{5.13}$$

The solution to equation (5.13) is the sum of the homogenous solution and the particular (or bound) solution. For the moment let us consider the latter. With the ansatz

$$\begin{aligned}\mathbf{E}_S^B &= \Big[A' e^{i\left(\tilde{k_j}+q_m\right)z_j} + B' e^{-i\left(\tilde{k_j}+q_m\right)z_j} \\ &\quad + C' e^{i\left(\tilde{k_j}-q_m\right)z_j} + D' e^{-i\left(\tilde{k_j}-q_m\right)z_j}\Big] e^{-i(\omega_I-\omega_m)t}\hat{\mathbf{x}}, \end{aligned} \tag{5.14}$$

we can compute the derivatives on the left hand side of Equation (5.13) using (5.14) and the derivative on the right hand side using (5.12). By matching terms with the same exponential

dependence, we obtain for the coefficients

$$A' = \frac{-p\omega_s}{\epsilon_0 c^2} \frac{aA}{\tilde{k}_{sj}^2 - \left(\widetilde{k}_j + q_m\right)^2} \tag{5.15}$$

$$B' = \frac{-p\omega_s}{\epsilon_0 c^2} \frac{bB}{\tilde{k}_{sj}^2 - \left(\widetilde{k}_j + q_m\right)^2} \tag{5.16}$$

$$C' = \frac{-p\omega_s}{\epsilon_0 c^2} \frac{bA}{\tilde{k}_{sj}^2 - \left(\widetilde{k}_j - q_m\right)^2} \tag{5.17}$$

$$D' = \frac{-p\omega_s}{\epsilon_0 c^2} \frac{aB}{\tilde{k}_{sj}^2 - \left(\widetilde{k}_j - q_m\right)^2} \tag{5.18}$$

where $\omega_s = \omega_I - \omega_m$ is the Stokes frequency, $\tilde{k}_{sj} = \omega_s \tilde{n}_j / c$ is the wavevector of the Stokes free (homogenous) wave, and $\tilde{k}_j = 2\pi\tilde{n}_j/\lambda_I$ is the complex wavevector of the applied field.

We use the amplitudes of the bound wave as the source term for a free Stokes wave by introducing pseudo reflection and transmission coefficients that describe the coupling efficiency of the bound wave to the free wave [85]. This represents the phase matching requirement for efficient free wave generation. The source term is associated with two separate bound waves, one with wavevector $\tilde{K}_1 = \tilde{k}_j + q_m$ and the other with $\tilde{K}_2 = \tilde{k}_j - q_m$. For the active GaAs layer, we can construct a bound wave matrix given by

$$\begin{aligned} \mathbf{E}_{bound} &= \mathbf{E}^1_{bound} + \mathbf{E}^2_{bound} \\ &= \begin{bmatrix} A' \\ B' \end{bmatrix} + \begin{bmatrix} C' \\ D' \end{bmatrix}. \end{aligned} \tag{5.19}$$

We make the assumption that $\tilde{n}_i\left(\omega_I\right) = \tilde{n}_i\left(\omega_s\right)$ for every layer i, and define pseudo refractive indices $\tilde{n}_{s1} = c\tilde{K}_1/\omega_s$ and $\tilde{n}_{s2} = c\tilde{K}_2/\omega_s$. This allows us to describe the coupling

between the bound and free wave by a pseudo interface and propagation matrices given by

$$\mathbf{L}_{S\gamma} = \begin{bmatrix} e^{-i\widetilde{K}_\gamma D} & 0 \\ 0 & e^{i\widetilde{K}_\gamma D} \end{bmatrix} \tag{5.20}$$

and

$$\mathbf{I}_{\mathbf{S}\gamma} = \frac{1}{t_{S\gamma}} \begin{bmatrix} 1 & r_{S\gamma} \\ r_{S\gamma} & 1 \end{bmatrix}, \tag{5.21}$$

where $\gamma = 1, 2$ labels the bound source and $r_{S\gamma}$ and $t_{S\gamma}$ are the pseudo transmission and reflection coefficients found from Equations (5.3) and (5.4). If the active layer is labeled as j, we can define an effective source matrix as

$$\mathbf{F}_{j\gamma} = \left(\mathbf{L}_j \mathbf{I}_{S\gamma} \bar{\mathbf{L}}_{S\gamma} - \bar{\mathbf{L}}_{S\gamma}\right) \mathbf{E}^{\gamma}_{bound}. \tag{5.22}$$

Finally, we compute the scattered free wave amplitude at the input and output interfaces as

$$\begin{bmatrix} E^{+}_{S\gamma,j+1} \\ E^{-}_{S\gamma,0} \end{bmatrix} = \frac{1}{S_{11}} \begin{bmatrix} 1 & 0 \\ S_{21} & -S_{11} \end{bmatrix} \mathbf{F}^{'}_{j\gamma}, \tag{5.23}$$

where $\mathbf{F}^{'}_{j\gamma} = \mathbf{S}^{'}_{j}\mathbf{F}_{j\gamma}$, and S_{ij} and $\mathbf{S}^{'}_{j}$ are given by (5.7) and (5.8), respectively. The scattered wave at the output propagates in the forward direction and the wave at the input side propagates in the backward direction. To complete the treatment of the scattered free waves, we add the contributions due to each bound source.

It is also useful to know the field distribution within the layered structure in addition to the waves retreating from the input and output surfaces. In order to do this, we can use the formalism developed by Hashizume et al. [86] based on a method proposed by Sipe [87]. The treatment can be used as a standalone procedure, but here I incorporate the previous results. For a normally incident driving field polarized in the x-direction, the

Green's function associated with a 2D polarization sheet in the xy plane in layer j is [86]

$$\begin{aligned}\mathbf{G}\left(z,z'\right) &= i\frac{\omega_s^2}{2\epsilon_0 c^2\widetilde{k}_{sj}}\hat{x}\hat{x}e^{i\widetilde{k}_{sj}(z-z')}\theta\left(z-z'\right) \\ &\quad +i\frac{\omega_s^2}{2\epsilon_0 c^2\widetilde{k}_{sj}}\hat{x}\hat{x}e^{-i\widetilde{k}_{sj}(z-z')}\theta\left(z-z'\right) \\ &\quad \times\theta\left(z'-z\right)-\frac{1}{\epsilon_j}\hat{z}\hat{z}\delta\left(z-z'\right).\end{aligned}$$

This allows us to construct the scattered field from an arbitrary polarization as

$$\mathbf{E}_S\left(z\right)=\int_{-\infty}^{\infty}\mathbf{G}\left(z-z'\right)\mathbf{P}_{NL}\left(z'\right)dz',$$

and specifically, we can describe the field in layer j that would exist if the entire structure was comprised of the same material (i.e. no internal reflections). This is referred to as $\mathbf{E}_j^{self}\left(z\right)$ and is given by

$$\mathbf{E}_j^{self}\left(z\right) = \mathbf{E}_j^r\left(z\right)+\mathbf{E}_j^b\left(z\right)$$

where

$$\begin{aligned}\mathbf{E}_j^r\left(z\right) &= i\frac{\omega_s^2}{2\epsilon_0 c^2\widetilde{k}_{sj}}\hat{x}\hat{x}\cdot\int_{z_{j-1}}^{z}\mathbf{P}_{NL,j}\left(z'\right)e^{-i\widetilde{k}_{sj}z'}dz'e^{i\widetilde{k}_{sj}z} \\ &\quad +i\frac{\omega_s^2}{2\epsilon_0 c^2\widetilde{k}_{sj}}\hat{x}\hat{x}\int_{z}^{z_j}\mathbf{P}_{NL,j}\left(z'\right)e^{i\widetilde{k}_{sj}z'}dz'e^{-i\widetilde{k}_{sj}z} \qquad (5.24)\\ \mathbf{E}_j^b\left(z\right) &= -\frac{1}{\epsilon_j}\hat{z}\hat{z}\cdot\mathbf{P}_{NL,j}\left(z\right). \qquad (5.25)\end{aligned}$$

The first and second terms of Equation (5.24) represents the forward and backward waves from the nonlinear polarization behind and ahead of the point z, respectively. Equation (5.25) gives the field that is bound to the nonlinear polarization.

Having defined the self-field, we can find the additional field profile that would be

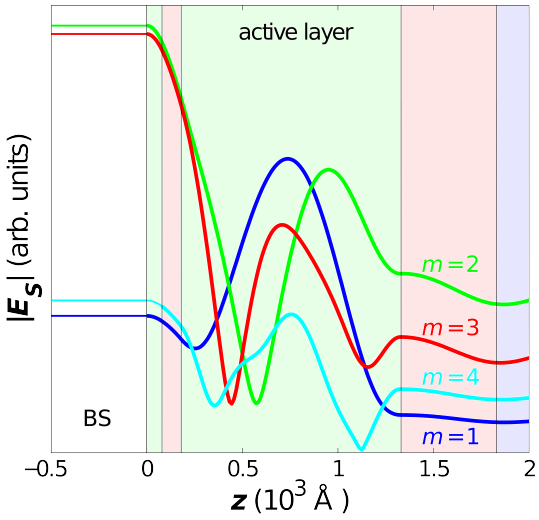

Figure 5.3: A sample of the scattered field inside the heterostructure. The shaded regions are colored to indicate the corresponding layer in Figure 5.1.

present in any layer as a result of generation in the nonlinear layer(s) and subsequent transmission and reflection at the various interfaces in the structure. Namely, [86]

$$\begin{bmatrix} E_j^{add,+}(z) \\ E_j^{add,-}(z) \end{bmatrix} = \mathbf{L}_j^{-1}(z - z_{j-1}) \left\{ \mathbf{S}_i'^{-1} \begin{bmatrix} 0 \\ E_{S\gamma,0}^{-} \end{bmatrix} + \mathbf{S}_i'^{-1} \begin{bmatrix} E_0^{r,+}(0) \\ E_0^{r,-}(0) \end{bmatrix} - \begin{bmatrix} E_j^{r,+}(z_j) \\ E_j^{r,-}(z_j) \end{bmatrix} + \sum_{\beta=1}^{j-1} \mathbf{S}_j'^{-1} \mathbf{S}_\beta' \mathbf{L}_\beta \mathbf{L}_j \mathbf{F}_j \right\},$$

where the first term on the right hand side is determined from Equation (5.23). The total field in any layer j is then given by $\mathbf{E}_j(z) = \mathbf{E}_j^{add}(z) + \mathbf{E}_j^{self}(z)$.

Figure 5.3 shows a sample of the scattered field computed using the method outlined above. The magnitude of the fields on the first surface show that certain modes couple more efficiently to the incident field than others. In my analysis, I used the relative field magnitudes to construct a set of weighting factors which I used to perform a weighted sum of the theoretically computed spectra for a set of acoustic plasmon standing wave modes.

5.2 Experimental results and analysis

My experiments were focused upon three samples with GaAs active layer thicknesses of 6000 Å, 3000 Å, and 1150 Å (all other aspects of the samples were identical, see Figure 5.1). The experimental light-scattering setup used in these experiments was discussed in Chapter 4.

5.2.1 Analysis procedure

For each sample, I took measurements at various different incident laser powers and focal spot sizes in order to measure the sample at different photoexcited EHP densities. For each experiment, I collected the anti-Stokes and Stokes depolarized spectrum ($\hat{\epsilon}_I \perp \hat{\epsilon}_S$) to measure the spin density fluctuation and $E_0 + \Delta_0$ photoluminescence line shapes. Then, I collected the anti-Stokes and Stokes polarized spectrum ($\hat{\epsilon}_I \parallel \hat{\epsilon}_S$) in order to measure the L_-, L_+, and acoustic plasmon spectral peaks. The polarized spectrum also included a signal associated with the $E_0 + \Delta_0$ photoluminescence and a polarized component of the SPE. After fitting the photoluminescence in the depolarized spectrum with two Gaussians, one for each side of the peak, I subtracted this estimate from the depolarized spectrum to obtain the line shape of the SDFs. I divided the resulting SDF line by Bose factors ($n(\omega) + 1$ for the Stokes side and $n(\omega)$ for the anti-Stokes side) at various temperatures until the Stokes and anti-Stokes sides were mirror images of each other. The temperature which satisfied this condition was the temperature of the carriers (T).

Using the carrier temperature, I calculated the theoretical structure factor at various carrier densities and dampings using Equation (3.44). By comparing the calculated L_- and L_+ peak positions with the corresponding experimental peaks, I was able to assign an initial guess of the carrier density (n) and plasma damping (Γ) for each experiment. I then compared theoretical SDF and measured spectra, adjusting the plasma damping term as necessary to improve the fits. Finally, I recalculated the theoretical polarized spectra using

n, T, and the updated Γ. By iterating over this process several times, I was able to obtain consistent fits of both the SPE spectra and L_- and L_+ peak positions.

Once I had established the n, T, and Γ for the plasma, I was able calculate the associated slope of the acoustic plasmon frequency dispersion. Using this slope, the thickness of the sample, and the associated set of mode wavevectors, $q_m = m\pi/d_{active}$, I calculated the scattering efficiency of each mode under the photoelastic model and obtained weighting factors for the scattering contributions of several adjacent modes (10 to 20 modes depending on the thickness of the sample). After calculating the acoustic plasmon spectra for each of the modes, I computed the theoretical acoustic plasmon spectral peak as a weighted sum of the contributions of each mode as

$$I_S(\omega) \propto \sum_{j=1}^{N_m} q_j^2 w_j \Im\{S(\mathbf{q}_j, \omega)\},$$

where N_m was the number of modes used in the sum, w_j is the weighting factor associated with mode j, and S is given by Equation (3.44). I will now discuss the comparison of these calculations to the experimental data for each of the three samples.

5.2.2 6000 Å sample

For the 6000 Å sample, I was able to photoexcite 4 different carrier densities by changing the power of the incident laser beam. In Figure 5.4, I have plotted the experimental SPE spectra and theoretical predictions for the four densities. The insets of each figure show the raw depolarized spectrum and a dashed line representing the estimated photoluminescence. I have noted the three plasma parameters in the figures, and the red line is the corresponding theoretical SDF lineshape. The deviation between the calculated and experimental SDF spectra become more pronounced at lower carrier densities and is due to errors in the photoluminescence estimates, as they are less accurate due to decreased signal at lower densities. However, in general, the fits are consistent with the experimental data,

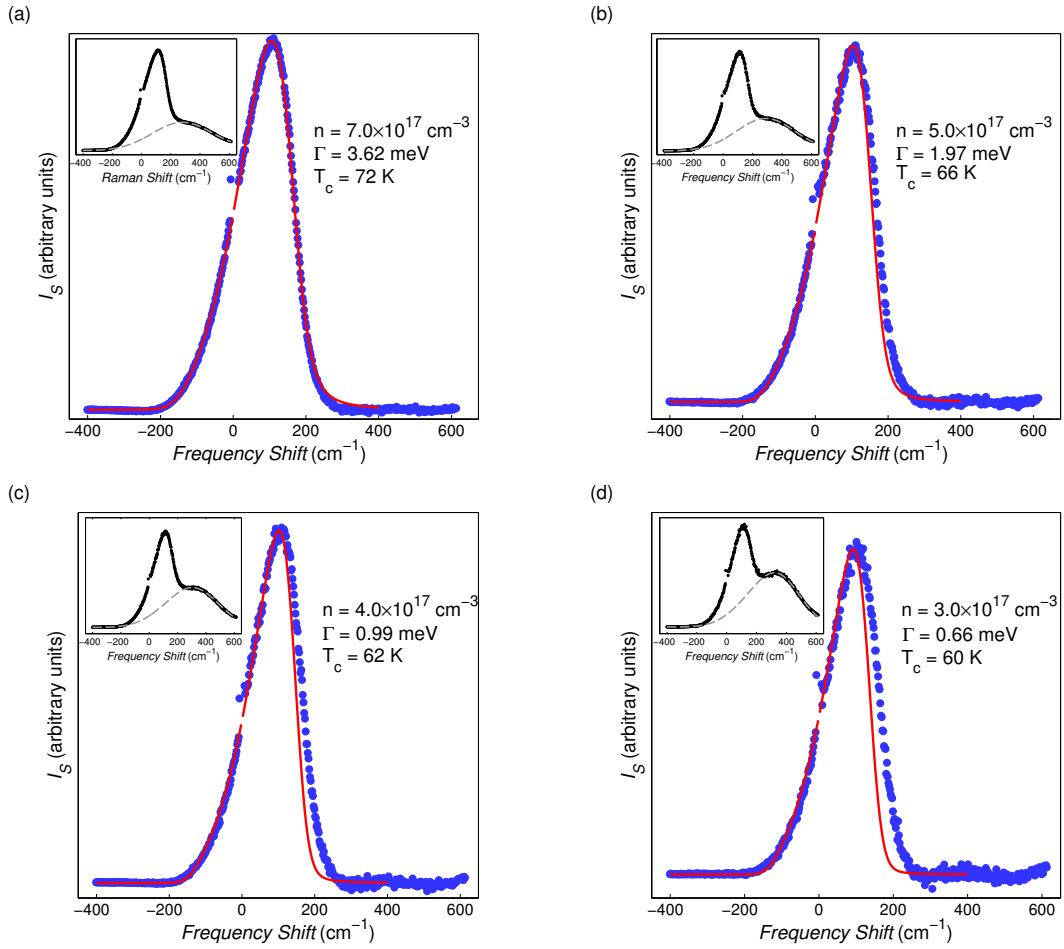

Figure 5.4: The experimentally obtained spin density fluctuation spectrum for (a) $n = 7.0 \times 10^{17}$ cm^{-3}, (b) $n = 5.0 \times 10^{17}$ cm^{-3}, (c) $n = 4.0 \times 10^{17}$ cm^{-3}, and (d) $n = 3.0 \times 10^{17}$ cm^{-3}. The red lines are the calculated SDF spectra for the plasma parameters indicated in the figures. The insets of each figure show the raw depolarized spectrum (in black) and the photoluminescence estimate (in gray).

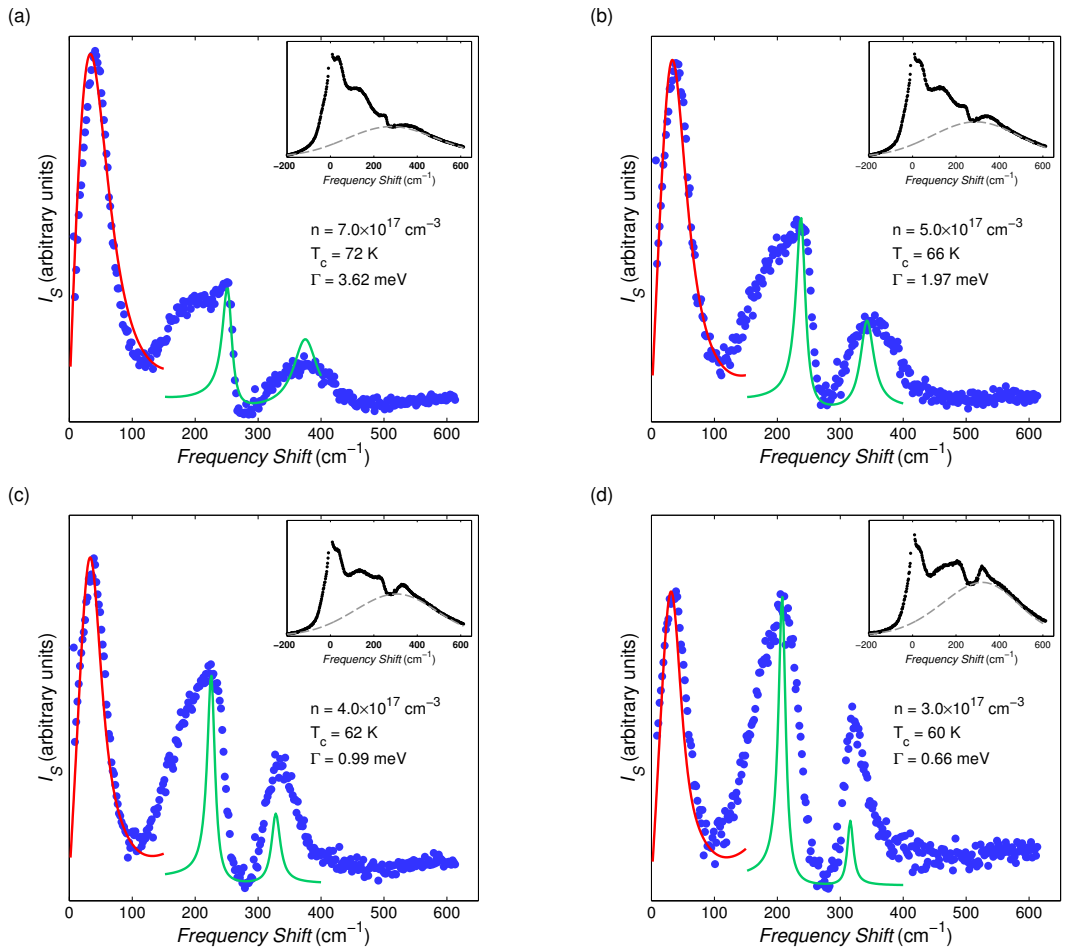

Figure 5.5: The experimentally obtained polarized spectrum for the 6000-Å sample for (a) $n = 7.0 \times 10^{17}$ cm^{-3}, (b) $n = 5.0 \times 10^{17}$ cm^{-3}, (c) $n = 4.0 \times 10^{17}$ cm^{-3}, and (d) $n = 3.0 \times 10^{17}$ cm^{-3}. The blue dots are the experimental spectrum after subtraction of the luminescence and polarized SPE component, and division by the Bose factor. The calculated electronic contributions to the polarized spectra for the coupled modes are shown in green. The theoretical photoelastically weighted spectra for acoustic plasmons is shown in red. The insets of each figure show the raw polarized spectrum (in black) and the photoluminescence fit (in gray).

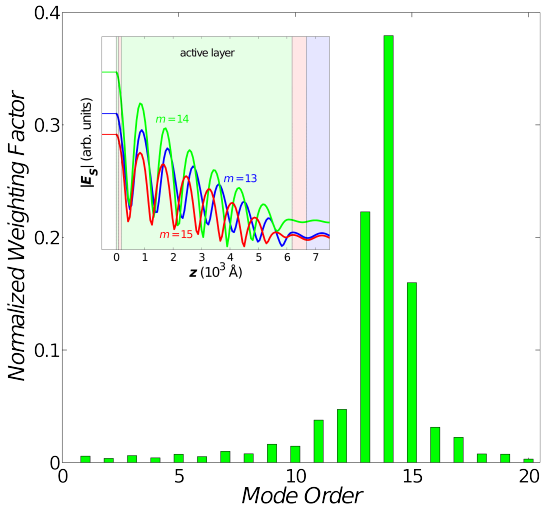

Figure 5.6: Normalized weighting factors for modes 1 though 20 for $n = 7 \times 10^{17}$ cm^{-3}. The inset shows the absolute value of the scattered fields for modes 13-15 inside the GaAs active layer.

particularly on the anti-Stokes side where the luminescence is smaller, and for higher densities where the overall signal to noise is higher. As expected, both the carrier temperature and plasma damping decrease as the incident laser power is diminished, and are well within range of values in the literature [50, 19].

In Figure 5.5, I have plotted the polarized spectrum for the four densities. The insets show the raw polarized spectra and estimates of the photoluminescence. The calculated electronic contribution to the scattering cross section for the coupled modes appear in green. In general, they show excellent agreement between the experimental peak positions of the L_- and L_+ modes, but the line widths and relative peak heights do not match. In the case of the L_- mode, the pronounced asymmetry in the experimental peak is due to the variation in carrier density across the focal spot of the beam. This has the effect of smearing the spectral peak to the low frequency side due to the strong variation of the L_- mode's frequency with carrier density (see Figure 3.6). The L_+ peak does not show this asymmetry because its frequency does not vary greatly at low densities. I attribute the difference in relative peak heights between theory and experiment to the fact that I am only plotting the

carrier contribution to the scattering cross section, and ignoring the contribution from the phonon component of of the coupled modes due to the deformation scattering mechanism [2]. Additionally the larger widths of the experimental peaks may be due, in part, to the effect of damping mechanisms not considered in the theoretical calculations. A full line shape analysis of the coupled modes is further complicated by the resonant behavior of the electro-optic tensor which affects the phonon-component of the scattering cross section [2]. This is beyond the scope of this work as I am primarily interested in the peak positions as a metric to make the carrier density assignment.

Figure 5.6 shows one set of normalized weighting factors for the $n = 7 \times 10^{17}$ cm^{-3} case. The efficiency is highly dependent on mode order, with the 14^{th} mode showing the strongest coupling. This is expected as the $m = 14$ mode has a wavevector of $q = 14\pi/d = 7.33 \times 10^5$ cm^{-1}, which is extremely close to the backscattering wavevector of the incident light ($q_{BS} = 4\pi n/\lambda_{incident} = 7.30 \times 10^5$ cm^{-1}). Accordingly this mode leads to a strain wave that has the best phase matching to the incident field. Additionally, due to the relatively small wavevector spacing between adjacent modes, the distribution of weighting factors is fairly symmetric about the dominant mode. The weighting factors for the other carrier densities show a similar trend with only slight differences in the magnitude. In the inset, I have plotted the absolute value of the scattered field of the 3 highest efficiency modes ($m = 13, 14, 15$). The red line in Figure 5.5 represents the calculated weighted sum spectra of the acoustic plasmon given the weighting factors in Figure 5.6. For all the densities, the photoelastic weighting of the first 20 modes consistently reproduces both the peak location and line shape of the acoustic plasmon. This reenforces the validity of both standing wave discretization of the acoustic plasmon and the assumption of photoelastic efficiency.

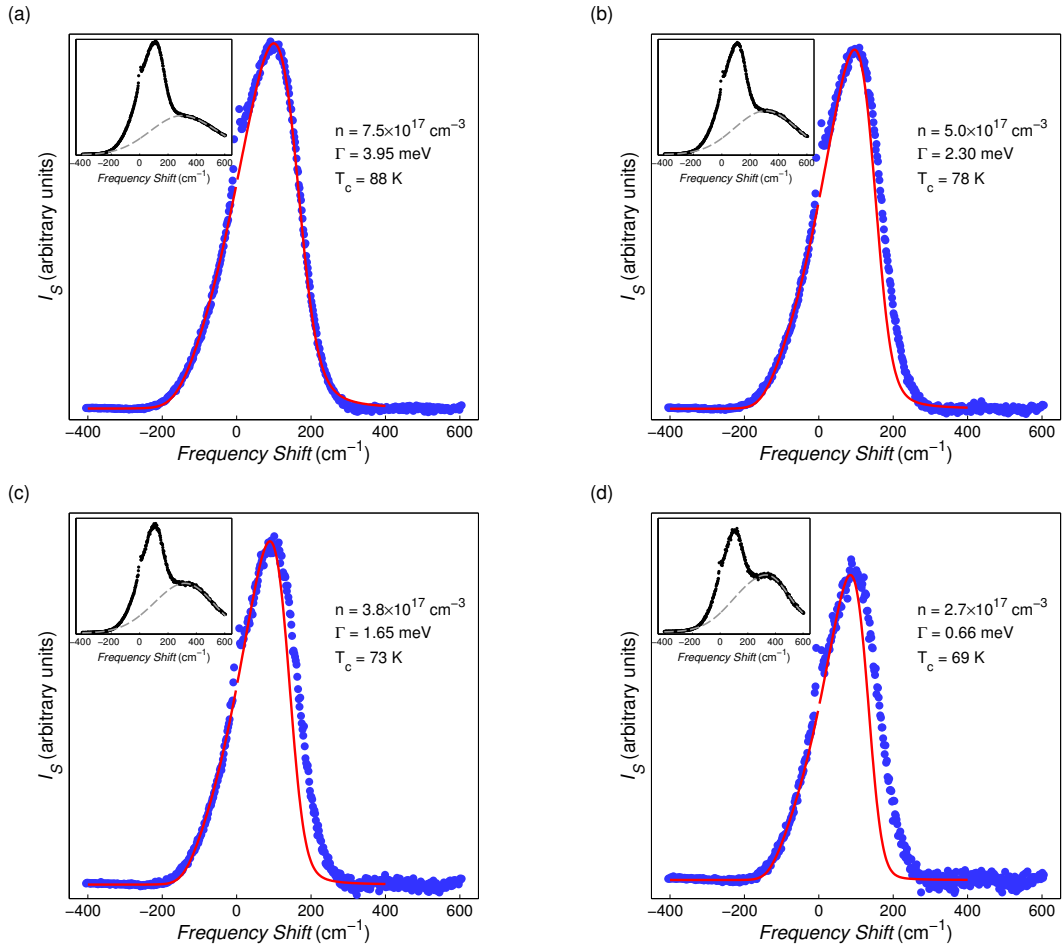

Figure 5.7: The experimentally obtained spin density fluctuation spectrum for the 3000 Å sample at (a) $n = 7.5 \times 10^{17}$ cm^{-3}, (b) $n = 5.0 \times 10^{17}$ cm^{-3}, (c) $n = 3.8 \times 10^{17}$ cm^{-3}, (d) $n = 2.7 \times 10^{17}$ cm^{-3}. The red line is the calculated SDF line shape for the plasma parameters indicated in the figure. The insets of each figure show the raw depolarized spectrum (in black) and the photoluminescence estimate (in gray).

5.2.3 3000 Å sample

I performed experiments with the 3000 Å sample in the same way as for the 6000 Å sample. Figure 5.7 shows the corresponding experimental and theoretical SDF spectra. As in the previous case, the fits show excellent agreement for high densities but tend to deviate on the low energy side at lower densities. Figure 5.8 shows the experimental polarized spectra and the theoretical coupled mode spectra (green line). Again, we see that the plasma parameter estimates produce consistent predictions for both the coupled mode positions and SDF line

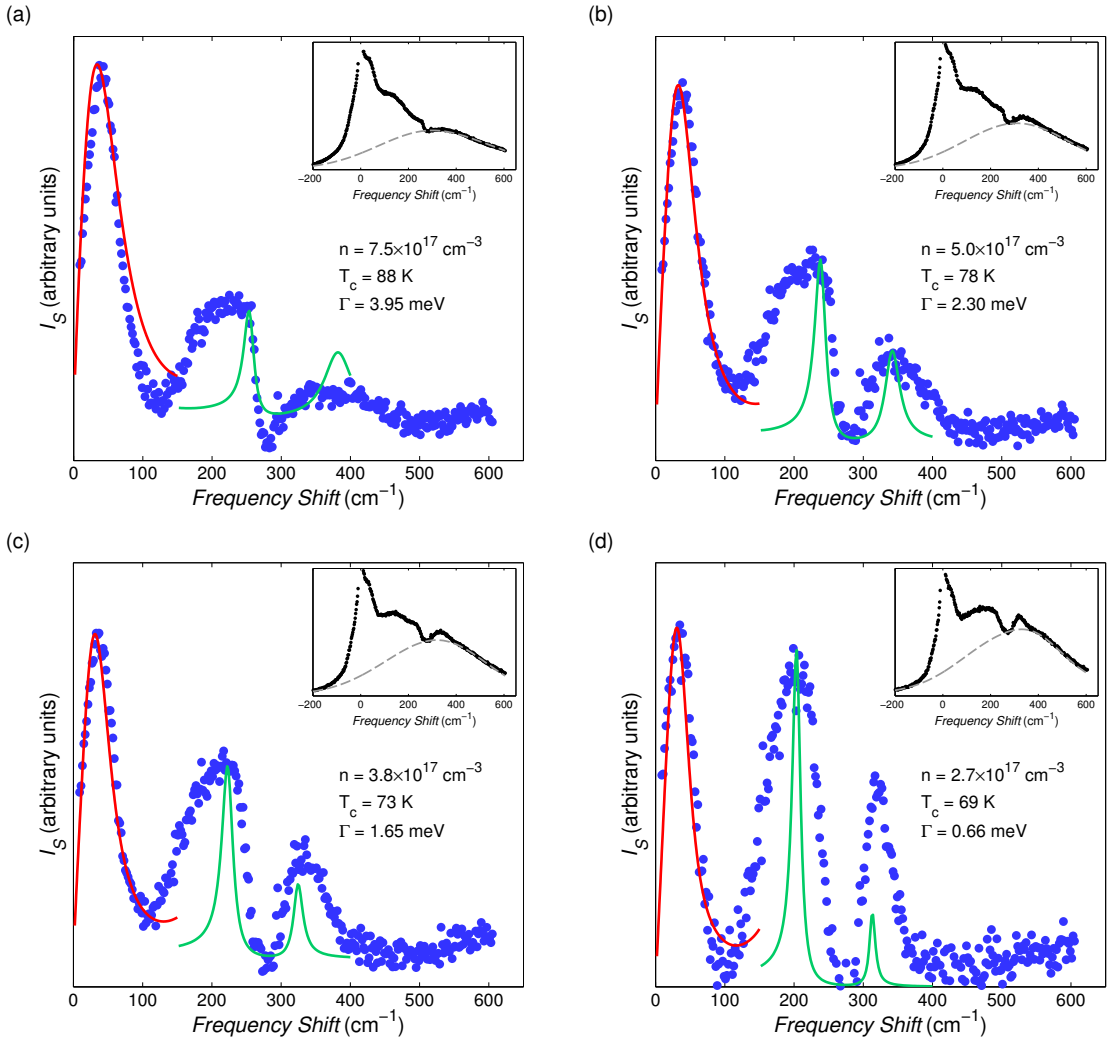

Figure 5.8: The experimentally obtained polarized spectrum for the 3000 Å sample at (a) $n = 7.5 \times 10^{17}$ cm^{-3}, (b) $n = 5.0 \times 10^{17}$ cm^{-3}, (c) $n = 3.8 \times 10^{17}$ cm^{-3}, (d) $n = 2.7 \times 10^{17}$ cm^{-3}. The blue dots are the experimental spectrum after subtraction of the luminescence and polarized SPE component, and division by the Bose factor. The calculated electronic contributions to the polarized spectra for the coupled modes are shown in green. The theoretical photoelastically weighted spectra for acoustic plasmons is shown in red. The insets of each figure show the raw polarized spectrum (in black) and the photoluminescence fit (in gray).

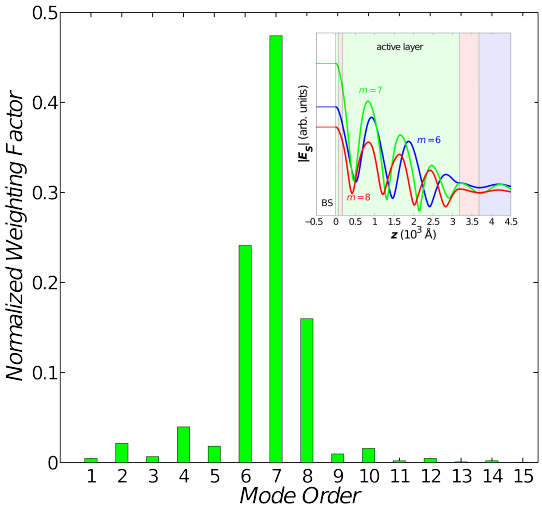

Figure 5.9: The weighting factors calculated using the photoelastic model for the 3000 Å sample for $n = 7.5 \times 10^{17}$ cm^{-3}.

shapes.

The 3000 Å sample has a set of wavevectors where the spacing between adjacent acoustic plasmon modes is twice that of the 6000 Å sample. Accordingly, we would expect that fewer modes should couple to light since there are fewer modes that are close to the back scattering wavevector of the incident light field. In Figure 5.9, we see that the coupling efficiency drops to negligible levels within 15 modes. However, the dominant $m = 7$ mode shares the same wavevector ($q = 7.33 \times 10^5$ cm^{-1}) as the dominant mode in the 6000 Å sample. Moreover, the coupling distribution is relatively symmetric about the dominant mode, indicating that the acoustic plasmon peak in these two samples should be at approximately the same frequency. Figure 5.8 shows the theoretical weighted acoustic plasmon spectra (red line) expected for the 3000 Å sample for the various densities . As with the 6000 Å sample, we see that the weighted spectra reproduces the acoustic plasmon peak position and lineshape. Moreover, the acoustic plasmon peak positions are roughly equivalent to those of the 6000 Å sample for comparable plasma densities.

5.2.4 1150 Å sample

The 1150 Å sample posed a new experimental challenge. Because it was much thinner than the other samples, even when using low laser powers, the photoexcited carrier density was always high ($> 6 \times 10^{17}$ cm^{-3}) when the beam was focused onto the sample. As such, it was difficult to probe a wide range of carrier densities by merely attenuating the laser beam. Moreover, at low laser powers, the signal to noise ratio was very low due to the smaller scattering volume relative to the two other samples. In order to overcome both these issues, I defocused the spot size which allowed me to achieve low carrier densities while still maintaining a strong scattered light signal.

The results for the 1150 Å sample show much the same results as I have previously described. There are, however, a few notable differences. In the spectra plotted in Figure 5.10, we see that the SDFs are shifted closer to the laser line. As a result, the peak appears as a shoulder. This is primarily due to the interplay between the higher carrier dampings and temperatures in the 1150 Å sample for comparable densities relative to the 6000 Å and 3000 Å samples. Additionally, in the polarized spectra shown in Figure 5.11, we see that that the coupled mode peaks are very weak in comparison to the other samples. In fact, at higher densities, the L_+ mode is damped to such an extent that it is almost indiscernible, and it was no longer a reliable metric for assigning the carrier density. As such, the carrier density assignments for the 1150 Å sample are slightly less accurate as I had to rely upon the L_- position and SDF line alone.

Based on the trend, we would expect that still fewer modes would couple to the incident light field. From Figure 5.12, we see that this is in fact the case as the coupling efficiency drops to negligible values within 10 modes, with the $m = 2$ ($q = 5.46 \times 10^5$ cm^{-1}) and $m = 3$ ($q = 8.20 \times 10^5$ cm^{-1}) modes showing the highest weighting. This is reasonable as the back scattering wavevector is positioned in between these two modes. It is interesting, however, that the second mode shows a slightly stronger coupling despite the fact that it is farther away from the back scattering wavevector than the third mode. Again, as with the

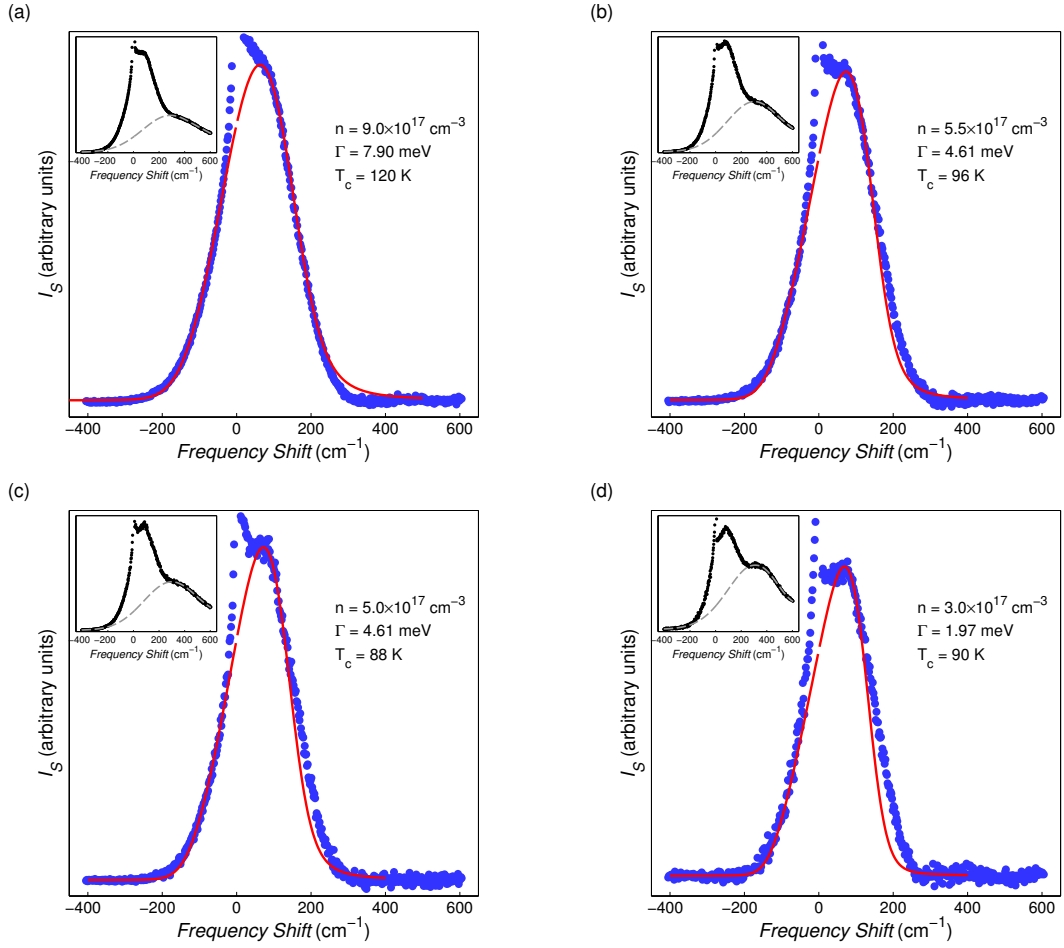

Figure 5.10: The experimentally obtained spin density fluctuation spectrum for the 1150 Å sample at (a) $n = 9.0 \times 10^{17}$ cm^{-3}, (b) $n = 5.5 \times 10^{17}$ cm^{-3}, (c) $n = 5.0 \times 10^{17}$ cm^{-3}, (d) $n = 3.0 \times 10^{17}$ cm^{-3}, and (e) $n = 2.3 \times 10^{17}$ cm^{-3}. The red line is the best calculated SPE line shape for the plasma parameters indicated in the figure. The insets of each figure show the raw depolarized spectrum (in gray) and the photoluminescence estimate (in green). The fit of the SPE spectrum is excellent at 150 mW but deviates as the power is decreased. This is likely due to errors in the photoluminescence estimates at lower powers.

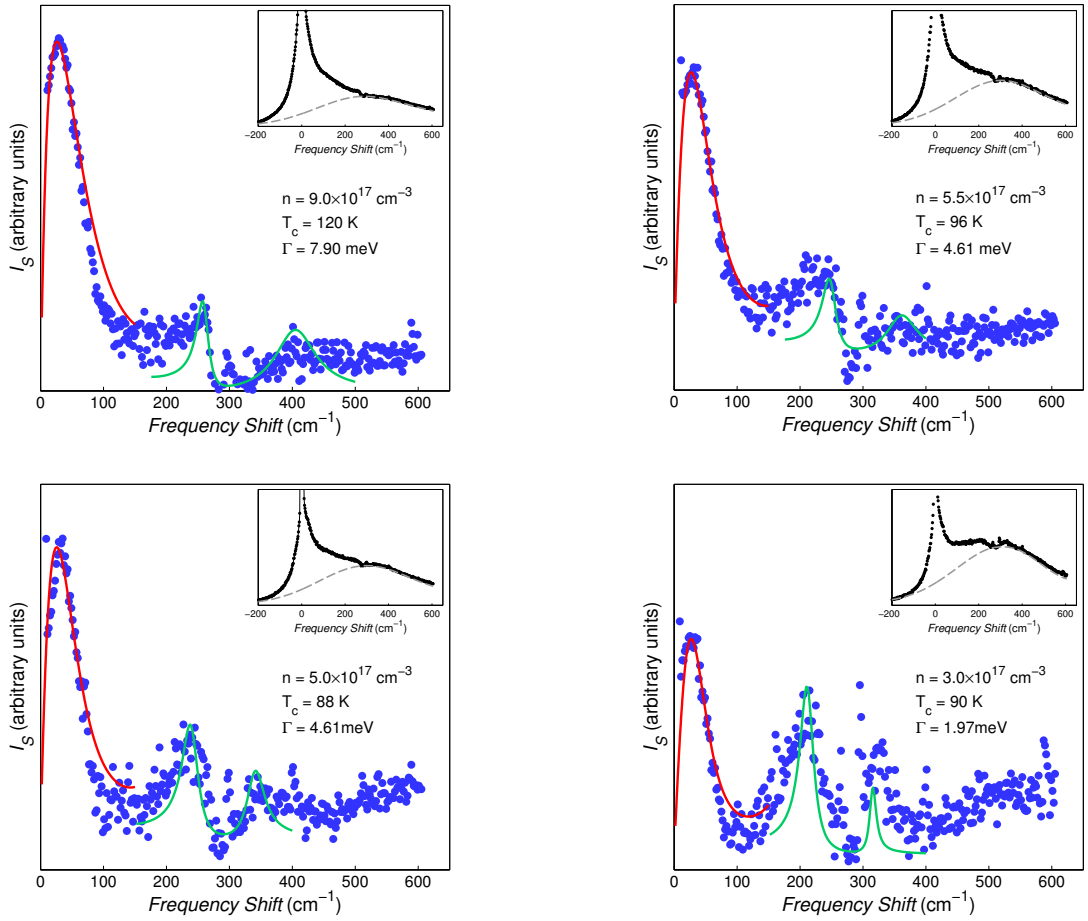

Figure 5.11: The experimentally obtained polarized spectrum for the 1150 Å sample at (a) $n = 9.0 \times 10^{17}\,\mathrm{cm}^{-3}$, (b) $n = 5.5 \times 10^{17}\,\mathrm{cm}^{-3}$, (c) $n = 5.0 \times 10^{17}\,\mathrm{cm}^{-3}$, (d) $n = 3.0 \times 10^{17}\,\mathrm{cm}^{-3}$. The blue dots are the experimental spectrum after subtraction of the luminescence and polarized SPE component, and division by the Bose factor. The calculated electronic contributions to the polarized spectra for the coupled modes are shown in green. The theoretical photoelastically weighted spectra for acoustic plasmons is shown in red. The insets of each figure show the raw polarized spectrum (in black) and the photoluminescence fit (in gray).

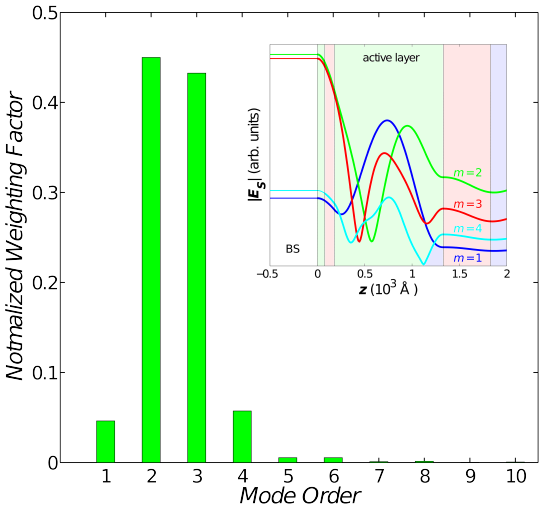

Figure 5.12: The weighting factors calculated using the photoelastic model for the 1150 Å sample for $n = 9.0 \times 10^{17}$ cm^{-3}.

other samples, we see that the calculated weighted acoustic plasmon spectra (red line) in Figure 5.11 shows excellent agreement with experiments for all the densities.

As further confirmation of the thickness dependence of the acoustic plasmon frequency, we can see from Figure 5.13 that the 1150 Å sample exhibits a markedly different acoustic plasmon frequency compared to the 6000 Å and 3000 Å samples for comparable carrier densities. This is due to the fact that in the 1150 Å sample, the phase matching condition with the incident field is not satisfied as well as for the other two samples. In both the 6000 Å and 3000 Å samples, the dominant mode has a wavevector of $q = q_D = 7.33 \times 10^5$ cm^{-1}, and is associated with some frequency ω_D dependent on the plasma parameters. In the 1150 Å sample, the $m = 2$ mode is separated from q_D by 1.83×10^5 cm^{-1}, while the $m = 3$ mode is separated by 8.93×10^4 cm^{-1}. The linearity of the acoustic plasmon's dispersion means that the $m = 2$ mode is also more than twice as far away in frequency from ω_D than the $m = 3$ mode. As a result, the net effect is that the experimental acoustic plasmon peak locations of the 1150 Å sample are downshifted relative to the 6000 Å and 3000 Å samples for comparable plasma densities.

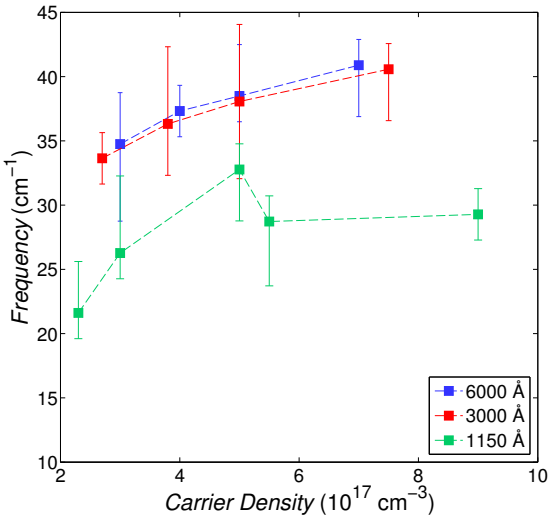

Figure 5.13: The acoustic plasmon frequency as a function of photoexcited carrier density for the 1150 Å, 3000 Å, and 6000 Å samples.

5.2.5 A remark on the connection to LA phonons

In the preceding analysis, I have relied heavily upon the photoelastic model to support my assertion that the acoustic plasmon must exist as a discrete set of standing waves. In doing so, I have leveraged the analogy between light scattering from acoustic plasmons and LA phonons. There is, however, an issue associated with this comparison. If we look at the scattering spectra from LA phonons confined to a membrane as in Figure 5.14(a), we see several discrete peaks associated with the scattering from individual modes. This forces us to ask why we do not see discrete peaks in the case of acoustic plasmons. Moreover, as I show in Figure 5.14(b), the acoustic plasmon has a much larger group velocity than LA phonons over the range of accessible wavevectors. Ostensibly, it would seem as though we should see separate peaks due to scattering from each acoustic plasmon mode. This is clearly not the case in my experimental results, but the absence of several discrete acoustic plasmon peaks in a given experiment can be explained by considering the nature of the excitation.

In chapter 2, I plotted the acoustic plasmon's dispersion in Figure 2.3, and we saw that it was embedded within the single particle excitation continuum over virtually the entire

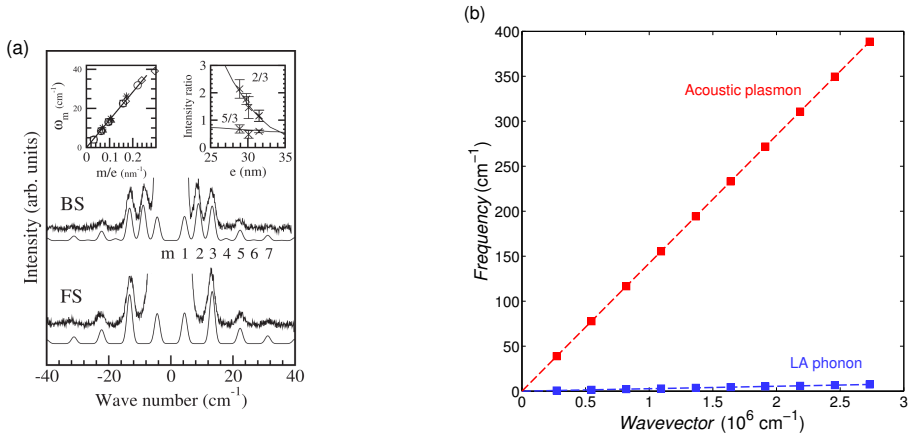

Figure 5.14: (a) The scattering cross section for LA phonons in a 30 nm Si membrane (reproduced from [80]). (b) The theoretical dispersion for confined LA phonons and acoustic plasmons confined to a 1150 Å membrane. The LA phonon dispersion was obtained from Strauch and Dorner [88].

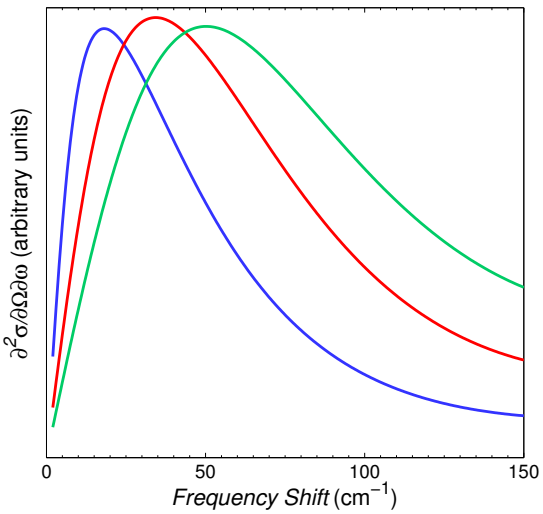

Figure 5.15: The theoretically calculated scattering cross section for the $m = 1$ (blue), $m = 2$ (red), and $m = 3$ (green) acoustic plasmon modes for the 1150 Å sample at $n = 9.0 \times 10^{17}$ cm^{-3}, $T = 120$ K, and $\Gamma = 7.90$ meV.

range of wavevectors accessible to us in light scattering experiments. This means that the acoustic plasmon is highly Landau damped through its coupling to the continua of single particle excitations of both electrons and holes. Spectrally, this manifests as a scattering peak width that is exceptionally large. As I show in Figure 5.15 for the 1150 Å sample, the FWHM can be more than a hundred cm^{-1} for the relevant modes. In contrast the LA phonons typically have widths on the order a few wave numbers as we can see in Figure 5.14(a). This is the reason why we do not see a multiple peaks, since the scattering peaks from the individual acoustic plasmon modes are severely overlapped.

5.2.6 Conclusions

Using spontaneous light scattering experiments, I am able to generate photoexcited electron-hole plasmas the show not only the coupled mode excitations associated with the interaction of optical plasmons and LO phonons, but also acoustic plasmons that originate from multi-component effects. The underlying assumption has been that, given the geometry of my samples, the acoustic plasmon should be confined to the active GaAs layer in my heterostructure. As a result of this confinement and the assumption that the carrier density fluctuation is small, the acoustic plasmon should exist as a discrete set of standing wave modes whose wavevector is dependent upon the thickness of the layer.

Through three samples, each with a different GaAs active layer thickness, we see that using the assumption of discrete standing wave modes that couple to light differently under the photoelastic model leads to a calculated weighted sum spectra that is remarkably good at reproducing not only the experimental acoustic plasmon peak location, but also the spectral line shape for a variety of plasma parameters. This then, supports the conclusions of confinement of the acoustic plasmon into a discrete set of standing waves as well as the analogy between acoustic plasmons and LA phonons. Additionally, the marked difference in acoustic plasmon frequency in the 1150 Å sample relative to the others indicates a thickness dependence in the plasmon frequency that could no exist in the absence of standing

wave modes. Future experiments should focus on still thinner samples, such that the frequency separation between the adjacent modes becomes large enough such that we may see several spectral lines associated with scattering from individual modes.

CHAPTER 6

Confined coherent acoustic plasmons

Thus far, I have presented the results of experiments designed to prove the existence of acoustic plasmon confinement from a purely frequency domain perspective. The natural extension is into the time-domain. In this chapter, I will demonstrate that I have not only generated coherent acoustic plasmons using ultrafast techniques, but due to the fact that we are able to generate exceptionally large photoexcited carrier densities, we can see the discretization of the acoustic plasmon into discernible standing waves. Further, I will demonstrate that the acoustic plasmon is in fact coupled to a coherent L_- oscillation, and this can serve as the driving term for the coherent oscillation of the acoustic plasmon.

6.1 Coherent coupled modes in opaque materials

The lower branch of the phonon-plasmon coupled mode plays an important role in our ability to generate and detect the coherent acoustic plasmons. For this reason, I believe it is beneficial to briefly discuss how we generate and detect coherent coupled modes in opaque materials. Let us begin by considering the case where we have two CW laser beams impinging on a sample of GaAs. If the beams are phase locked relative to each other and are chosen such that their difference frequency is equal to the phonon frequency ($\omega_1 - \omega_2 = \Omega$), we can generate a macroscopic coherent phonon field through a process known as stimulated Raman scattering (SRS) [67]. Through k-conservation, the excited phonons will have a well defined wavevector equal to $\mathbf{q} = \mathbf{k}_1 - \mathbf{k}_2$, where $\mathbf{k}_1$ and $\mathbf{k}_2$ are

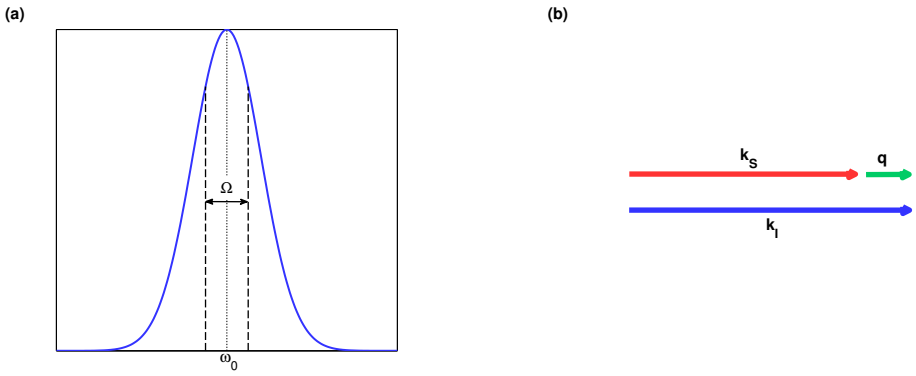

Figure 6.1: (a) Spectrum of the pump pulse with bandwidth large enough to support multiple frequency pairs with separation Ω, the LO phonon frequency. (b) Forward wave vector conservation. $\mathbf{k}_I$, $\mathbf{k}_S$, and $\mathbf{q}$ are the incident, scattered, and phonon wavevectors, respectively.

the wavevectors of the incident beams. The resulting optical signals from SRS are highly directional, coherent, and can be orders of magnitude more intense then corresponding spontaneous Raman signals.

6.1.1 Generation through impulsively stimulated Raman scattering

There is also another way to use SRS in conjunction with femtosecond pulses. As I show in Figure 6.1(a), we can use an optical pulse with a temporal width sufficiently small such that its spectral bandwidth is broad enough to support numerous frequency pairs, whose difference is equal to the phonon frequency. Since the two pairs originate from the same source, wavevector conservation is automatically satisfied in the forward direction as indicated in Figure 6.1(b). As a result, we are able to launch a coherent macroscopic phonon field upon the arrival of the pump pulse. The macroscopic oscillation of the lattice that accompanies the coherent phonon causes an oscillation in the refractive index of the crystal. Accordingly, by using a probe pulse set to strike the sample at a variable delay τ_D relative to pump, we can track the change in the sample induced by the pump as a function of time. This is the foundation of pump-probe spectroscopy based on impulsive stimulated Raman scattering (ISRS).

ISRS differs significantly between transparent and opaque materials. However, since my experiments involve light with photon energies above the fundamental energy gap of GaAs, I will restrict the following discussion to the latter. Comprehensive reviews of ISRS are available elsewhere [89, 77, 90]. In general, we can treat the coherent phonon field, defined by the normal displacement coordinate Q, as a damped driven harmonic oscillator governed by the differential equation

$$\frac{\partial^2 Q}{\partial t^2} + 2\gamma \frac{\partial Q}{\partial t} + \Omega^2 Q = F(t). \tag{6.1}$$

Here, γ describes the damping of the phonon and $F(t)$ is a driving force provided by the pump pulse through the Raman tensor. This is given by [91]

$$F(t) \propto \sum_{ij} \int_{-\infty}^{\infty} \int_{-\infty}^{\infty} d\omega d\Omega \exp(-i\Omega t) E_j(\omega) \pi_{ij}^R E_i^*(\omega - \Omega) \tag{6.2}$$

The difference between the transparent and opaque situations is due to the form of $F(t)$ in each of these two cases, and stems from the nature of the Raman tensor π_{ij}^R.

Stevens et al. discovered that the Raman tensor governing ISRS is distinct from the one responsible for spontaneous Raman scattering [91]. Namely, we can write

$$\pi_{ij}^R \approx \frac{\Xi_0}{4\pi\hbar} \left[\frac{\partial \Re\{\epsilon_{ij}\}}{\partial \omega} + 2i \frac{\Im\{\epsilon_{ij}\}}{\Omega} \right] \tag{6.3}$$

for ISRS and

$$\chi_{ij}^R \approx \frac{\Xi_0}{4\pi\hbar} \left[\frac{\partial \Re\{\epsilon_{ij}\}}{\partial \omega} + i \frac{\partial \Im\{\epsilon_{ij}\}}{\partial \omega} \right] \tag{6.4}$$

for spontaneous Raman scattering, where ϵ is the dielectric tensor of the material and Ξ_0 is the deformation potential, here treated as a constant. Though very similar, we see that there can be a great difference between the two Raman tensors for the case of absorptive materials. This is because the imaginary part of ϵ can be quite large on or above resonance, and in

this case, the second terms in the brackets of (6.3) and (6.4) dominate the expressions. For a transparent material on the other hand, the $\Im\{\epsilon\}$ is negligible and the two Raman tensors are virtually identical.

How, then, does this difference affect the driving term? Let us examine this by taking the limit where $\pi_{ij}^R \propto \Im\{\epsilon_{ij}\}/\Omega$, and inserting this expression into (6.2) with fields polarized along the y-direction. In this case, the diving force is

$$F(t) \propto \int_{-\infty}^{t} |E(t')|^2 \, dt'.$$

In the event that $E(t')$ is a δ-function, this is nothing more than the integral form of a step function, such that

$$F(t) = F_0 \Theta(t). \tag{6.5}$$

We can insert this into (6.1) and solve the differential equation. The solution for the displacement is

$$Q(t) = \frac{F_0}{\Omega^2 + \gamma^2} - \frac{F_0 e^{-\gamma t} \cos(\Omega t - \tan^{-1}(\gamma/\Omega))}{\Omega\sqrt{\Omega^2 + \gamma^2}}.$$

We see that the phonon displacement has a DC offset proportional to the magnitude of the step-like force. Further, the displacement oscillates as a cosine rather than the sine dependence that is characteristic of a transparent material [77].

There is another point we have to consider, and this has to do with the persistence of the driving term. We should reasonably expect that it decays in time as the system slowly returns to it pre-excited state. We can introduce this through a phenomenological damping Γ_F imposed upon the step function such that

$$F(t) = F_0 \Theta(t) \exp(-\Gamma_F t).$$

If we again solve for the phonon displacement, we obtain

$$Q(t) = \frac{F_0 e^{-\Gamma_F t}}{\Omega^2 + (\Gamma_F - \gamma)^2} - \frac{F_0 e^{-\gamma t} \cos\left(\Omega t - \tan^{-1}\left[(\Gamma_F - \gamma)/\Omega\right]\right)}{\Omega\sqrt{\Omega^2 + (\Gamma_F - \gamma)^2}}.$$

What we find is that the decay in the driving force causes both a change in the oscillators phase and amplitude, as well as a decay in the DC offset with time.

In the preceding discussion, we have made a fairly unphysical approximation in assuming that the incident pulse is δ-function like. In actuality, the mode-locked lasers we use produce Gaussian-like pulses with temporal widths $\lesssim 100$ fs. This can have a rather significant affect upon the amplitude of the phonon oscillation. What we find is that the amplitude of $Q(t)$ is proportional to a factor $e^{-(\Omega\tau_L)^2/2}$, where τ_L is the temporal pulse width of the pump. This means that if $\Omega\tau_L$ is large, the phonon amplitude will be significantly suppressed. As a result, when performing pump-probe experiments, we seek to ensure that the pulse width is smaller than the period of the phonon.

6.1.2 Detection through reflective electro-optic sampling

The final point we must consider involves the detection of the coherent phonon. In the reflection geometry, we use a probe pulse to measure the differential reflectivity of the sample; a change which results from the effect the phonon has upon the optical properties of the crystal. One approach is to employ reflective electro-optic sampling (REOS). In (100) GaAs, the principal axes are $x = [0\bar{1}\bar{1}]$, $y = [0\bar{1}1]$, and $z = [100]$. As a result of the electro-optic effect, the index along the first two directions are dependent upon the strength of the electric field along $[100]$. This relationship is governed by the expression [67]

$$\frac{x^2}{n_0 - \frac{n_0^3}{2} r_{41} E_z} + \frac{y^2}{n_0 + \frac{n_0^3}{2} r_{41} E_z} + \frac{z^2}{n_0^2} = 1, \tag{6.6}$$

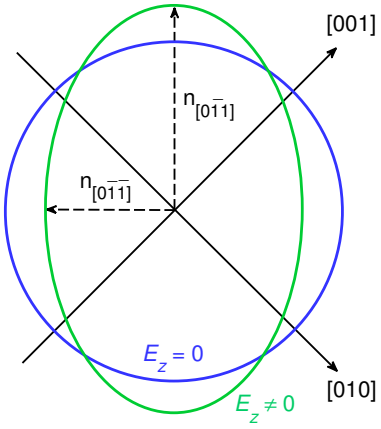

Figure 6.2: Indicatrix for GaAs.

where r_{41} is the only non-zero element of the electro-optic tensor of GaAs, and E_z is the electric field along the $[100]$ direction.

We can plot (6.6) with $z = 0$ to obtain the so-called indicatrix. As I show in Figure 6.2, in the absence of any field, the indicatrix is a circle implying that the refractive indices along $[0\bar{1}\bar{1}]$ and $[0\bar{1}1]$ are identical. However, when $E_z \neq 0$, the indicatrix is deformed into an ellipse resulting in different indices along the two directions. Since the LO phonon carries with it a longitudinal field, if the detected probe beam has a polarization that makes an angle δ with respect to $[001]$, then the index it sees is given by [92]

$$n(\delta) = \frac{1}{2} + \frac{n_0^3}{2} r_{41} E_z \sin(2\delta).$$

Given this index, the differential reflectivity is [92]

$$\frac{\Delta R}{R_0} = \frac{1}{R_0}\frac{\partial R}{\partial n}\Delta n,$$

where R_0 is the reflectivity in the absence of any perturbation. If we orient the probe polarization at 90° relative to $[001]$, split the reflected probe beam along $[0\bar{1}\bar{1}]$ and $[0\bar{1}1]$,

and send the two signals into a balanced detector, what we measure is [92]

$$\frac{\Delta R}{R_0} = \frac{1}{R_0}\left(R_{[0\bar{1}\bar{1}]} - R_{[0\bar{1}1]}\right) \approx \frac{4n_0^3 r_{41}}{n_0^2 - 1} E_{[100]}(t)\,.$$

Since the electric field is proportional to the lattice displacement $Q(t)$, we are able to detect the coherent phonon.

The theory developed in this section can be applied directly to the L_- modes in GaAs by noting that, in this case, we need to replace the fixed LO phonon frequency with the carrier density dependent frequency of the L_- mode. As our photoexcited densities are quite large ($> 10^{18}$ cm^{-3}), this frequency will be essentially pegged at the TO phonon frequency as we can see from Figure 3.6. In addition, we can safely disregard the L_+ branch because the photoexcited densities are large enough that the frequency is far beyond what we can excite in our experiment with the limited bandwidth of our pump pulse.

6.2 Confined coherent acoustic plasmons

At first glance, we would imagine that we could generate coherent acoustic plasmons in much the same way we do in the case of phonons. However, this proves to be quite challenging due to the need for large EHP densities. It might seem as though simply using a pump-probe experiment with light resonant with the band gap would overcome this issue, but unfortunately, this introduces another complication. In my early experiments, I attempted just this, and the result was a probe signal mired in a great deal of electronic background associated with the cooling of the photoexcited carriers. This was a problem as the signals associated with both coherent phonons and plasmons are relatively small, and any attempts to use standard techniques to remove this background proved ineffective. The solution to this problem involves a modification of the standard pump-probe scheme that leverages the power of phase sensitive detection and also the interaction between the L_- coupled mode and the acoustic plasmon.

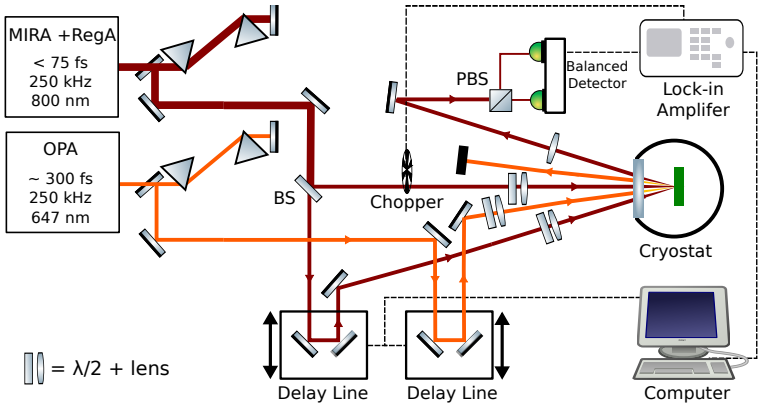

Figure 6.3: Double pump-probe scheme.

6.2.1 Double pump-probe scheme

The essence of the modified pump-probe scheme is to use two pump pulses with a fixed separation in time and different central frequencies using the geometry shown in Figure 6.3. The first pulse is in the infrared (IR) with a pulse width of ~ 75 fs polarized along the $[001]$ direction. Since the period of the coupled mode at high densities is approximately 110 fs, this pulse is capable of generating a coherent L_- mode with a relatively large amplitude. The second pump is in the visible and arrives at the sample 2 ps after the IR pump. The IR and visible pumps have focal spot sizes of 200 μm and 100 μm, respectively. The central energy of the visible pump is set to 1.92 eV, which is very close the the energy of the $E_0 + \Delta_0$ gap. The visible pulse has a width of ~ 300 fs, which is too large to generate a coherent coupled mode oscillation of appreciable amplitude. This means that the primary role of the visible pump is to inject carriers into the photoexcited volume. The dynamics of the system are measured with an IR probe polarized along the $[010]$ direction with the same characteristics as the IR pump at a variable delay of -1 to 13 ps relative to the arrival of the IR pump.

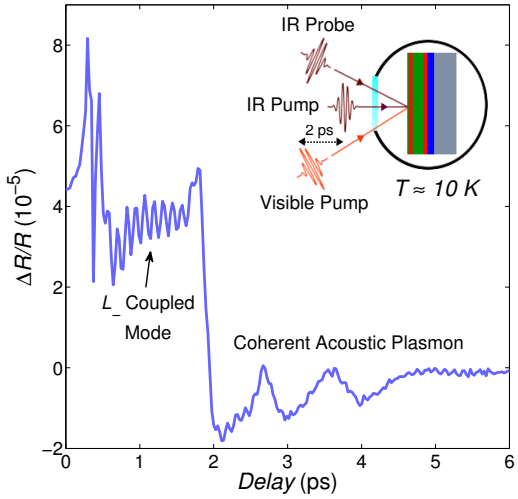

Figure 6.4: Typical time domain results from my modified pump-probe experiment. The inset shows the scattering geometry and pump pulse sequence. This experiment used a 15 mW IR pump, 12 mW visible pump, and 5 mW IR probe. The sample was maintained at 10 K using a liquid He immersion cryostat.

6.2.2 Experimental results

Figure 6.4 shows the essential features observed in a typical time-domain experiment. Following the IR pump, we see approximately 8 THz oscillations associated with the generation of the L_{-} mode. Two picoseconds following the IR pump, we observe a large shift in the reflectivity coincident with the arrival of the visible pump, which is followed by a large amplitude low frequency oscillation due to the generation of the coherent acoustic plasmon. Note that the heavy Landau damping of the acoustic plasmon through single particle excitations is evidenced by the modes large decay rate.

In order to explicitly show that the low frequency oscillation is an acoustic plasmon, I examined the oscillation at varying visible pump powers. This is because the acoustic plasmon frequency depends on the carrier density, which we can vary by attenuating the beam. Upon excitation by the pump, the surface carrier density is equivalent to [93]

$$n_{surface} = Af\frac{\alpha}{E},$$

where A is the absorptivity of the material, f is the fluence (energy per unit area) of the pulse, α is the absorption coefficient, and E is the photon energy. Due to the absorption coefficient, the carrier density at any depth z into the sample is given by

$$n(z) = n_{surface} \exp(-\alpha z).$$

Thus, we can determine the carrier density by integrating over $n(z)$:

$$n = \frac{1}{d_{active}} \int_0^{d_{active}} n_{surface} \exp(-\alpha z)\, dz.$$

In general, these estimates of carrier density are prone to variability due to the fact that focal spot size measurements can be somewhat inaccurate, and even a 10% error in the measurement can introduce a rather large variation in the estimated density. Unfortunately, in situ measurements of carrier density in photoexcited samples is a challenge in an of itself, particularly in ultrafast experiments. Still, as we shall see, the numerical estimates of the density provided a good correspondence with the theoretical predictions for the acoustic plasmon's density dependence, confirming their veracity.

Figure 6.5 shows the time traces (after the arrival of the visible pump) and corresponding Fourier transforms for a 1500 Å, 1150 Å, and 6000 Å sample at various photoexcited carrier densities. In all three samples, we can see low frequency oscillations whose Fourier peaks exhibit a marked change with carrier density. In the case of the 1150 Å sample, we see two clear Fourier peaks, indicating the simultaneous presence of two modes. The acoustic plasmon should show a fractional power law dependence with the carrier density. As such, I extracted the locations of the Fourier peaks at each density for the three samples and compared these to the theoretically expected n dependence of the acoustic plasmon frequency under the random phase approximation. I did this by first calculating the susceptibilities (Equations (2.33)-(2.37)), dielectric function (Equation (3.41)), and structure

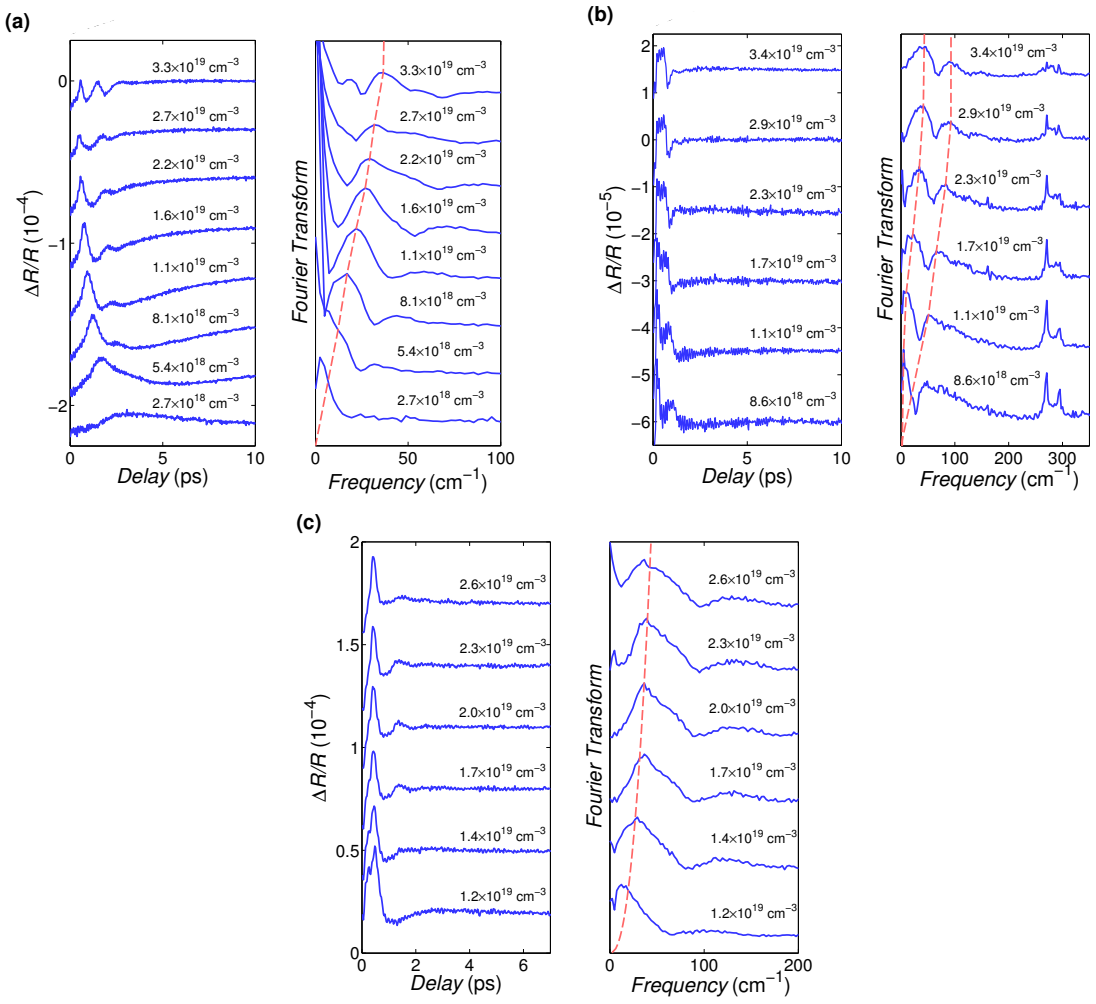

Figure 6.5: Time-domain results and corresponding Fourier transforms for (a) the 1500 Å, (b) 1150 Å, and (c) 6000 Å samples.

factor (Equation (3.44)) for the acoustic plasmon over a range of carrier densities. For the wavevectors, I used several values corresponding to multiple orders of acoustic plasmon standing waves for the three samples as given by Equation (2.52). I then used the peak location of the acoustic plasmon at each density to determine the theoretical n-dependence in each case. In these calculations, I used a value of 400 K for the carrier temperature and 5.9 meV for the carrier damping, which were commensurate with theoretical and experimental values, respectively [94, 50].

Figure 6.6 shows the experimental acoustic plasmon frequencies as a function of photoexcited carrier density for the three samples. The blue and red shaded regions represent the predicted density dependence of the acoustic plasmon frequency computed for the first and second modes, respectively, for each sample. The lower and upper bounds of each of the shaded regions are calculated at dampings of $\Gamma = 5.9$ meV and $\Gamma = 0.08$ meV, respectively, at a carrier temperature of $T = 400$ K with various values of n for the appropriate value of q for the given mode. The blue and red squares are the experimental data points. The error bars in the experimental data represent the Fourier transform (vertical) and focal spot measurement (horizontal) errors. For the 1500 Å sample, I observed a mode that has an n dependence that coincides with an $m = 1$ mode ($q = 2.1 \times 10^5$ cm^{-1}). The inset shows the Fourier transform for the $n = 2.2 \times 10^{19}$ cm^{-3} experimental datapoint with theoretical calculations of the imaginary part of the electron response function for the first (blue line) and second (red line) modes (calculated with $n = 2.2 \times 10^{19}$ cm^{-3}, $T = 400$ K, and $\Gamma = 5.9$ meV). We can see that the $m = 1$ mode calculation shows a reasonably good agreement with the experimental Fourier peak. For the 1150-Å sample, I see two modes corresponding to $m = 1$ ($q = 2.7 \times 10^5$ cm^{-1}) and $m = 2$ ($q = 5.4 \times 10^5$ cm^{-1}). Here, because of the large photoexcited carrier densities, the spacing between the modes in frequency is large enough, such that the individual modes can be clearly distinguished. This is in direct contrast to the spontaneous scattering experiments of Chapter 5, where the frequency separation was insufficient to overcome the spectral

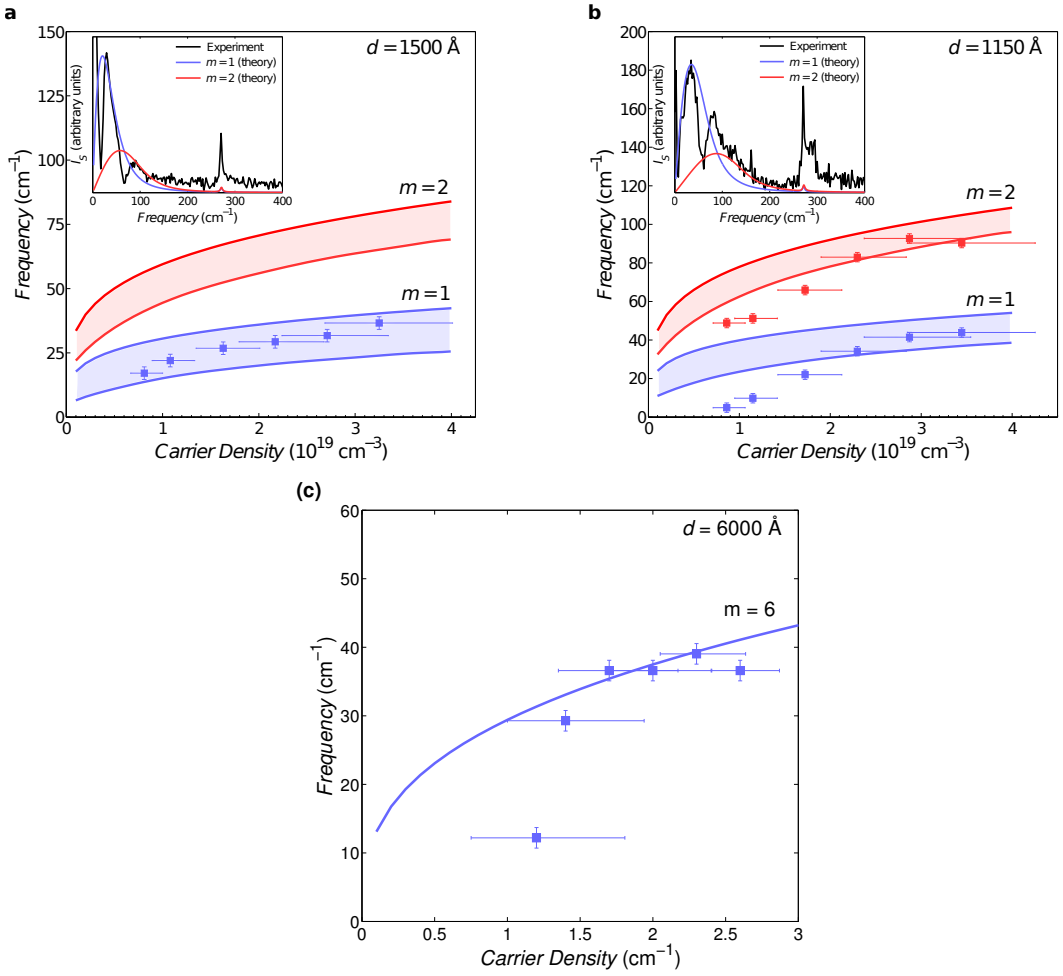

Figure 6.6: (a) The theoretically calculated carrier density dependence of the acoustic plasmon frequency for the coherent acoustic plasmon standing wave in the 1500 Å GaAs layer. The experimental data is shown as blue squares. The inset shows a representative Fourier transform of the experimental time-trace for $n = 2.2 \times 10^{19}$ cm^{-3}. The blue and red lines in the inset are the theoretically calculated imaginary part of the electron response function for the $m = 1$ and $m = 2$ modes, respectively, at $\Gamma = 5.9$ meV. (b) Similar results for a 1150 Å GaAs layer for the the $m = 1$ and $m = 2$ modes. The inset shows a representative Fourier transform of the experimental time-trace for $n = 2.3 \times 10^{19}$ cm^{-3}. The blue and red lines in the inset are the theoretically calculated imaginary part of the electron response function for the $m = 1$ and $m = 2$ modes, respectively, at $\Gamma = 5.9$ meV. (c) The theoretically calculated carrier density dependence of the acoustic plasmon frequency for the $m = 6$ coherent acoustic plasmon standing wave mode in the 6000 Å GaAs layer. The experimental data are shown as blue squares.

overlapping of the modes. We can see this in the inset of Figure 6.6(b), where the Fourier transform of the $n = 2.3 \times 10^{19}$ cm^{-3} experimental datapoint shows two clear peaks. The red and blue lines in the inset are again theoretical calculations of the imaginary part of the electron response function (calculated with $n = 2.3 \times 10^{19}$ cm^{-3}, $T = 400$ K, and $\Gamma = 5.9$ meV). For both modes, the experimental peaks are noticeably narrower that than the theoretical predictions. This may be due to interference effects between the two modes as evidenced by the dramatic dip between the Fourier peaks.

In both the 1150 Å and 1500 Å samples, there is a clear breakdown in wavevector conservation due to the strong confinement of the acoustic plasmon. As such, the relevant wavevector is determined by the thickness of the sample as evidenced by its good agreement with the theoretical predictions made under this assumption. As a result, rather than seeing a mode with ω_{AP} vs. n behavior matching $q = 4\pi n/\lambda_{probe} \approx 5.7 \times 10^5$ cm^{-1} (as in a bulk sample), both the 1500 Å and 1150 Å samples have a dominant modes ($m = 1$) which have wavevectors that are very different from the backscattering wave vector associated with the probe pulse. The presence of this mode is clear evidence of confinement of the coherent acoustic plasmon as a standing wave. The case of the 6000 Å sample is more perplexing. Figure 6.6(c) shows the experimental acoustic plasmon frequency as a function of carrier density for this sample. We see that for all but the lowest carrier density, the experimental data is in good agreement with the theoretical predictions for an $m = 6$ mode (3.14×10^5 cm^{-1}) at $\Gamma = 5.9$ meV. This is in contrast to the other two samples where the dominant most was the fundamental. This may be due to the fact that in the 6000 Å sample, we are beginning to enter the transitionary regime where k-conservation begins to reestablish due to the relatively small wavevector spacing between the various standing wave modes.

As I previously noted, the coherent acoustic plasmon is significantly Landau damped, and as a result the oscillations in the time-domain decay within a few cycles. Figure 6.7 confirms this assessment, as we can see that at $n = 2.3 \times 10^{19}$ cm^{-3}, the acoustic plasmon

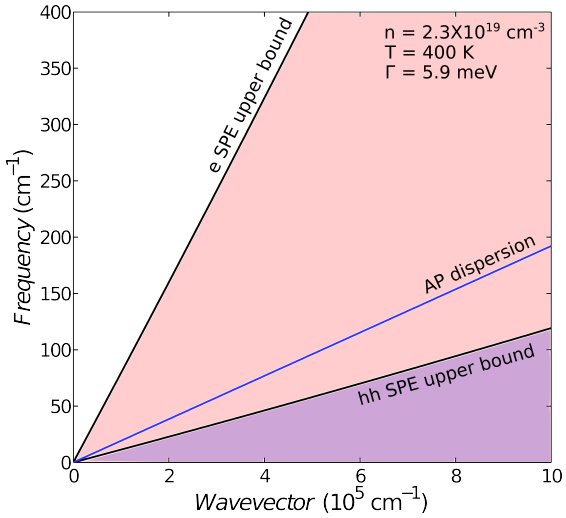

Figure 6.7: Calculated acoustic plasmon dispersion for the parameters listed in the figure and approximate electron and heavy hole SPE continua.

is completely embedded within the electron SPE continuum. Here, the upper bounds of the SPE are calculated from $T = 0$ K behavior and are qualitative only as the SPE boundaries become diffuse at non-zero temperatures. The Landau damped nature of the acoustic plasmon is a consistent feature across the range of photoexcited carrier densities, and not just for those pictured in Figure 6.7.

It should be noted that the spectral features in the spontaneous light scattering experiments and the oscillations in pump-probe studies are not due to the surface waves because first and foremost, the holes do not contribute to the surface polariton as their contributions are heavily damped out by single particle excitations. Further, the splitting between even and odd modes is negligible due to the relatively large thicknesses associated with my samples. As a result, there should not be a pronounced thickness dependence in either the spontaneous spectra or the time-domain oscillatory frequencies if both these features were due to surface waves. Finally, the surface polaritons originating from the electrons have a large peak in the density of states at frequencies much higher than what I experimentally observe at any given plasma density.

6.2.3 PSD and generation of coherent acoustic plasmons

In a pump-probe scheme, we need some method by which we can differentiate the pump-induced response from other complicating signals originating from laser noise, thermal fluctuations in the laboratory, and probe-induced changes to the sample. There are a multitude of ways to do this, but one of the most convenient involves amplitude modulating the pump with a known frequency. We can then extract the pump-induced change in the reflected probe beam by isolating the Fourier component of the differential reflectivity with the same modulation. This is the principle behind phase sensitive detection (PSD).

In the laboratory, we implement PSD using a lock-in amplifier (SRS 830). First, we split the probe pulse into it's two constituent polarizations and then send each component into a balanced detector, as required for REOS. We send the output of the detector to a unity gain preamplifier. The preamplifier serves as a low pass filter with a 10 kHz bandwidth. Since the repetition rate of the laser is 250 kHz and a typical photodiode has a bandwidth of over 50 MHz, we can regard the the input signal as a continuous in time with non-zero values approximately every 4 μs. The low pass filter pre-conditions this signal by removing high frequency components above approximately 10 kHz originating from the laser and other sources. This result is then sent to the lock-in amplifier.

The first stage of the lock-in amplifier is an analog-to-digital (A/D) converter that samples the continuous time input signal at 256 kHz. By the Nyquist theorem, the highest frequency component in the input signal that will be non-aliased will be at 128 kHz. Since our low pass preamplifier removed most of the extraneous signal above 10 kHz, and also because the frequency component we are interested in is at 2 kHz (the chopping frequency), this condition is not a problem in our experiment. The signal now undergoes multiplication with an internally generated sine wave oscillating at the reference frequency supplied by the chopper. The resultant signal is now comprised predominantly of a signal oscillating at two times the reference frequency and one that is nearly DC. The signal after the PSD is low-pass filtered to extract the latter. It is this DC signal that we measure at various

delays and what constitutes the time-trace I obtain in my experiment. The importance of phase sensitive detection within the context of my experiment is that we can only measure the direct effect of the pump if it is modulated in some manner. In my experiment, I only chop the IR pump. Ostensibly, we would imagine that phase sensitive detection would only allow us to measure the oscillation in reflectivity associated with the coherent coupled mode. Since the signal due exclusively to the visible pump would be attenuated away in the detection process, even if we were to directly excite a coherent acoustic plasmon, we should not be able to detect the signal associated with it.

What if, however, there were some interaction between the two excitations? Namely, if we were to treat both as a system of coupled quantum harmonic oscillators, how would the detected signal? To examine this, let us begin by considering a coupled system consisting of phonons and acoustic plasmons. The Hamiltonian for a the coupled oscillator system in second quantization can be written as [95]

$$\begin{aligned} H &= \hbar\omega_L \sum_{\mathbf{k}} \hat{a}^\dagger_{\mathbf{k}} \hat{a}_{\mathbf{k}} + \hbar\omega_{AP} \sum_{\mathbf{k}} \hat{b}^\dagger_{\mathbf{k}} \hat{b}_{\mathbf{k}} \\ &\quad -\hbar\beta \sum_{\mathbf{k}} \left(\hat{a}_{\mathbf{k}} \hat{b}_{-\mathbf{k}} + \hat{a}_{\mathbf{k}} \hat{b}^\dagger_{\mathbf{k}} + \hat{a}^\dagger_{\mathbf{k}} \hat{b}_{\mathbf{k}} + \hat{a}^\dagger_{\mathbf{k}} \hat{b}^\dagger_{-\mathbf{k}} \right). \end{aligned} \tag{6.7}$$

Here, $a^\dagger_{\mathbf{k}}$ and $a_{\mathbf{k}}$ ($b^\dagger_{\mathbf{k}}$ and $b_{\mathbf{k}}$) are the creation and annihilation operators for the coupled mode (acoustic plasmon) and ω_L (ω_{AP}) is the frequency of the coupled mode (acoustic plasmon). The position operators for the phonon and plasmon oscillators are

$$\hat{Q}_{\mathbf{k}} = \sqrt{\frac{\hbar}{2\omega_L}} \left(\hat{a}_{\mathbf{k}} + \hat{a}^\dagger_{-\mathbf{k}} \right) \tag{6.8}$$

$$\hat{P}_{\mathbf{k}} = i\sqrt{\frac{\hbar\omega_L}{2}} \left(\hat{a}^\dagger_{-\mathbf{k}} - \hat{a}_{\mathbf{k}} \right) \tag{6.9}$$

$$\hat{q}_{\mathbf{k}} = \sqrt{\frac{\hbar}{2\omega_{AP}}} \left(\hat{b}_{\mathbf{k}} + \hat{b}^\dagger_{-\mathbf{k}} \right) \tag{6.10}$$

$$\hat{p}_{\mathbf{k}} = i\sqrt{\frac{\hbar\omega_{AP}}{2}} \left(\hat{b}^\dagger_{-\mathbf{k}} - \hat{b}_{\mathbf{k}} \right) \tag{6.11}$$

To begin, we calculate the commutators of the ladder operators and the Hamiltonian as

$$\begin{aligned}
\left[\hat{a}_{\mathbf{q}}, \hat{H}\right] &= \hbar\omega_L \hat{a}_{\mathbf{q}} - \hbar\beta\hat{b}_{\mathbf{q}} - \hbar\beta\hat{b}^{\dagger}_{-\mathbf{q}} && (6.12)\\
\left[a^{\dagger}_{-\mathbf{q}}, \hat{H}\right] &= -\hbar\omega_L \hat{a}^{\dagger}_{-\mathbf{q}} + \hbar\beta\hat{b}_{\mathbf{q}} + \hbar\beta\hat{b}^{\dagger}_{-\mathbf{q}} && (6.13)\\
\left[\hat{b}_{\mathbf{q}}, \hat{H}\right] &= \hbar\omega_{AP} \hat{b}_{\mathbf{q}} - \hbar\beta\hat{a}_{\mathbf{q}} - \hbar\beta\hat{a}^{\dagger}_{-\mathbf{q}} && (6.14)\\
\left[b^{\dagger}_{-\mathbf{q}}, \hat{H}\right] &= -\hbar\omega_{AP} \hat{b}^{\dagger}_{-\mathbf{q}} + \hbar\beta\hat{a}_{\mathbf{q}} + \hbar\beta\hat{a}^{\dagger}_{-\mathbf{q}}. && (6.15)
\end{aligned}$$

Using these and the Ehrenfest theorem, we obtain

$$\begin{aligned}
\frac{d}{dt}\left\langle \hat{Q}_{\mathbf{k}} \right\rangle &= \left\langle \hat{P}_{\mathbf{k}} \right\rangle && (6.16)\\
\frac{d}{dt}\left\langle \hat{q}_{\mathbf{k}} \right\rangle &= \left\langle \hat{p}_{\mathbf{k}} \right\rangle && (6.17)
\end{aligned}$$

Now, we can derive the expression for the canonical momentum:

$$\begin{aligned}
\frac{d}{dt}\left\langle \hat{P}_{\mathbf{k}} \right\rangle &= \frac{1}{i\hbar}\left\langle \left[\hat{P}_{\mathbf{k}}, \hat{H}\right] \right\rangle \\
&= -\omega_L^2 \left\langle \hat{Q}_{\mathbf{k}} \right\rangle + 2\beta\sqrt{\frac{\hbar\omega_L}{2}} \left\langle \left(\hat{b}^{\dagger}_{-\mathbf{k}} + \hat{b}_{\mathbf{k}}\right) \right\rangle \\
&= -\omega_L^2 \left\langle \hat{Q}_{\mathbf{k}} \right\rangle + 2\beta\sqrt{\omega_L\omega_{AP}} \left\langle \hat{q}_{\mathbf{k}} \right\rangle , && (6.18)
\end{aligned}$$

We can derive a similar expression for $\langle \hat{q}_{\mathbf{k}} \rangle$ as well:

$$\frac{d^2}{dt^2}\left\langle \hat{q}_{\mathbf{k}} \right\rangle = -\omega_{AP}^2 \left\langle \hat{q}_{\mathbf{k}} \right\rangle + 2\beta\sqrt{\omega_L\omega_{AP}} \left\langle \hat{Q}_{\mathbf{k}} \right\rangle . \quad (6.19)$$

To account for damping of these oscillators, we include a phenomenological damping term for both the coupled mode and acoustic plasmon along with driving terms that accounts for

the excitation of each of these quasiparticles. Doing so, we obtain

$$\frac{d^2}{dt^2}\left\langle \hat{q}_{\mathbf{k}}\right\rangle + \gamma_{AP}\frac{d}{dt}\left\langle \hat{q}_{\mathbf{k}}\right\rangle + \omega_{AP}^2\left\langle \hat{q}_{\mathbf{k}}\right\rangle = F_{AP}\left(t\right) + 2\beta\sqrt{\omega_L\omega_{AP}}\left\langle \hat{Q}_{\mathbf{k}}\right\rangle \quad (6.20)$$

$$\frac{d^2}{dt^2}\left\langle \hat{Q}_{\mathbf{k}}\right\rangle + \gamma_L\frac{d}{dt}\left\langle \hat{Q}_{\mathbf{k}}\right\rangle + \omega_L^2\left\langle \hat{Q}_{\mathbf{k}}\right\rangle = F_L\left(t\right) + 2\beta\sqrt{\omega_L\omega_{AP}}\left\langle \hat{q}_{\mathbf{k}}\right\rangle . \quad (6.21)$$

At this point, we can make a few assumptions. First, since the visible pump is not chopped, the only modulation in $F_{AP}\left(t\right)$ arises from the 250 kHz repetition rate of the OPA. As a result, most of the signal associated with this term will be eliminated by the pre-amplifier and lock-in system. Second, we presume that the carrier density injected by the visible pump follows a simple rate law with the pump intensity [96]. That is

$$\frac{dN}{dt} = N_0 I\left(t\right) \quad (6.22)$$

where N_0 is the final value of the density following the visible pump. Since the acoustic plasmon frequency depends on the carrier density, ω_{AP} will also be time dependent. With these assumptions we have the following system of equations which I solved numerically

$$\frac{d^2}{dt^2}\left\langle \hat{q}_{\mathbf{k}}\right\rangle + \gamma_{AP}\frac{d}{dt}\left\langle \hat{q}_{\mathbf{k}}\right\rangle + \omega_{AP}^2\left(t\right)\left\langle \hat{q}_{\mathbf{k}}\right\rangle = 2\beta\sqrt{\omega_L\omega_{AP}\left(t\right)}\left\langle \hat{Q}_{\mathbf{k}}\right\rangle \quad (6.23)$$

$$\frac{d^2}{dt^2}\left\langle \hat{Q}_{\mathbf{k}}\right\rangle + \gamma_L\frac{d}{dt}\left\langle \hat{Q}_{\mathbf{k}}\right\rangle + \omega_L^2\left\langle \hat{Q}_{\mathbf{k}}\right\rangle = F_L\left(t\right) + 2\beta\sqrt{\omega_L\omega_{AP}\left(t\right)}\left\langle \hat{q}_{\mathbf{k}}\right\rangle . \quad (6.24)$$

In solving this system, $F_L\left(t\right)$ was treated as a step function in time consistent with the generation mechanism of coherent phonons in opaque materials, and β was a free parameter. In practice, the signal sent to a detector will be the sum of contributions due to $\hat{q}_{\mathbf{k}}$ and $\hat{Q}_{\mathbf{k}}$ ($\Delta R/R \propto \left\langle \hat{Q}_{\mathbf{k}}\right\rangle + \zeta\left\langle \hat{q}_{\mathbf{k}}\right\rangle$). The relative contribution of these two terms will depend on the relationship between $q_{\mathbf{k}}$ and the associated polarization. Equations (6.23) and (6.24) reveal that the coupled mode and acoustic plasmon are coupled through their amplitudes. Further, even in the absence of a driving field on the acoustic plasmon, the coupling term on the right hand side of (6.23) can coherently drive the oscillator. This is the proposed

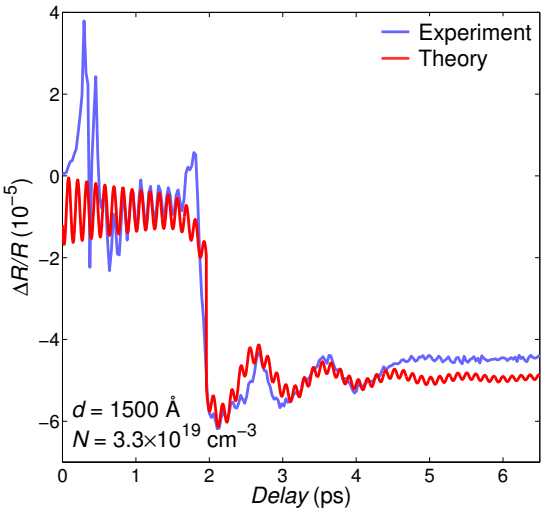

Figure 6.8: Comparison between the experimental (blue) and theoretical (red) differential reflectivity calculated using the coupled oscillator model.

generation mechanism given my experimental configuration.

The exact value of ζ and the constant of proportionality depend upon the physical relationship between the phonon and plasmon amplitudes and the differential reflectivity. However, my experiment cannot distinguish between the detection efficiency (ζ) and the coupling strength (β) contributions to the measured acoustic oscillation magnitude. For this reason, I set $\zeta = 1$, and the parameter space for the model is reduced to β and an overall multiplicative factor (-1). Figure 6.8 shows the theoretically calculated differential reflectivity (in red) against an experimentally obtained time scan (in blue). In calculating the model, I used $\beta = 2.50 \times 10^{12}$ s^{-1}, $F_0 = 0.22 \times 10^{23}$, $\gamma_L = 1.00 \times 10^{12}$ s^{-1}, and $\gamma_{AP} = 1.80 \times 10^{12}$ s^{-1}. The value for F_0 and γ_L were determined by calculating the differential reflectivity trace with $\beta = 0$ and fitting it to experimental results in the absence of a visible pump. The values of β and γ_{AP} were chosen to best fit the experimental data. The theoretical calculation was only modified by adding a step function-like offset at 2 ps ($-0.32 \times 10^{-4} \cdot \Theta(t-2)$) to account for the sudden shift in reflectivity associated with the arrival of the visible pump. This modification had no impact upon the oscillation frequency. Despite slight differences in the background (due to the reflectivity changes associated with

the electronic background), we see a good correspondence between the oscillatory frequencies and amplitudes.

6.3 Summary

Using ultrafast excitation, I have successfully generated confined coherent acoustic plasmons using an all-optical technique. These modes exhibit a carrier density dependence that is in good agreement with the theoretically expected behavior of acoustic plasmon standing wave modes based on the random phase approximation. Owing to the large separation in frequency between adjacent modes, we are able to see multiple distinguishable discrete modes in the 1150 Å and 6000 Å samples. The generation of these modes can be explained using a phenomenological coupled oscillator model. Here, the coherent acoustic plasmon is generated through a coupling with the L_- mode generated via impulsively stimulated Raman scattering. While these modes are heavily Landau damped, the successful generation of the coherent mode may open possibilities for the generation of these modes in systems where damping effects are mitigated [97, 98].

CHAPTER 7

Conclusions and future work

Acoustic plasmons in semiconductors represent longitudinal acoustic oscillations of the electron-hole plasma. In essence, we can associate these oscillations with a second type of sound supported by the crystal that exists in addition to that supported by longitudinal acoustic phonons. In slabs where the carriers are confined, treating the electron-plasma as a fluid reveals that the acoustic plasmon exists as a discrete set of standing waves. Each of these modes has a discrete wavevector that is an integer multiple of a fundamental value associated with the lowest order mode; this value is proportional to the inverse sample thickness. As a result, as sample thickness diminishes, the wavevector spacing between adjacent modes increases, and owing to the linearity of the acoustic plasmon's dispersion, the frequency separation between modes increases concomitantly.

In samples on the order of 1000 Å, the spacing between modes becomes large enough that the assumption of wavevector conservation breaks down, allowing light to couple to a range of modes that would otherwise be forbidden. As a result, in light scattering experiments, we see that the acoustic plasmon frequency changes dramatically for a thin sample relative to thicker samples. We can model this result by leveraging the analogy with LA phonons, and invoke the photoelastic effect to explain the efficiency with which a given mode contributes to the scattering spectra. Theoretical calculations under this framework are in agreement with the experimental results. It is initially puzzling as to why we do not see discrete scattering peaks associated with several modes, as we do for the case of con-

fined LA phonons. However, this can be explained by the large line width of the acoustic plasmon stemming from its heavy Landau damping over the range of wavevectors that are accessible to us in light scattering experiments. Given the thickness of my samples, the wavevector spacing between adjacent modes was insufficient to overcome the heavy overlapping of the spectra, resulting in a single scattering peak that was the combination of the contributions of several modes.

Using ultrafast pump-probe techniques, I have demonstrated that we can also generate coherent acoustic plasmons. Moreover, since the the photoexcited carrier densities are much larger in ultrafast experiments than in spontaneous scattering, the frequency separation between acoustic plasmon standing wave modes becomes large enough that we can distinguish between adjacent modes. As such, not only do we see coherent generation of the acoustic plasmon, but also standing wave behavior, with some samples exhibiting multiple modes simultaneously. The experimental results are in excellent agreement with theoretical predictions under the random phase approximation. The generation mechanism in my experiment is explained by coupling of the acoustic plasmon to the coherent L_- mode.

Future spontaneous scattering experiments should focus upon thinner samples where the mode spacing is large enough to allow us the ability to discern the spectral contributions due to each mode. This, however, will necessitate great care due to the diminished signal and carrier density control in thinner samples. It would also be beneficial to use a two color spontaneous scattering experiment. Here, the photoexcited electron hole plasma is generated using a resonant beam, and a second off-resonance beam is used to perform the light scattering measurement. The carrier temperature may still be estimated using the spectra obtained from the resonant beam. The immediate benefit in such a scheme is that there is no longer any photoluminescence to contend with, which greatly simplifies the analysis procedure. Moreover, the polarized component of the SPE vanishes along with the resonance enhancement in the spectra making the analysis of the plasma parameters

and acoustic plasmon peak more straight-forward. The difficulty in this experiment lies in the proper overlapping of the two beams. In particular, the off-resonant beams must be focused to a much smaller spot size than the already tightly focused resonant beam in order to ensure that a homogenous carrier distribution can be interrogated.

The natural extension of the ultrafast experiments contained in this work is into the realm of direct excitation of the acoustic plasmon. Here, the coupling to L_- mode can be bypassed by using a temporally broad pulse (as compared to the L_- mode period) in a single pump probe scheme. The main difficulty in such an experiment is associated with the large electronic background in the probe signal if the resonant pump pulse is chopped. The difficulties associated with background subtraction may be eased using transient grating techniques [99] or through the use of a non-degenerate pump-probe scheme with careful choice of pump and probe frequencies [100]. In addition to direct excitation, it would be interesting to probe the transition to k-conservation with progressively thicker samples, though this may require the use of kHz systems to generate the required carrier densities.

Another possible avenue for future research involves potentially long-lived acoustic plasmons. It has been shown that highly non-equilibrium plasma distributions with unoccupied low momentum states may posses an undamped acoustic plasmon mode [97, 98]. Figure 7.1 shows a sample calculation of $\Im\{1/\epsilon\}$ for a boxcar-like carrier distribution at $n = 1 \times 10^{18}$ cm^{-3} for a two-component plasma assuming effective mass energy dispersions ($m_1 = 0.067m_0$ and $m_2 = 0.47m_0$ where m_0 is the electron mass). Only states between $k = 3.1 \times 10^6$ cm^{-1} and $k = 3.9 \times 10^6$ cm^{-1} are occupied. In such systems an undamped pocket forms between the SPE of the electrons and holes. As a result, the acoustic plasmon dispersion, which passes through this region, is not coupled to the SPE of either electrons or holes and exists as an undamped mode. In general, these distributions are very short lived, and equilibrate within a few hundred femtoseconds, so the experimental challenge will be to isolate these oscillations spectrally or in the time-domain before this occurs.

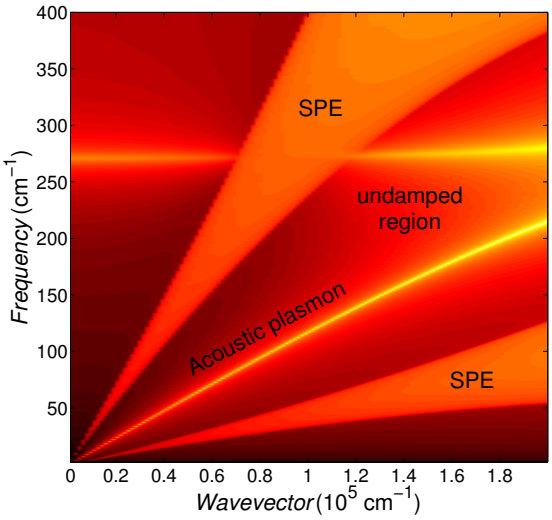

Figure 7.1: Undamped acoustic plasmon mode in a simple two-component plasma.

Due to the requirement for high carrier densities, coupled with their relatively large damping, light scattering from acoustic plasmons has remained rather elusive. While spontaneous light scattering from acoustic plasmons has been previously achieved, in these experiments, the effects of geometrical confinement was an unanswered question. My experiments serve to show that the acoustic plasmon can exist as a confined mode. The successful reproduction of the spectral line shape associated with the acoustic plasmon mode using the photoelastic model is particularly exciting, as it serves as strong confirmation of the analogy between LA phonons and acoustic plasmons. Furthermore, the ability to generate a coherent state of acoustic plasmons represents the generation of a new type of sound wave in a semiconductor, that till now, has not been seen. Owing to the relationship between sound waves and heat transport within the crystal, this discovery introduces new possibilities for research into the thermal properties of semiconducting materials.

APPENDIX A

Phonons

A.1 Optical and acoustic lattice vibrations

When the lattice vibrates, the atoms execute small amplitude oscillations as though the particles are interconnected by springs (i.e. atomic bonds). We can treat these vibrations classically, and we then obtain two branches of vibrations of acoustic and optical character. To get a physical interpretation of these branches, we consider a linear lattice with two atoms per unit cell as shown in Figure A.1(a). In this system, acoustic vibrations correspond to the two atoms in the cell moving in the same direction as shown in Figure A.1(b). Optical vibrations are those where the two atoms move in opposite directions such that the center of mass of the unit cell is not displaced, as in Figure A.1(c). Classically, we can treat

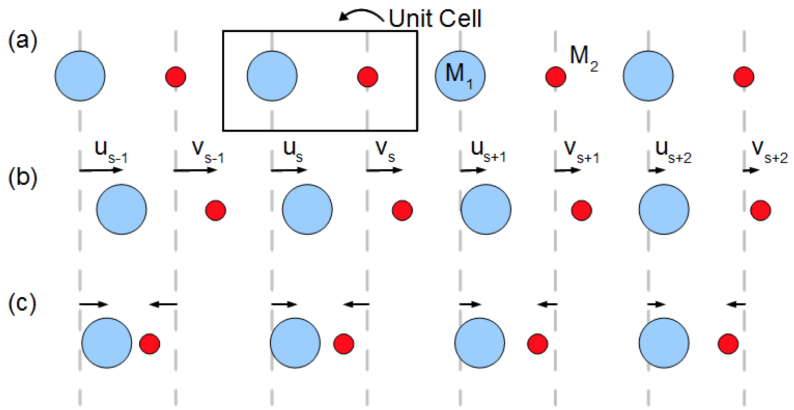

Figure A.1: Lattice vibrations of a diatomic 1D chain.

this linear diatomic system as coupled oscillators. If we only consider nearest neighbor interactions, the equation of motion are given by

$$M_1 \frac{d^2 u_s}{dt^2} = C\left(v_s + v_{s-1} - 2u_s\right) \tag{A.1}$$

$$M_2 \frac{d^2 v_s}{dt^2} = C\left(u_{s+1} + u_s - 2v_s\right), \tag{A.2}$$

where M_1 and M_2 are the masses of the first and second atom in the unit cell. If we treat the 1D chain as periodic with constant a_0, we can solve these equations using periodic traveling wave solutions of the form

$$u_n(t) = Ae^{i(qna_0 - \omega t)} \tag{A.3}$$

$$v_n(t) = Be^{i(qna_0 + qna_0/2 - \omega t)}. \tag{A.4}$$

We can insert Equations (A.3) and (A.4) into (A.1) and (A.2) in order to obtain

$$\begin{aligned} -M_1\omega^2 A &= C\left(Be^{iqa_0/2} + Be^{-iqa_0/2} - 2A\right) \\ -M_2\omega^2 B &= C\left(Ae^{iqa_0/2} + Ae^{-iqa_0/2} - 2B\right), \end{aligned}$$

which we can solve for the eigenvalues by forming the determinant

$$\begin{vmatrix} 2C - M_1\omega^2 & -2C\sin\left(qa_0/2\right) \\ -2C\sin\left(qa_0/2\right) & 2C - M_2\omega^2 \end{vmatrix} = 0.$$

The frequency eigenvalues are

$$\omega^2 = CM \pm C\sqrt{M^2 - \frac{4\sin^2\left(qa_0/2\right)}{M_1 M_2}},$$

where $M = 1/M_1 + 1/M_2$. Figure A.2 shows a plot of ω as a function of q. The lower branch corresponds to the acoustic mode where $\omega \to 0$ as $q \to 0$. The upper branch is

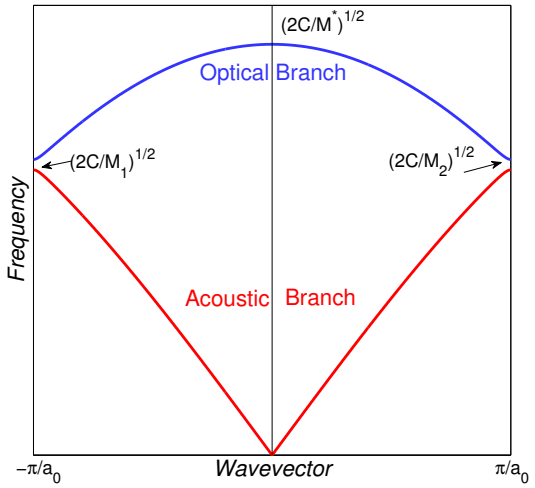

Figure A.2: Phonon dispersion of 1D diatomic chain.

associated with the optical mode which has a vanishing group velocity at $q = 0$. Near $q = 0$, the acoustic branch has a linear dispersion while the optical branch is quadratic.

In a three dimensional lattice where the unit cell contains two atoms (e.g. GaAs), vibrations can occur in three ways. In the first two, the atoms in one plane (e.g. a plane of Ga atoms) can slide past a neighboring plane (e.g. a plane of As atoms) along either of the two axes parallel to the planes. In this case, the spacing between the two planes remains constant. These are the transverse vibrations. The planes can also move in the direction orthogonal to them such that their spacing increases and decreases. This is the longitudinal vibration. Thus, three dimensional lattice vibrations can then take on 3 polarizations, two transverse and one longitudinal. A crystal with 2 atoms per unit cell and N unit cells has $6N$ total modes: $1N$ longitudinal acoustic (LA), $2N$ transverse acoustic (TA), $2N$ transverse optical (TO), and $1N$ longitudinal optical (LO) vibrations.

A.2 Phonons

The normal modes of these lattice vibrations can be quantized into Bosonic quasiparticles known as phonons. First, the quantum mechanical form of the Hamiltonian for a system of

lattice vibrations is given by

$$H = \sum_{\mathbf{q},\lambda} \left[\frac{1}{2M} \hat{p}_{\mathbf{q},\lambda} \hat{p}_{-\mathbf{q},\lambda} + \frac{M\omega_\lambda^2(\mathbf{q})}{2} \hat{u}_{\mathbf{q},\lambda} \hat{u}_{-\mathbf{q},\lambda} \right]$$

where $\mathbf{q}$ and λ are the wavevector and band-index of the phonon mode, $\hat{p}_{\mathbf{q},\lambda}$ is the momentum operator, and $\hat{u}_{\mathbf{q},\lambda}$ is the coordinate operator. In second quantization, we can use creation and annihilation operators to write $\hat{p}_{\mathbf{q},\lambda}$ and $\hat{u}_{\mathbf{q},\lambda}$ as

$$\begin{aligned} \hat{u}_{\mathbf{q},\lambda} &= \sqrt{\frac{\hbar}{2M\omega_{\mathbf{q},\lambda}}} \left[\hat{a}_{\mathbf{q},\lambda} + \hat{a}^\dagger_{-\mathbf{q},\lambda} \right] \\ \hat{p}_{\mathbf{q},\lambda} &= i \sqrt{\frac{M\hbar\omega_{\mathbf{q},\lambda}}{2}} \left[\hat{a}_{\mathbf{q},\lambda} - \hat{a}^\dagger_{-\mathbf{q},\lambda} \right], \end{aligned}$$

where the ladder operators obey the commutation relations

$$\begin{aligned} \left[\hat{a}_{\mathbf{q},\lambda}, \hat{a}^\dagger_{\mathbf{q}',\lambda'} \right] &= \delta_{\mathbf{q},\mathbf{q}'} \delta_{\lambda,\lambda'} \\ [\hat{a}_{\mathbf{q},\lambda}, \hat{a}_{\mathbf{q}',\lambda'}] &= \left[\hat{a}^\dagger_{\mathbf{q},\lambda}, \hat{a}^\dagger_{\mathbf{q}',\lambda'} \right] = 0. \end{aligned}$$

Physically, we can interpret the creation operator as being responsible for creating a phonon of band-index λ with wavevector $\mathbf{q}$; the corresponding annihilation operator destroys a phonon in this state. We can define a number operator $\hat{n}_{\mathbf{q},\lambda} = \hat{a}^\dagger_{\mathbf{q},\lambda} \hat{a}_{\mathbf{q},\lambda}$ that counts the number of phonons with wavevector $\mathbf{q}$ in the band λ, and in the notation of second quantization, an arbitrary state of the system is written as

$$\left| n_{\mathbf{q}_1,\lambda_1}, n_{\mathbf{q}_2,\lambda_2}, n_{\mathbf{q}_2,\lambda_2}, \dots \right\rangle,$$

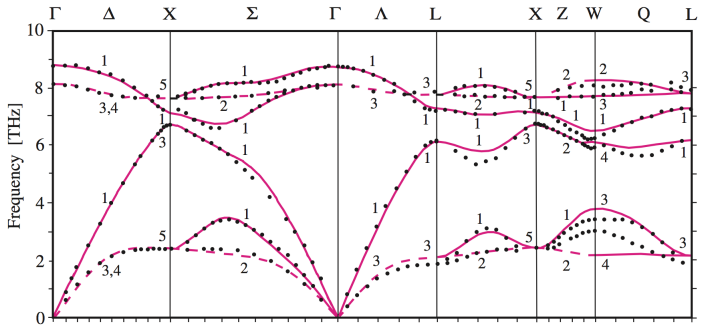

Figure A.3: Phonon dispersion in GaAs along the high-symmetry directions in the Brillouin zone, reproduced from [48, 88].

where $n_{\mathbf{q}_1,\lambda_1}$ is the number of phonons with $\mathbf{q} = \mathbf{q}_1$ and $\lambda = \lambda_1$. The ladder operators operate on this state as

$$\begin{aligned} \hat{a}_{\mathbf{q},\lambda} \left| \ldots, n_{\mathbf{q},\lambda}, \ldots \right\rangle &= \sqrt{n_{\mathbf{q},\lambda}} \left| \ldots, n_{\mathbf{q},\lambda} - 1, \ldots \right\rangle \\ \hat{a}^{\dagger}_{\mathbf{q},\lambda} \left| \ldots, n_{\mathbf{q},\lambda}, \ldots \right\rangle &= \sqrt{n_{\mathbf{q},\lambda} + 1} \left| \ldots, n_{\mathbf{q},\lambda} + 1, \ldots \right\rangle . \end{aligned}$$

Finally, we can re-write the Hamiltonian in second quantization as

$$H = \sum_{\mathbf{q},\lambda} \hbar\omega_{\mathbf{q},\lambda} \left[\hat{n}_{\mathbf{q},\lambda} + \frac{1}{2} \right],$$

where $\hbar\omega_{\mathbf{q},\lambda}$ is the energy of the phonon with $\mathbf{q}$ in λ. The utility of second quantization lies in the fact that it allows us to deal with interaction with light more easily once we quantize the electromagnetic field.

The number of bands and their dispersion are dependent upon the symmetry of the crystal. As GaAs is a semiconductor with two atoms per unit cell, in 3-dimensions, we have $3 \times 2 = 6$ phonon modes: 2 TO, 2 TA, 1 LO, and 1 LA. Figure A.3 shows the phonon dispersion in GaAs. Both the TA and LA phonons demonstrate the expected acoustic behavior since their frequencies vanish at the Γ point where $\mathbf{q} = 0$. Acoustic phonons are associated with sound waves in a crystal, TA phonons corresponding to shear sound and LA phonons to compressive sound. The LA phonon generally has a larger group velocity than

the TA phonon, reflecting the fact that the shear modulus is smaller than the bulk modulus in GaAs. The TO and LO phonons both have higher energies than the acoustic modes and have a nearly flat dispersion at the Γ point. In the long wavelength (small q) regime, the LO phonon has a higher frequency than the TO mode. This is due to the fact the LO phonon carries with it an electric field that introduces an additional restoring force to the vibration.

APPENDIX B

Code

B.1 spectrasim.m

```
% NAME: spectrasim.m

% PURPOSE: This code generates dynamic Xe, Xhh, Xlh, and Xinter using
% either a parabolic band, anisotropic parabolic band, or interpolated
% band structure (calculated using a 30-band kp method with kp30GaAs2.m

% NOTE: Run kp30GaAs2.m prior to running this script
% NOTE: Parallel computing toolbox required is using multiple cores

% Open Parallel workers ***************************************************
myCluster = parcluster('local');
myCluster.NumWorkers = 3;

if matlabpool('size')==0
    matlabpool open 3
end
% *************************************************************************


% Define band structures **************************************************
% Electron band structure
K = [-k100(end:-1:2) k100(1:end)];
E = [E_00(9,end:-1:2)-E_00(9,1) E100(9,1:end)-E100(9,1)];

% LH band structure
K2 = [-k100(end:-1:2) k100(1:end)];
E2 = -[E_00(5,end:-1:2) E100(5,1:end)];
% *************************************************************************


% Define Numerical parameters *********************************************
% d = active layer thickness
% Q = acoustic plasmon wavevector points
% w = frequency
% Efac = possible factors to multiple with an energy to give the Fermi E
% n = reference number to set energy to be multipled by Efac
% Ts = carrier temeprature
% eta = carrier damping
% KF = upperlimit for wavevector integration
% Efacee = the electron Efac factors
% Efachh = the HH and LH Efac factors
d = 6e-5;
Q = (pi/d)*(1:20); %Q = [1e4 Q];
%Q = 4*pi*3.76/(6.47e-5);
w = 2*pi*3e10*(2.5:0.5:150);
Efac = -3:0.0025:2; %-4:0.0025:1; %-3:0.0025:2; %-2:0.0025:1; %-2:0.0025:1;
n = 2e19;
Ts = 400;
eta = 9e12;
%Efac(1843);
%Efac(627);

% for i = 1:40
%     temp = abs(Ne-1e18-(i-1)*1e18);
%     [ee_idx(i) ee_idx(i)] = min(temp);
% end
% for i = 1:40
%     temp = abs(Nh-1e18-(i-1)*1e18);
%     [hh_idx(i) hh_idx(i)] = min(temp);
% end
% Efacee = Efac(ee_idx);
% Efachh = Efac(hh_idx);

KF = (3*pi^2*4e19).^(1/3);
% *************************************************************************


% Constants and values based on parameters ********************************
m0 = 9.11e-28;
me = 0.067*m0;
mhh = 0.47*m0;
mlh = 0.082*m0;
eps_inf = 10.89;
e_c = 4.803e-10;
hb = 1.05e-27;
kb = 1.38e-16;
kFe = (3*pi^2*n).^(1/3);
EFe = hb^2*kFe.^2/(2*me);
EFhh = hb^2*kFe.^2/(2*mhh);
% *************************************************************************


```

```
%Preallocate loop variables (commented out after first run) ***************
Qe_0 = zeros(length(Efacee),length(Q));
Qe = zeros(length(w),length(Efacee),length(Q));
Qe_LM = zeros(length(w),length(Efacee),length(Q));
eps = zeros(length(w),length(Efacee),length(Q));
T11 = zeros(length(w),length(Efacee),length(Q));
Ne = zeros(length(Efacee),length(Q));
Qhh_0 = zeros(length(Efacee),length(Q));
Qhh = zeros(length(w),length(Efacee),length(Q));
Qhh_LM = zeros(length(w),length(Efacee),length(Q));
Nhh = zeros(length(Efacee),length(Q));
Qlh_0 = zeros(length(Efacee),length(Q));
Qlh = zeros(length(w),length(Efacee),length(Q));
Qlh_LM = zeros(length(w),length(Efacee),length(Q));
Nlh = zeros(length(Efacee),length(Q));
Qinter_0 = zeros(length(Efacee),length(Q));
Qinter = zeros(length(w),length(Efacee),length(Q));
Qinter_LM = zeros(length(w),length(Efacee),length(Q));
QSPE_0 = zeros(length(Efacee),length(Q));
QSPE = zeros(length(w),length(Efacee),length(Q));
QSPE_LM = zeros(length(w),length(Efacee),length(Q));
speed_check = zeros(length(w),1);
% ************************************************************************


% % Generates N vs. Fermi energy for e, hh, lh (commented out by default) *
% W = length(Efac);
% kFe_current = KF(1);
% parfor_progress(W);
% parfor i = 1:length(Efac)
%
%         % Use this code for complex band structure (e = interpolation..., hh =↙
warped, lh = warped
%         Ne(i) = 2*pi*integral2(@(k,theta)density(k,q,w(1),eta,theta,0,EFe*Efac(i),↙
Ts,K,E,1),0,4*kFe_current,0,pi);
%         Nhh(i) = integral3(@(k,theta,phi)density(k,q,w(1),eta,theta,phi,EFhh*Efac↙
(i),Ts,K,E,2),0,4*kFe_current,0,pi,0,2*pi);
%         Nlh(i) = integral3(@(k,theta,phi)density(k,q,w(1),eta,theta,phi,EFhh*Efac↙
(i),Ts,K,E,3),0,4*kFe_current,0,pi,0,2*pi);
%
%         % Use this code for effective mass band structure
%         %Ne(i) = 2*pi*integral2(@(k,theta)density(k,q,w(1),eta,theta,0,EFe*Efac↙
(i),Ts,K,E,4),0,4*kFe_current,0,pi);
%         %Nhh(i) = 2*pi*integral2(@(k,theta)density(k,q,w(1),eta,theta,0,EFhh*Efac↙
(i),Ts,K,E,5),0,4*kFe_current,0,pi);
%         %Nlh(i) = 2*pi*integral2(@(k,theta)density(k,q,w(1),eta,theta,0,EFhh*Efac↙
(i),Ts,K,E,6),0,4*kFe_current,0,pi);
%         parfor_progress;
% end
% parfor_progress(0);
% ************************************************************************


% Lattice susceptibility (T=0) ***********************************************
wlo = 2*pi*3e10*295;
wto = 2*pi*3e10*272;
QL = (eps_inf/(4*pi))*(wlo^2 - wto^2)./(wto^2 - w.^2 - 1i*2*pi*3e10*5*w);
% ************************************************************************


% Main loop to calcualte susceptibilties, eps, and T11 *******************
for qi=1:length(Q)
% Main loop that calculates susceptibilities for all n in range and mode index qi
    q = Q(qi);
    T_current = Ts(1);
    for j = 1:length(Efacee)
            EFe_current = EFe*Efacee(j);
            EFhh_current = EFhh*Efachh(j);
            kFe_current = KF(1);

            % Compute carr density (complex band structure)
            Ne(j,qi) = 2*pi*integral2(@(k,theta)density(k,q,w(1),eta,theta,0,↙
EFe_current,T_current,K,E,1),0,4*kFe_current,0,pi)
            Nhh(j,qi) = integral3(@(k,theta,phi)density(k,q,w(1),eta,theta,phi,↙
EFhh_current,T_current,K,E,2),0,4*kFe_current,0,pi,0,2*pi);
            Nlh(j,qi) = integral3(@(k,theta,phi)density(k,q,w(1),eta,theta,phi,↙
EFhh_current,T_current,K,E,3),0,4*kFe_current,0,pi,0,2*pi);
            Nh = Nhh(j,qi) + Nlh(j,qi)

            % Compute carr density (simple parabolic bands)
            %Ne(j,qi) = 2*pi*integral2(@(k,theta)density(k,q,w(1),eta,theta,0,↙
EFe_current,T_current,K,E,4),0,4*kFe_current,0,pi)
```

```
154             %Nhh(j,qi) = 2*pi*integral2(@(k,theta)density(k,q,w(1),eta,theta,0,↙
EFhh_current,T_current,K,E,5),0,4*kFe_current,0,pi)
155             %Nlh(j,qi) = 2*pi*integral2(@(k,theta)density(k,q,w(1),eta,theta,0,↙
EFhh_current,T_current,K,E,6),0,4*kFe_current,0,pi)
156             %Nh = Nhh(j,qi) + Nlh(j,qi)
157
158             tstart1 = tic;
159
160             % Compute 0 frequency susceptibilities (complex bands)
161             Qe_0_current = 2*pi*integral2(@(k,theta)suscep(k,q,0,0,theta,0,↙
EFe_current,T_current,K,E,K2,E2,1),0,4*kFe_current,0,pi);
162             Qhh_0_current = integral3(@(k,theta,phi)suscep(k,q,0,0,theta,phi,↙
EFhh_current,T_current,K,E,K2,E2,4),0,4*kFe_current,0,pi,0,2*pi);
163             Qlh_0_current = 2*pi*integral2(@(k,theta)suscep(k,q,0,0,theta,0,↙
EFhh_current,T_current,K,E,K2,E2,9),0,4*kFe_current,0,pi);
164             Qinter_0_current = 2*pi*integral2(@(k,theta)suscep(k,q,0,0,theta,0,↙
EFhh_current,T_current,K,E,K2,E2,10),0,4*kFe_current,0,pi);
165
166             % Compute 0 frequency susceptibilities (simple parabolic bands)
167             % Use this code for simple effective mass band structure
168             %Qe_0_current = integral(@(k)suscep(k,q,0,0,0,0,EFe_current,T_current,K,↙
E,K2,E2,2),0,4*kFe_current);
169             %Qhh_0_current = integral(@(k)suscep(k,q,0,0,0,0,EFhh_current,T_current,↙
K,E,K2,E2,5),0,4*kFe_current);
170             %Qlh_0_current = integral(@(k)suscep(k,q,0,0,0,0,EFhh_current,T_current,↙
K,E,K2,E2,8),0,4*kFe_current);
171             %Qinter_0_current = 1;
172
173             parfor_progress(length(w));
174             parfor i = 1:length(w)
175
176                 ts = tic;
177
178                 % Compute susceptibilities (complex bands)
179                 Qe_current(i) = 2*pi*integral2(@(k,theta)suscep(k,q,w(i),eta,theta,↙
0,EFe_current,T_current,K,E,K2,E2,1),0,4*kFe_current,0,pi);
180                 Qhh_current(i) = integral3(@(k,theta,phi)suscep(k,q,w(i),eta,theta,↙
phi,EFhh_current,T_current,K,E,K2,E2,4),0,4*kFe_current,0,pi,0,2*pi);
181                 Qlh_current(i) = 2*pi*integral2(@(k,theta)suscep(k,q,w(i),eta,theta,↙
0,EFhh_current,T_current,K,E,K2,E2,9),0,4*kFe_current,0,pi);
182                 Qinter_current(i) = integral3(@(k,theta,phi)suscep(k,q,w(i),eta,↙
theta,phi,EFhh_current,T_current,K,E,K2,E2,10),0,4*kFe_current,0,pi,0,2*pi);
183
184                 % Compute susceptibilities (simple parabolic bands)
185                 %Qe_current(i) = integral(@(k)suscep(k,q,w(i),eta,0,0,EFe_current,↙
T_current,K,E,K2,E2,2),0,4*kFe_current);
186                 %Qhh_current(i) = integral(@(k)suscep(k,q,w(i),eta,0,0,EFhh_current,↙
T_current,K,E,K2,E2,5),0,4*kFe_current);
187                 %Qlh_current(i) = integral(@(k)suscep(k,q,w(i),eta,0,0,EFhh_current,↙
T_current,K,E,K2,E2,8),0,4*kFe_current);
188                 %Qinter_current(i) = 2*pi*integral2(@(k,theta)suscep(k,q,w(i),eta,↙
theta,0,EFhh_current,T_current,K,E,K2,E2,10),0,4*kFe_current,0,pi);
189
190                 timer1 = toc(ts);
191                 speed_check(i) = timer1;
192                 parfor_progress;
193
194             end
195             parfor_progress(0);
196             toc(tstart1)
197
198             % Calculate Lindhard-Mermin suceptibilities
199             Qe_LM_current = ((1+1i*eta(1)./w).*Qe_current)./(1+(1i*eta(1)./w).*↙
(Qe_current/Qe_0_current));
200             Qhh_LM_current = ((1+1i*eta(1)./w).*Qhh_current)./(1+(1i*eta(1)./w).*↙
(Qhh_current/Qhh_0_current));
201             Qlh_LM_current = ((1+1i*eta(1)./w).*Qlh_current)./(1+(1i*eta(1)./w).*↙
(Qlh_current/Qlh_0_current));
202             Qinter_LM_current = ((1+1i*eta(1)./w).*Qinter_current)./(1+(1i*eta(1).↙
/w).*(Qinter_current/Qinter_0_current));
203             eps_current = eps_inf + 4*pi*Qe_LM_current + 4*pi*Qhh_LM_current +↙
4*pi*Qlh_LM_current + 4*pi*Qinter_LM_current + 4*pi*QL;
204             T11_current = Qe_LM_current - 4*pi*(Qe_LM_current.^2)./eps_current;
205
206             % Save all computations to variables
207             Qe_0(j,qi) = Qe_0_current;
208             Qe(:,j,qi) = Qe_current;
209             Qe_LM(:,j,qi) = Qe_LM_current;
210             Qhh_0(j,qi) = Qhh_0_current;
211             Qhh(:,j,qi) = Qhh_current;
212             Qhh_LM(:,j,qi) = Qhh_LM_current;
213             Qlh_0(j,qi) = Qlh_0_current;
```

```
214             Qlh(:,j,qi) = Qlh_current;
215             Qlh_LM(:,j,qi) = Qlh_LM_current;
216             Qinter_0(j,qi) = Qinter_0_current;
217             Qinter(:,j,qi) = Qinter_current;
218             Qinter_LM(:,j,qi) = Qinter_LM_current;
219             QSPE_LM(:,j,qi) = QSPE_LM_current;
220             eps(:,j,qi) = eps_current;
221             T11(:,j,qi) = T11_current;
222     end
223 end
224 matlabpool close
225 % ************************************************************************
226
227
228 W = w/(2*pi*3e10); % Frequency in wavenumbers
229 Np12 = (1./(1-exp(-hb*abs(2*pi*3e10*W)/(kb*Ts)))-1+1*(W>0)); % Bose factor
```

B.2 suscep.m

```
% NAME: suscep.m

% PURPOSE: This is a helper function for spectrasim.m. It controls the
% integrand for the susceptibility integrals using various models
% (effective mass, interpolation, aniso).

% NOTE: In all simulations, q is assumed to be in the [001] direction.

function z = suscep(k,q,w,eta,theta,phi,mu,T,kdir,Ek,kdir2,Ek2,sw)


% Constants
hb = 1.05e-27;
kb = 1.38e-16;
wc = w + 1i*eta;
m0 = 9.11e-28;
me = 0.067*9.11e-28;
mhh = 0.47*m0;
mlh = 0.082*m0;
e_c = 4.803e-10;
vd = 0;


% Warped band structure parameters
A = -7.98;
B = -5.16;
C = 6.56;


if sw == 1
    % Conduction band using kp and linear interpolation (2D inegral)
    E_k = interp1(kdir,Ek,k,'spline');
    E_kpq = interp1(kdir,Ek,sqrt(k.^2 + q.^2 + 2*k.*q.*cos(theta)),'spline');
    f_k = 1./(exp(E_k/(kb*T)).*exp(-mu/(kb*T))+1);
    f_kpq = 1./(exp(E_kpq/(kb*T)).*exp(-mu/(kb*T))+1);
    z = -(1*e_c^2./(pi^2*q.^2)).*((f_k - f_kpq)./(-E_kpq + E_k + hb*wc)).*k.^2.*sin(theta)/(4*pi);
elseif sw == 2
    % Conduction band using effective mass approx (1D integral)
    A1 = 2*hb^2*q*k/me + hb^2*q^2/me - 2*hb*wc;
    B1 = -2*hb^2*q*k/me + hb^2*q^2/me - 2*hb*wc;
    A2 = -2*hb^2*q*k/me + hb^2*q^2/me + 2*hb*wc;
    B2 = 2*hb^2*q*k/me + hb^2*q^2/me + 2*hb*wc;
    f = 1./(exp(((hb^2*((k-me*vd/hb).^2)/(2*me))-mu)/(kb*T))+1);
    z = (2*e_c^2*me/(pi*hb^2*q^3))*k.*f.*(log(A1./B1) - log(A2./B2));
elseif sw == 3
    % Conduction band using effective mass approx (2D integral)
    E_k = hb^2*k.^2/(2*me);
    E_kpq = hb^2.*(k.^2 + q.^2 + 2*k.*q.*cos(theta))/(2*me);
    E_kmq = hb^2.*(k.^2 + q.^2 - 2*k.*q.*cos(theta))/(2*me);
    f_k = 1./(exp(E_k/(kb*T)).*exp(-mu/(kb*T))+1);
    z = (1*e_c^2./(pi^2*q.^2)).*f_k.*(1./(E_kpq - E_k - hb*wc)+1./(E_kmq - E_k + hb*wc)).*k.^2.*sin(theta);
elseif sw == 4
    % HH band using effective approx including aniso (3D integral)
    g = sqrt((B/A)^2 + (C/A)^2*(sin(theta).^2.*cos(theta).^2+sin(theta).^4.*cos(phi).^2.*sin(phi).^2));
    E_kpq = (abs(A)*hb^2./(2*m0)).*(1-g).*(k.^2+q.^2+2.*k.*q.*cos(theta));
    E_k = abs(A)*hb^2./(2*m0).*(1-g).*(k.^2);
    f_k = 1./(exp(E_k/(kb*T)).*exp(-mu/(kb*T))+1);
    f_kpq = 1./(exp(E_kpq/(kb*T)).*exp(-mu/(kb*T))+1);
    M11 = (1/4)*(1+(3*(k.^2+q*k.*cos(theta)).^2)./((k.^2).*(k.^2+q.^2+2.*k.*q.*cos(theta))));
    z = (1*e_c^2./(pi^2*q.^2)).*M11.*((f_k - f_kpq)./(E_kpq - E_k - hb*wc)).*k.^2.*sin(theta)/(4*pi);
elseif sw == 5
    % HH band using effective mass approx (1D integral)
    A1 = 2*hb^2*q*k/mhh + hb^2*q^2/mhh - 2*hb*wc;
    B1 = -2*hb^2*q*k/mhh + hb^2*q^2/mhh - 2*hb*wc;
    A2 = -2*hb^2*q*k/mhh + hb^2*q^2/mhh + 2*hb*wc;
    B2 = 2*hb^2*q*k/mhh + hb^2*q^2/mhh + 2*hb*wc;
    f = 1./(exp(((hb^2*(k.^2)/(2*mhh))-mu)/(kb*T))+1);
    z = (2*e_c^2*mhh/(pi*hb^2*q^3))*k.*f.*(log(A1./B1) - log(A2./B2));
elseif sw == 6
    % HH band using kp and linear interpolation (3D inegral)
    E_k = interp2(kt,thetat,Emesh(:,:,1),k,theta,'spline');
    E_kpq = interp2(kt,thetat,Emesh(:,:,1),sqrt(k.^2 + q.^2 + 2*k.*q.*cos(theta)),theta,'spline');
    E_kmq = interp2(kt,thetat,Emesh(:,:,1),sqrt(k.^2 + q.^2 - 2*k.*q.*cos(theta)),theta,'spline');
    f_k = 1./(exp(E_k/(kb*T)).*exp(-mu/(kb*T))+1);
    z = (1*e_c^2./(pi^2*q.^2)).*f_k.*(1./(E_kpq - E_k - hb*wc)+1./(E_kmq - E_k +
```

```
hb*wc)).*k.^2.*sin(theta);
 76 elseif sw == 7
 77     % LH band using effective approx including aniso (3D integral)
 78     g = sqrt((B/A)^2 + (C/A)^2*(sin(theta).^2.*cos(theta).^2+sin(theta).^4.*cos↙
(phi).^2.*sin(phi).^2));
 79     E_kpq = (abs(A)*hb^2./(2*m0)).*(1+g).*(k.^2+q.^2+2.*k.*q.*sin(theta).*cos(phi));
 80     E_kmq = (abs(A)*hb^2./(2*m0)).*(1+g).*(k.^2+q.^2-2.*k.*q.*sin(theta).*cos(phi));
 81     E_k = abs(A)*hb^2./(2*m0).*(1+g).*(k.^2);
 82     f_k = 1./(exp(E_k/(kb*T)).*exp(-mu/(kb*T))+1);
 83     z = (1*e_c^2./(pi^2*q.^2)).*f_k.*(1./(E_kpq - E_k - hb*wc)+1./(E_kmq - E_k +↙
hb*wc)).*k.^2.*sin(theta);
 84  elseif sw == 8
 85     % LH band using effective mass approx (1D integral)
 86     A1 = 2*hb^2*q*k/mlh + hb^2*q^2/mlh - 2*hb*wc;
 87     B1 = -2*hb^2*q*k/mlh + hb^2*q^2/mlh - 2*hb*wc;
 88     A2 = -2*hb^2*q*k/mlh + hb^2*q^2/mlh + 2*hb*wc;
 89     B2 = 2*hb^2*q*k/mlh + hb^2*q^2/mlh + 2*hb*wc;
 90     f = 1./(exp(((hb^2*(k.^2)/(2*mlh))-mu)/(kb*T))+1);
 91     z = (2*e_c^2*mlh/(pi*hb^2*q^3))*k.*f.*(log(A1./B1) - log(A2./B2));
 92  elseif sw == 9
 93     % LH band using kp and linear interpolation (2D inegral)
 94     E_k = interp1(kdir2,Ek2,k,'spline');
 95     E_kpq = interp1(kdir2,Ek2,sqrt(k.^2 + q.^2 + 2*k.*q.*cos(theta)),'spline');
 96     f_k = 1./(exp(E_k/(kb*T)).*exp(-mu/(kb*T))+1);
 97     f_kpq = 1./(exp(E_kpq/(kb*T)).*exp(-mu/(kb*T))+1);
 98     M11 = (1/4)*(1+(3*(k.^2+q*k.*cos(theta)).^2)./((k.^2).*(k.^2+q.^2+2.*k.*q.*cos↙
(theta))));
 99     z = (1*e_c^2./(pi^2*q.^2)).*M11.*((f_k - f_kpq)./(E_kpq - E_k - hb*wc)).*k.^2.↙
*sin(theta)/(4*pi);
100 elseif sw == 10
101     % Interband transitions using effective mass approx including aniso
102     g = sqrt((B/A)^2 + (C/A)^2*(sin(theta).^2.*cos(theta).^2+sin(theta).^4.*cos↙
(phi).^2.*sin(phi).^2));
103     E_1 = (abs(A)*hb^2./(2*m0)).*(1+g).*(k.^2);
104     E_2 = (abs(A)*hb^2./(2*m0)).*(1-g).*(k.^2+q.^2+2.*k.*q.*cos(theta));
105     f_k_1 = 1./(exp(E_1/(kb*T)).*exp(-mu/(kb*T))+1);
106     f_k_2 = 1./(exp(E_2/(kb*T)).*exp(-mu/(kb*T))+1);
107     M12 = (3/4)*(1-((k.^2+q*k.*cos(theta)).^2)./((k.^2).*(k.^2+q.^2+2.*k.*q.*cos↙
(theta))));
108     z = (1*e_c^2./(2*pi^2*q.^2)).*M12.*((f_k_1 - f_k_2)./(E_2 - E_1 + hb*wc)+(f_k_1↙
- f_k_2)./(E_2 - E_1 - hb*wc)).*k.^2.*sin(theta)/(4*pi);
109 end
```

B.3 density.m

```
% NAME: density.m

% PURPOSE: This is a helper function for spectrasim.m. It computes the
% carrier density using various models for the bands.

function z = density(k,q,w,eta,theta,phi,mu,T,kdir,Ek,sw)

hb = 1.05e-27;
kb = 1.38e-16;
A = -7.98;
B = -5.16;
C = 6.56;
me = 0.067*9.11e-28;
mhh = 0.47*9.11e-28;
mlh = 0.082*9.11e-28;

if sw == 1
    % Electron density using linear interpolation
    E_k = spline(kdir,Ek,k);
    f_k = 1./(exp(E_k/(kb*T)).*exp(-mu/(kb*T))+1);
    z = 2/(8*pi^3)*f_k.*k.^2.*sin(theta);
elseif sw == 2
    % HH density using anisotropic effective mass approximation
    g = sqrt((B/A)^2 + (C/A)^2*(sin(theta).^2.*cos(theta).^2+sin(theta).^4.*cos(phi).^2.*sin(phi).^2));
    E_k = abs(A)*hb^2./(2*9.11e-28).*(1-g).*(k.^2);
    f_k = 1./(exp(E_k/(kb*T)).*exp(-mu/(kb*T))+1);
    z = 2/(8*pi^3)*f_k.*k.^2.*sin(theta);
elseif sw == 3
    % LH density using anisotropic effective mass approximation
    g = sqrt((B/A)^2 + (C/A)^2*(sin(theta).^2.*cos(theta).^2+sin(theta).^4.*cos(phi).^2.*sin(phi).^2));
    E_k = abs(A)*hb^2./(2*9.11e-28).*(1+g).*(k.^2);
    f_k = 1./(exp(E_k/(kb*T)).*exp(-mu/(kb*T))+1);
    z = 2/(8*pi^3)*f_k.*k.^2.*sin(theta);
elseif sw == 4
    % Electron density using effective mass approximation
    E_k = hb^2*k.^2/(2*me);
    f_k = 1./(exp(E_k/(kb*T)).*exp(-mu/(kb*T))+1);
    z = 2/(8*pi^3)*f_k.*k.^2.*sin(theta);
elseif sw == 5
    % HH density using effective mass approximation
    E_k = hb^2*k.^2/(2*mhh);
    f_k = 1./(exp(E_k/(kb*T)).*exp(-mu/(kb*T))+1);
    z = 2/(8*pi^3)*f_k.*k.^2.*sin(theta);
elseif sw == 6
    % LH density using effective mass approximation
    E_k = hb^2*k.^2/(2*mlh);
    f_k = 1./(exp(E_k/(kb*T)).*exp(-mu/(kb*T))+1);
    z = 2/(8*pi^3)*f_k.*k.^2.*sin(theta);
end
```

B.4 kp30GaAs2.m

```
% NAME: kp30GaAs2.m

% PURPOSE: Computes band structure of GaAs using 30 band direct
% diagonalization along [1 1 1], [-1 -1 -1], [1 0 0], and [-1 0 0]

% References: Richard, PRB, 70 (23), 235204 (2004)

clear;

% Constants
m0 = 9.11e-28;  %electron mass/(c^2)
hb = 1.05e-27;


% Gamma-point energy levels in GaAs (eV)
Eq = 13.64*1.6e-12;
E8d = 11.89*1.6e-12;
E7d = 11.89*1.6e-12;
E3 = 10.17*1.6e-12;
Eu = 8.56*1.6e-12;
E8C = 4.569*1.6e-12;
E7C = 4.488*1.6e-12;
E6 = 1.519*1.6e-12;
E8 = 0*1.6e-12;
E7 = -0.341*1.6e-12;
E6v = -12.55*1.6e-12;


% Gamma-point momentum matrix elements
Ep = 22.37*1.6e-12;
EPX = 16.79*1.6e-12;
EP3 = 4.916*1.6e-12;
EP2 = 6.280*1.6e-12;
EPS = 2.434*1.6e-12;
EP_prime = 0.0656*1.6e-12;
EPd = 0.010*1.6e-12;
EPXd = 4.344*1.6e-12;
EP3d = 8.888*1.6e-12;
EP2d = 23.15*1.6e-12;
EPU = 19.63*1.6e-12;
Ed_prime = 0;

P = sqrt((hb^2/(2*m0))*Ep);
PX = sqrt((hb^2/(2*m0))*EPX);
P3 = sqrt((hb^2/(2*m0))*EP3);
P2 = sqrt((hb^2/(2*m0))*EP2);
PS = sqrt((hb^2/(2*m0))*EPS);
P_prime = sqrt((hb^2/(2*m0))*EP_prime);
Pd = sqrt((hb^2/(2*m0))*EPd);
PXd = sqrt((hb^2/(2*m0))*EPXd);
P3d = sqrt((hb^2/(2*m0))*EP3d);
P2d = sqrt((hb^2/(2*m0))*EP2d);
PU = sqrt((hb^2/(2*m0))*EPU);
d_prime = sqrt((hb^2/(2*m0))*Ed_prime);


% k-vectors
a = 5.65e-8;
kx = 0:1e4:2*pi/a;
ky = 0:1e4:2*pi/a;
kkz = 0:1e4:2*pi/a;


Hdiag = diag([Eq,Eq,E8d,E8d,E8d,E8d,E7d,E7d,E3,E3,E3,E3,Eu,Eu,E8C,E8C,E8C,E8C,E7C,↙
E7C,E6,E6,E8,E8,E8,E8,E7,E7,E6v,E6v]);
Hoffdiag = zeros(30,30);

%dirs100 = {'100' '_00' '010' '0_0' '001' '00_'};
%dirs110 = {'110' '_10' '1_0' '__0' '101' '_01' '10_' '_0_' '011' '0_1' '01_'↙
'0__'};
%dirs111 = {'111' '_11' '1_1' '11_' '__1' '_1_' '1__' '___'};

dirs100 = {'100'};
dirs110 = {'_00'};
dirs111 = {'111' '___'};

dirs = [dirs100 dirs110 dirs111];

q = 5.25e5; % in [100 direction]

for runs = 1:length(dirs)

```

```
 81      curr = dirs{runs}
 82
 83      if strcmp(curr(1),'0')
 84          kx = 0*(0:1e4:2*pi/a);
 85          x_index = '1';
 86      elseif strcmp(curr(1),'1')
 87          kx = (0:1e4:2*pi/a);
 88          x_index = 'i';
 89      elseif strcmp(curr(1),'_')
 90          kx = -((0:1e4:2*pi/a));
 91          x_index = 'i';
 92      end
 93
 94
 95      if strcmp(curr(2),'0')
 96          ky = 0*(0:1e4:2*pi/a);
 97          y_index = '1';
 98      elseif strcmp(curr(2),'1')
 99          ky = (0:1e4:2*pi/a);
100          y_index = 'i';
101      elseif strcmp(curr(2),'_')
102          ky = -(0:1e4:2*pi/a);
103          y_index = 'i';
104      end
105
106
107      if strcmp(curr(3),'0')
108          kkz_string = 'kkz = 0*(0:1e4:2*pi/a);';
109          kkz = 0*(0:1e4:2*pi/a);
110          z_index = '1';
111      elseif strcmp(curr(3),'1')
112          kkz_string = 'kkz = (0:1e4:2*pi/a);';
113          kkz = (0:1e4:2*pi/a);
114          z_index = 'i';
115      elseif strcmp(curr(3),'_')
116          kkz_string = 'kkz = -(2*pi/a:-1e4:0);';
117          kkz = -(0:1e4:2*pi/a);
118          z_index = 'i';
119      end
120
121
122      eval(['k',curr,' = sqrt(kx.^2+ky.^2+kkz.^2);']);
123      eval(['K = k',curr,';']);
124
125      for i = 1:length(K)
126          Hoffdiag=Hoffdiag*0;
127
128          eval(['kplus = kx(',x_index,') + 1i*ky(',y_index,');']);
129          eval(['kminus = kx(',x_index,') - 1i*ky(',y_index,');']);
130
131          eval(['kz = kkz(',z_index,');']);
132          eval(['Ek = (hb^2/(2*m0))*(kx(',x_index,')^2+ky(',y_index,')^2+kkz(',↙
z_index,')^2);']);
133
134          HEkdiag = diag([Ek,Ek,Ek,Ek,Ek,Ek,Ek,Ek,Ek,Ek,Ek,Ek,Ek,Ek,Ek,Ek,Ek,Ek,Ek,Ek,↙
Ek,Ek,Ek,Ek,Ek,Ek,Ek,Ek,Ek,Ek]);
135
136          Hoffdiag(1,2:end) = [0,-P2d*kplus/sqrt(2),P2d*kz*sqrt(2/3),P2d*kminus/sqrt↙
(6),0,P2d*kz/sqrt(3),P2d*kminus/sqrt(3),0,0,0,0,0,0,0,0,0,0,0,0,0,-P2*kplus/sqrt(2),↙
P2*kz*sqrt(2/3),P2*kminus/sqrt(6),0,P2*kz/sqrt(3),P2*kminus/sqrt(3),0,0];
137          Hoffdiag(2,3:end) = [0,-P2d*kplus/sqrt(6),P2d*kz*sqrt(2/3),P2d*kminus/sqrt↙
(2),P2d*kplus/sqrt(3),-P2d*kz/sqrt(3),0,0,0,0,0,0,0,0,0,0,0,0,0,-P2*kplus/sqrt(6),↙
P2*kz*sqrt(2/3),P2*kminus/sqrt(2),P2*kplus/sqrt(3),-P2*kz/sqrt(3),0,0];
138          Hoffdiag(3,4:end) = [0,0,0,0,0,-P3d*kminus/sqrt(2),0,P3d*kplus*sqrt(3/2),↙
0,0,0,0,PXd*kplus/sqrt(3),PXd*kz/sqrt(3),0,PXd*kplus/sqrt(6),PXd*kz*sqrt(2/3),-↙
Pd*kminus/sqrt(2),0,0,0,0,0,0,0,0,0];
139          Hoffdiag(4,5:end) = [0,0,0,0,-P3d*kz*sqrt(8/3),-P3d*kminus/sqrt(6),0,↙
P3d*kplus/sqrt(2),0,0,-PXd*kminus/sqrt(3),0,0,PXd*kz/sqrt(3),0,-PXd*kplus/sqrt(2),↙
Pd*kz*sqrt(2/3),-Pd*kminus/sqrt(6),0,0,0,0,0,0,0,0,0];
140          Hoffdiag(5,6:end) = [0,0,0,P3d*kplus/sqrt(6),-P3d*kz*sqrt(8/3),-↙
P3d*kminus/sqrt(2),0,0,0,-PXd*kz/sqrt(3),0,0,-PXd*kplus/sqrt(3),PXd*kminus/sqrt(2),0,↙
Pd*kplus/sqrt(6),Pd*kz*sqrt(2/3),0,0,0,0,0,0,0,0];
141          Hoffdiag(6,7:end) = [0,0,0,P3d*kplus/sqrt(2),0,-P3d*kminus*sqrt(3/2),0,0,0,-↙
PXd*kz/sqrt(3),PXd*kminus/sqrt(3),0,PXd*kz*sqrt(2/3),-PXd*kminus/sqrt(6),0,Pd*kplus/sqrt↙
(2),0,0,0,0,0,0,0,0,0];
142          Hoffdiag(7,8:end) = [0,-P3d*kz*sqrt(4/3),P3d*kminus/sqrt(3),0,-P3d*kplus,↙
0,0,-PXd*kminus/sqrt(6),0,-PXd*kplus/sqrt(2),-PXd*kz*sqrt(2/3),0,0,Pd*kz/sqrt(3),↙
Pd*kminus/sqrt(3),0,0,0,0,0,0,0,0,0];
143          Hoffdiag(8,9:end) = [P3d*kplus/sqrt(3),P3d*kz*sqrt(4/3),-P3d*kminus,0,0,0,-↙
PXd*kz*sqrt(2/3),PXd*kminus/sqrt(2),0,PXd*kplus/sqrt(6),0,0,Pd*kplus/sqrt(3),-Pd*kz/sqrt↙
(3),0,0,0,0,0,0,0,0,0];
144          Hoffdiag(9,10:end) = [0,0,0,0,0,0,0,0,0,0,0,0,0,-P3*kplus/sqrt(2),-↙
```

```
P3*kz*sqrt(8/3),P3*kminus/sqrt(6),0,-P3*kz*sqrt(4/3),P3*kminus/sqrt(3),0,0];
145         Hoffdiag(10,11:end) = [0,0,0,0,0,0,0,0,0,0,0,0,-P3*kplus/sqrt(6),-↙
P3*kz*sqrt(8/3),P3*kminus/sqrt(2),P3*kplus/sqrt(3),P3*kz*sqrt(4/3),0,0];
146         Hoffdiag(11,12:end) = [0,0,0,0,0,0,0,0,0,0,0,P3*kminus*sqrt(3/2),0,-↙
P3*kplus/sqrt(2),0,0,-P3*kplus,0,0];
147         Hoffdiag(12,13:end) = [0,0,0,0,0,0,0,0,0,0,0,0,P3*kminus/sqrt(2),0,-↙
P3*kplus*sqrt(3/2),-P3*kminus,0,0,0];
148         Hoffdiag(13,14:end) = [0,-PU*kplus/sqrt(2),PU*kz*sqrt(2/3),PU*kminus/sqrt↙
(6),0,PU*kz/sqrt(3),PU*kminus/sqrt(3),0,0,0,0,0,0,0,0,0,0];
149         Hoffdiag(14,15:end) = [0,-PU*kplus/sqrt(6),PU*kz*sqrt(2/3),PU*kminus/sqrt↙
(2),PU*kplus/sqrt(3),-PU*kz/sqrt(3),0,0,0,0,0,0,0,0,0,0];
150         Hoffdiag(15,16:end) = [0,0,0,0,0,-P_prime*kminus/sqrt(2),0,d_prime/3,↙
PX*kplus/sqrt(3),PX*kz/sqrt(3),0,PX*kplus/sqrt(6),PX*kz*sqrt(2/3),-PS*kminus/sqrt(2),0];
151         Hoffdiag(16,17:end) = [0,0,0,0,P_prime*kz*sqrt(2/3),-P_prime*kminus/sqrt(6),↙
-PX*kminus/sqrt(3),d_prime/3,0,PX*kz/sqrt(3),0,-PX*kplus/sqrt(2),PS*kz*sqrt(2/3),-↙
PS*kminus/sqrt(6)];
152         Hoffdiag(17,18:end) = [0,0,0,P_prime*kplus/sqrt(6),P_prime*kz*sqrt(2/3),-↙
PX*kz/sqrt(3),0,d_prime/3,-PX*kplus/sqrt(3),PX*kminus/sqrt(2),0,PS*kplus/sqrt(6),↙
PS*kz*sqrt(2/3)];
153         Hoffdiag(18,19:end) = [0,0,0,P_prime*kplus/sqrt(2),0,-PX*kz/sqrt(3),↙
PX*kminus/sqrt(3),d_prime/3,PX*kz*sqrt(2/3),-PX*kminus/sqrt(6),0,PS*kplus/sqrt(2)];
154         Hoffdiag(19,20:end) = [0,P_prime*kz/sqrt(3),P_prime*kminus/sqrt(3),-↙
PX*kminus/sqrt(6),0,-PX*kplus/sqrt(2),-PX*kz*sqrt(2/3),-2*d_prime/3,0,PS*kz/sqrt(3),↙
PS*kminus/sqrt(3)];
155         Hoffdiag(20,21:end) = [P_prime*kplus/sqrt(3),-P_prime*kz/sqrt(3),-PX*kz*sqrt↙
(2/3),PX*kminus/sqrt(2),0,PX*kplus/sqrt(6),0,-2*d_prime/3,PS*kplus/sqrt(3),-PS*kz/sqrt↙
(3)];
156         Hoffdiag(21,22:end) = [0,-P*kplus/sqrt(2),P*kz*sqrt(2/3),P*kminus/sqrt(6),0,↙
P*kz/sqrt(3),P*kminus/sqrt(3),0,0];
157         Hoffdiag(22,23:end) = [0,-P*kplus/sqrt(6),P*kz*sqrt(2/3),P*kminus/sqrt(2),↙
P*kplus/sqrt(3),-P*kz/sqrt(3),0,0];
158         Hoffdiag(23,:) = zeros(1,30);
159         Hoffdiag(24,:) = zeros(1,30);
160         Hoffidag(25,:) = zeros(1,30);
161         Hoffdiag(26,:) = zeros(1,30);
162         Hoffdiag(27,:) = zeros(1,30);
163         Hoffdiag(28,:) = zeros(1,30);
164         Hoffdiag(29,:) = zeros(1,30);
165         Hoffdiag(30,:) = zeros(1,30);
166
167         Hoffdiag = transpose(conj(Hoffdiag))+Hoffdiag;
168         H = Hdiag + Hoffdiag + HEkdiag;
169         eval(['E',curr,'(:,i) = eig(H);']);
170         H = H*0;
171     end
172 end
```

B.5 Efield.m

```
% Name: Efield.m

% PURPOSE: This program evaluates the forward and backward fields in a
% layered structure given an normally incident TE wave on a layered
% structure where each layer may have a different refractive index and
% thickness. It then uses the calculated forward and backward fields in the
% scattering layer and the form of the bound solution of photoelastic
% scattering to compute the scattered field propagating backward from the
% first surface and forward from the last surface. It also computes the
% fields in each layer

% References:
% 1) Pettersson et. al., J. Appl. Phys., 86 (1), 487 (1999)
% 2) Bethune, J. Opt. Soc. Am. B, 6 (5), 910 (1989)
% 3) Hashizume, J. Opt. Soc. Am. B, 12 (10), 1894 (1995)

sample_thickness = '1150';
exp_number = '130509 and 130510';
data_name = '100df2';
sim_type = 'heterostructure';

EPS_save_path = ['/Users/ppadmana/Documents/Acoustic Plasmon Data and Simulations/Raman Data/',sample_thickness,'-A Experiments/',exp_number,'/Best Fits/APFits/EPS Figures/',data_name];
FIG_save_path = ['/Users/ppadmana/Documents/Acoustic Plasmon Data and Simulations/Raman Data/',sample_thickness,'-A Experiments/',exp_number,'/Best Fits/APFits/FIG Figures/',data_name];
model_report_save_path = ['/Users/ppadmana/Documents/Acoustic Plasmon Data and Simulations/Raman Data/',sample_thickness,'-A Experiments/',exp_number,'/Best Fits/APFits/',data_name,' (',sim_type,') - model report.txt'];

save_switch = 1;

hbar = 1.05e-34;
kb = 1.38e-23;
slabs = 1150e-10;
temperature = 120;

clearvars -except ii slabs peakvals modes hbar kb bars EPS_save_path sample_thickness exp_number data_name save_switch model_report_save_path sim_type temperature FIG_save_path test;
warning('off','MATLAB:plot:IgnoreImaginaryXYPart')


% MAIN DECLARATIONS
% ************************************************************************
% Define incoming wavelength (m), number of layers, and the index of the
% layer where the scattered field originates
l0 = 647e-9;
numlayers = 5;
NLlayer_index = 3;

% Use the following code to simulate my problem
a_string = 'a = (-1)^m;';  % This is used for my experiment
b_string = 'b = (-1)^m;';  % This is used for my experiment
%a_string = 'a = (-1)^m/2;';
%b_string = 'b = (-1)^m/2;';

% Use the following code to compare to Loudon
%a_string = 'a = 1;';
%b_string = 'b = 0;';

% Use the following code to compare to Groenen
%a_string = 'a = 1/(2*1i)*sqrt(hbar/(2*2330*wm))*(-1)^(m-1)*qm;';
%b_string = 'b = -1/(2*1i)*sqrt(hbar/(2*2330*wm))*(-1)^(m-1)*qm;';

% Define wavevector,frequency, and max mode order of the plasmon and
% scattered wavelength
qm_string = 'qm = m*pi/d(NLlayer_index);';
%wm_string = 'wm = m*2*pi*3e10*4.6;';   % This is used to compare to Groenen
wm_string = 'wm = qm*4.126e-07*3e10*2*pi;';   % This is used for my experiment
ws_string = 'ws = wi-wm;';
mnumber = 10;

% Constants and frequency to incident field
c = 3e8;
eps0 = 8.85e-12;
wi = 2*pi*c/l0;

% Define complex refractive indices and wave vectors
n_GaAs = 3.76 + 1i*0.18;
n_AlAs = 3.11;
```

```
n_AlGaAs = 3.24;
n_Si = 5.222 + 1i*0.269;
k_GaAs = 2*pi*n_GaAs/l0;
k_AlAs = 2*pi*n_AlAs/l0;
k_AlGaAs = 2*pi*n_AlGaAs/l0;
k_Si = 2*pi*n_Si/l0;

% Define layer thicknesses and layer refractive indices and computer
% associated wave vectors and absorption coefficients
%n0 = n_SiO2;
n01 = 1;
n02 = n_GaAs;
k01 = 2*pi*n01/l0;
k02 = 2*pi*n02/l0;
d = [80e-10 100e-10 slabs(1) 500e-10 2000e-10];
n = [n_GaAs n_AlAs n_GaAs n_AlAs n_AlGaAs];
%n = n_GaAs;
p0 = [0 0 1 0 0];
%p0 = 1;
k = 2*pi*n/l0;
alpha = 4*pi*imag(n)/l0;


% COMPUTE PROFILE OF INPUT FIELD
% ************************************************************************
% Compute transfer and propgation matrices for the input field, which for
% the base of Brilluoin scattering, will be the same matrices for the
% scattered field (frequencies are nearly identical)

Iholder = cell(1,numlayers+1);
rholder = cell(1,numlayers+1);
tholder = cell(1,numlayers+1);
I = zeros(2,2,numlayers+1);
L = zeros(2,2,numlayers);
Sp = zeros(2,2,numlayers);
Spp = zeros(2,2,numlayers);

% Compute layer reflection/transmission (r,t) coefficients and matrices (I)
for i = 1:numlayers+1
    if i == 1
        eval(['r01=','(n01 - n(1))/(n01+n(1));']);
        eval(['t01=','2*n01/(n01+n(1));']);
    elseif i == numlayers+1
        eval(['r',num2str(i-1),num2str(i),'=','(n(',num2str(i-1),')-n02)/(n(',num2str(i-1),')+n02);'])
        eval(['t',num2str(i-1),num2str(i),'=','2*n(',num2str(i-1),')/(n(',num2str(i-1),')+n02);'])
    else
        eval(['r',num2str(i-1),num2str(i),'=','(n(',num2str(i-1),')-n(',num2str(i),'))/(n(',num2str(i-1),')+n(',num2str(i),'));'])
        eval(['t',num2str(i-1),num2str(i),'=','2*n(',num2str(i-1),')/(n(',num2str(i-1),')+n(',num2str(i),'));'])
    end

    eval(['I',num2str(i-1),num2str(i),'=[1 r',num2str(i-1),num2str(i),';r',num2str(i-1),num2str(i),' 1]/t',num2str(i-1),num2str(i),';'])
    eval(['I(:,:,',num2str(i),')=I',num2str(i-1),num2str(i),';'])

    rholder(i) = {['r',num2str(i-1),num2str(i)]};
    tholder(i) = {['t',num2str(i-1),num2str(i)]};
    Iholder(i) = {['I',num2str(i-1),num2str(i)]};
end

% Compute propagation matrices (L)
Lholder = cell(1,numlayers);
for i = 1:numlayers
    eval(['L',num2str(i),'=[exp(-1i*k(',num2str(i),')*d(',num2str(i),')) 0;0 exp(1i*k(',num2str(i),')*d(',num2str(i),'))];']);
    Lholder(i) = {['L',num2str(i)]};
    eval(['L(:,:,',num2str(i),')=L',num2str(i),';'])
end

% Compute scattering matrices (total (S) and intermediate (Sip and Sipp))
S_string = 'S=(1';
for i = 1:numlayers
    S_string = strcat(S_string,'*',Iholder(i),'*',Lholder(i));
end
S_string = strcat(S_string,')*',Iholder(end),';');
eval(cell2mat(S_string))
T = inv(S);
r = -T(2,1)/T(2,2);
t = 1/S(1,1);
```

```
151
152 S1p = I01;
153 Sp(:,:,1) = I01;
154 for i = 2:numlayers
155     Sp_string = '(1';
156     for j = 1:i-1
157         Sp_string = strcat(Sp_string,'*',Iholder(j),'*',Lholder(j));
158     end
159     Sp_string = strcat(Sp_string,')*',Iholder(i));
160     evalexp = cell2mat(strcat('S',num2str(i),'p=',Sp_string,';'));
161     eval(evalexp)
162     eval(['Sp(:,:,',num2str(i),')=S',num2str(i),'p;'])
163 end
164
165 for i = 1:numlayers-1
166     Spp_string = '(1';
167     for j = i+1:numlayers
168         Spp_string = strcat(Spp_string,'*',Iholder(j),'*',Lholder(j));
169     end
170     Spp_string = strcat(Spp_string,')*',Iholder(end));
171     evalexp = cell2mat(strcat('S',num2str(i),'pp=',Spp_string,';'));
172     eval(evalexp)
173     eval(['Spp(:,:,',num2str(i),')=S',num2str(i),'pp;'])
174 end
175 eval(['S',num2str(numlayers),'pp = I',num2str(numlayers),num2str(numlayers+1),';'])
176 eval(['Spp(:,:,',num2str(numlayers),')=S',num2str(numlayers),'pp;'])
177
178 % Evaluate fields and plot
179 E0_plus = 1;
180 z0 = -5000e-10:(5000e-10)/100:0;
181 Z0 = z0;
182 E0_minus = E0_plus*r*exp(-1i*k01*z0);
183 zend=0:(6000e-10)/100:6000e-10;
184 eval(['E',num2str(numlayers+1),'=E0_plus/S(1,1)*exp(1i*k02*zend);'])
185
186 z = 0;
187 for i = 1:numlayers
188     eval(['z = z + z',num2str(i-1),'(end);'])
189     eval(['z',num2str(i),'=0:d(',num2str(i),')/100:d(',num2str(i),');'])
190     eval(['Z',num2str(i),'=z(end) + z',num2str(i),';'])
191     eval(['zcurrent=z',num2str(i),';'])
192     A = E0_plus*(Spp(1,1,i)*exp(-1i*k(i)*(d(i)))./(Sp(1,1,i)*Spp(1,1,i)*exp(-1i*k↙
(i)*d(i))+Sp(1,2,i)*Spp(2,1,i)*exp(1i*k(i)*d(i)));
193     Ef = A*exp(1i*k(i)*zcurrent);
194     B = E0_plus*(Spp(2,1,i)*exp(1i*k(i)*(d(i)))./(Sp(1,1,i)*Spp(1,1,i)*exp(-1i*k(i)↙
*d(i))+Sp(1,2,i)*Spp(2,1,i)*exp(1i*k(i)*d(i)));
195     Eb = B*exp(-1i*k(i)*zcurrent);
196     eval(['E',num2str(i),'=Ef+Eb;'])
197     eval(['Ef',num2str(i),'=Ef;'])
198     eval(['Eb',num2str(i),'=Eb;'])
199     eval(['A',num2str(i),'=A;'])
200     eval(['B',num2str(i),'=B;'])
201 end
202 eval(['Zend=Z',num2str(numlayers),'(end)+zend;'])
203 clear E;
204
205 hold on;
206 f1=figure(1);
207 lineheight = 1;
208 for i=1:numlayers
209     eval(['plot(Z',num2str(i),',Ef',num2str(i),',',char(39),'--b',char↙
(39),',''LineWidth'',2);'])
210     eval(['plot(Z',num2str(i),',Eb',num2str(i),',',char(39),'-.g',char↙
(39),',''LineWidth'',2);'])
211     eval(['plot(Z',num2str(i),',abs(E',num2str(i),'),',char(39),'-r',char↙
(39),',''LineWidth'',2);'])
212     legend('|E|^2','|E^+|^2','|E^-|^2')
213     eval(['line([Z',num2str(i),'(1),Z',num2str(i),'(1)]',',[-lineheight,↙
2*lineheight],',char(39),'LineStyle',char(39),',',char(39),':',char(39),',',char↙
(39),'Color',char(39),',',char(39),'k',char(39),')'])
214 end
215 line([Zend(1),Zend(1)],[-lineheight,2*lineheight],'LineStyle',':','Color','k')
216 box on;
217 xlabel('z (m)')
218 ylabel('\itNormalized |E|^2')
219 title('\itInput field intensity \rm(arb. units)')
220 plot(z0,abs(E0_plus*exp(1i*k01*z0)+E0_plus*r*exp(-1i*k01*z0)),'-r','LineWidth',2)
221 eval(['plot(Zend,abs(E0_plus*t*exp(1i*k02*zend)),',char(39),'-r',char↙
(39),',''LineWidth'',2)'])
222 hold off;
223
224
```

```
% COMPUTE SCATTERED FIELD PROFILE - BETHUNE METHOD
% ************************************************************************
% Compute bound scattered wave amplitudes from photoelastic polarization of
% layer j assuming PNL = p0*uj*Ej where
% uj = a*exp(i*qm*zj) + b*exp(-i*qm*zj) and Ej = Ej_plus + Ej_minus

Ejout0 = zeros(2,2,mnumber);
Ejout = zeros(2,2,numlayers,mnumber);
F = zeros(2,2,numlayers,mnumber);       % Holds source amplitudes for each layer
Fp = zeros(2,2,numlayers,mnumber);      % Prime of F
FscatterVmT = zeros(1,mnumber);
BscatterVmT = zeros(1,mnumber);
FscatterVm = zeros(2,mnumber);
BscatterVm = zeros(2,mnumber);

% Constants to particular solution
for m = 1:mnumber;
    eval(qm_string);
    eval(wm_string);
    eval(ws_string);
    eval(a_string);
    eval(b_string);
    eval(['A=A',num2str(NLlayer_index),';'])
    eval(['B=B',num2str(NLlayer_index),';'])

    % Free wave index and wave vector
    kj = 2*pi*n(NLlayer_index)/l0;        % Wave vector of driving wave
    nj = n(NLlayer_index);                % Index of photoelastic layer
    ksj = ws*n(NLlayer_index)/c;          % Wave vector of Stokes free wave
    ks = ws*n/c;

    % Bound wave index and wave vector
    K1 = kj + qm;                         % Wave vector of Stokes bound wave
    ns1 = c*K1/ws;                        % Psuedo-index associated with bound wave
    K2 = kj - qm;
    ns2 = c*K2/ws;

    % Bound wave amplitudes
    Ap = (-p0(NLlayer_index)*ws^2/(eps0*c^2))*a*A/(ksj^2-(K1)^2);
    Bp = (-p0(NLlayer_index)*ws^2/(eps0*c^2))*b*B/(ksj^2-(K1)^2);
    Cp = (-p0(NLlayer_index)*ws^2/(eps0*c^2))*b*A/(ksj^2-(K2)^2);
    Dp = (-p0(NLlayer_index)*ws^2/(eps0*c^2))*a*B/(ksj^2-(K2)^2);

    % Matrix of source (bound) wave amplitdues in each layer
    Es10 = [0;0];
    Es20 = [0;0];
    Es1 = zeros(2,numlayers+1);
    Es2 = zeros(2,numlayers+1);
    Es1(:,NLlayer_index) = [Ap;Bp];
    Es2(:,NLlayer_index) = [Cp;Dp];

    % Psuedo reflection and transmission amplitudes and interface matrix for NL↙
layer
    rs1 = (nj-ns1)/(nj+ns1);
    ts1 = 2*nj/(nj+ns1);
    Is10 = zeros(2,2);
    Is1 = zeros(2,2,numlayers+1);
    Is1(:,:,NLlayer_index) = (1/ts1)*[1 rs1;rs1 1];

    rs2 = (nj-ns2)/(nj+ns2);
    ts2 = 2*nj/(nj+ns2);
    Is20 = zeros(2,2);
    Is2 = zeros(2,2,numlayers+1);
    Is2(:,:,NLlayer_index) = (1/ts2)*[1 rs2;rs2 1];

    % Calculate psuedo-propagation matrix for NL layer
    Ls1 = zeros(2,2,numlayers);
    Ls2 = zeros(2,2,numlayers);

    for i = 1:numlayers
        Ls1(:,:,i) = [exp(-1i*K1*d(i)) 0;0 exp(1i*K1*d(i))];
        Ls2(:,:,i) = [exp(-1i*K2*d(i)) 0;0 exp(1i*K2*d(i))];
    end

    % Main loop to compute left-edge free stokes-wave amplitudes
    E = zeros(2,1,numlayers+1);     % Holds forward and backward pump field↙
amplitude at left edge of each layer interface
    E0 = [1;r]*E0_plus;             % Forward and backward pumop field amplitude and↙
first interface (ambient/sample)
    G00 = [1 0;0 1];
    G0 = zeros(2,2,numlayers+1);
    F0(:,1) = Is10*Es10;
```

```
304     F0(:,2) = Is20*Es20;
305     Fp0(:,1) = G00*F0(:,1);
306     Fp0(:,2) = G00*F0(:,2);
307
308     for j = 1:2
309         eval(['Is=Is',num2str(j),';'])
310         eval(['Es=Es',num2str(j),';'])
311         eval(['Ls=Ls',num2str(j),';'])
312         for i = 1:numlayers+1
313             % Calculate the field on the left-hand side of each interface
314             if i == 1
315                 E(:,1,i) = I(:,:,i)\[1 0;0 1]*E0;
316             else
317                 E(:,1,i) = inv(I(:,:,i))*inv(L(:,:,i-1))*E(:,1,i-1);
318             end
319
320             % Calculate source amplitude matrix (F)
321             if i == numlayers + 1
322                 F(:,j,i,m) = -Is(:,:,i)*Es(:,i);
323             else
324                 F(:,j,i,m) = (L(:,:,i)*Is(:,:,i)*inv(Ls(:,:,i))-Is(:,:,i))*Es(:,i);
325             end
326
327             % Calculate Gj1 matrices (G0)
328             if i == 1
329                 G0(:,:,i) = I(:,:,i);
330             else
331                 G0(:,:,i) = G0(:,:,i-1)*L(:,:,i-1)*I(:,:,i);
332             end
333
334             % Calculate F-prime (Fp)1
335             Fp(:,j,i,m) = G0(:,:,i)*F(:,j,i,m);
336         end
337
338         Ejout0(:,j,m) = (1/G0(1,1,end))*[1 0;G0(2,1,end) -G0(1,1,end)]*Fp0(:,j);
339         for i = 1:numlayers+1
340             Ejout(:,j,i,m) = (1/G0(1,1,end))*[1 0;G0(2,1,end) -G0(1,1,end)]*Fp(:,j,↙
i,m);
341         end
342     end
343
344     BscatterVm(1,m) = Ejout(2,1,NLlayer_index,m);
345     FscatterVm(1,m) = Ejout(1,1,NLlayer_index,m);
346     BscatterVm(2,m) = Ejout(2,2,NLlayer_index,m);
347     FscatterVm(2,m) = Ejout(1,2,NLlayer_index,m);
348
349     BscatterVmT(m) = Ejout(2,1,NLlayer_index,m)+Ejout(2,2,NLlayer_index,m);
350     FscatterVmT(m) = Ejout(1,1,NLlayer_index,m)+Ejout(1,2,NLlayer_index,m);
351 end
352
353
354 % h2 = figure(2)
355 % plot(1:mnumber,abs(BscatterVmT).^2,1:mnumber,20*abs(FscatterVmT).^2)
356 % xlabel('Mode Order (m)')
357 % ylabel('arb. units')
358 % title('Forward and backward scattered field')
359 % legend('Forward','Bacward')
360
361
362
363
364
365
366 % COMPUTE SCATTERED FIELD PROFILE - HASHIZUME METHOD
367 % **********************************************************************
368 % Use the Hashizume method to calculate scattered field profiles within the
369 % multilayer structure
370
371 part = ['a','b'];
372 source = zeros(2,1,numlayers,mnumber);
373
374 for i = 1:numlayers
375     eval(['Zcurrent=Z',num2str(i),';'])
376     eval(['ES',num2str(i),' = zeros(2,length(Zcurrent),',num2str(mnumber),');'])
377 end
378
379 for m = 1:mnumber
380     eval(qm_string);
381     eval(wm_string);
382     eval(ws_string);
383     eval(a_string);
384     eval(b_string);
```

```
385     %qm = m*pi/d(NLlayer_index);
386     %wm = m*0.02e12;
387     %ws = wi-wm;
388     %a = -1/(2*1i);%1/(2*1);
389     %b = 1/(2*1i);%1/(2*1);
390     k01s = ws*n01/c;
391     k02s = ws*n02/c;
392
393     % Free wave index and wave vector
394     kj = 2*pi*n(NLlayer_index)/l0;        % Wave vector of driving wave
395     nj = n(NLlayer_index);                % Index of photoelastic layer
396     ksj = ws*n(NLlayer_index)/c;          % Wave vector of Stokes free wave
397     ks = ws*n/c;
398
399     % Bound wave index and wave vector
400     K1 = kj + qm;                         % Wave vector of Stokes bound wave
401     ns1 = c*K1/ws;                        % Psuedo-index associated with bound wave
402     K2 = kj - qm;
403     ns2 = c*K2/ws;
404
405     % Define nonlinear polarization function
406     for i = 1:numlayers
407         eval(['PNL',num2str(i),'a_p = @(zp) (p0(',num2str(i),')*a*A*exp(1i*(kj+qm)*zp) + p0(',num2str(i),')*b*B*exp(-1i*(kj+qm)*zp)).*exp(-1i*ks(',num2str(i),')*zp);'])
408         eval(['PNL',num2str(i),'a_m = @(zp) (p0(',num2str(i),')*a*A*exp(1i*(kj+qm)*zp) + p0(',num2str(i),')*b*B*exp(-1i*(kj+qm)*zp)).*exp(1i*ks(',num2str(i),')*zp);'])
409
410         eval(['PNL',num2str(i),'b_p = @(zp) (p0(',num2str(i),')*b*A*exp(1i*(kj-qm)*zp) + p0(',num2str(i),')*a*B*exp(-1i*(kj-qm)*zp)).*exp(-1i*ks(',num2str(i),')*zp);'])
411         eval(['PNL',num2str(i),'b_m = @(zp) (p0(',num2str(i),')*b*A*exp(1i*(kj-qm)*zp) + p0(',num2str(i),')*a*B*exp(-1i*(kj-qm)*zp)).*exp(1i*ks(',num2str(i),')*zp);'])
412     end
413
414     % Compute E_r (E_self = E_r + E_b)
415     for j = 1:numlayers
416         eval(['zcurrent=z',num2str(j),';'])
417         Era_p = zeros(length(zcurrent),1);
418         Era_m = zeros(length(zcurrent),1);
419         for i = 1:length(zcurrent)
420             eval(['Era_p(i) = (1i*ws^2/(2*eps0*c^2*ks(',num2str(j),')))*integral(PNL',num2str(j),'a_p,zcurrent(1),zcurrent(i))*exp(1i*k(',num2str(j),')*zcurrent(i));'])
421             eval(['Era_m(i) = (1i*ws^2/(2*eps0*c^2*ks(',num2str(j),')))*integral(PNL',num2str(j),'a_m,zcurrent(i),zcurrent(end))*exp(-1i*k(',num2str(j),')*zcurrent(i));'])
422             eval(['Erb_p(i) = (1i*ws^2/(2*eps0*c^2*ks(',num2str(j),')))*integral(PNL',num2str(j),'b_p,zcurrent(1),zcurrent(i))*exp(1i*k(',num2str(j),')*zcurrent(i));'])
423             eval(['Erb_m(i) = (1i*ws^2/(2*eps0*c^2*ks(',num2str(j),')))*integral(PNL',num2str(j),'b_m,zcurrent(i),zcurrent(end))*exp(-1i*k(',num2str(j),')*zcurrent(i));'])
424         end
425         eval(['E',num2str(j),'ra_p(',num2str(m),',:)=Era_p;'])
426         eval(['E',num2str(j),'ra_m(',num2str(m),',:)=Era_m;'])
427         eval(['E',num2str(j),'rb_p(',num2str(m),',:)=Erb_p;'])
428         eval(['E',num2str(j),'rb_m(',num2str(m),',:)=Erb_m;'])
429     end
430
431     % Compute source vector
432     for i = 1:numlayers
433         eval(['source_temp1 = [E',num2str(i),'ra_p(',num2str(m),',end);E',num2str(i),'ra_m(',num2str(m),',end)] - inv(L',num2str(i),')*[E',num2str(i),'ra_p(',num2str(m),',1);E',num2str(i),'ra_m(',num2str(m),',1)];'])
434         eval(['source_temp2 = [E',num2str(i),'rb_p(',num2str(m),',end);E',num2str(i),'rb_m(',num2str(m),',end)] - inv(L',num2str(i),')*[E',num2str(i),'rb_p(',num2str(m),',1);E',num2str(i),'rb_m(',num2str(m),',1)];'])
435
436         % source(fourward_or_backward,PNL_sourceterm,layer_index,m_value)
437         eval(['source(:,1,',num2str(i),',',num2str(m),')=source_temp1;'])
438         eval(['source(:,2,',num2str(i),',',num2str(m),')=source_temp2;'])
439     end
440
441     % Compute scattered waves for each layer
442     clear ES
443     EScurrent = zeros(2,length(Zcurrent));
444     for j=1:2
445         ES0 = [0; BscatterVm(j,m)];
446         eval(['ES',num2str(numlayers+1),'=[FscatterVm(j,m);0];'])
447         for i=1:numlayers
448             eval(['Zcurrent=Z',num2str(i),';'])
449             eval(['Tcurrent=inv(S',num2str(i),'p);'])
450
451             % Compute SiL
452             term1 = 0;
```

```
453             eval(['Eir = [E',num2str(i),'r',part(j),'_p(',num2str(m),',1);E',num2str(i),'r',part(j),'_m(',num2str(m),',1)];'])
454             term2 = -Eir;
455             if i<=3
456                 term3 = [0;0];
457             else
458                 term3 = [0;0];
459                 for h=1:i-1
460                     term3 = term3 + Sp(:,:,i)\Sp(:,:,h)*L(:,:,h)*source(:,j,h,m);
461                 end
462             end
463             SiLcurrent = term1 + term2 + term3;
464
465             for zj = 1:length(Zcurrent)
466                 Lcurrent = [exp(-1i*k(i)*(Zcurrent(zj)-Zcurrent(1))) 0;0 exp(1i*k(i)*(Zcurrent(zj)-Zcurrent(1)))];
467                 Tcurrent = Sp(:,:,i)\eye(size(Sp(:,:,i)));
468                 EScurrent(:,zj) = Lcurrent\(Tcurrent*ES0+SiLcurrent);
469             end
470
471             eval(['ES',num2str(i),'(:,:,',num2str(j),',',num2str(m),')=EScurrent;'])
472         end
473     end
474 end
475
476 % Plot additional and self fields and intensities for a specific mode order
477 % h3=figure(3);
478 % mplot = 2;
479 % sourceplot = 2;
480 % hold on;
481 % lineheight = 1;
482 % for i=1:numlayers
483 %     % Plot forward "add" wave
484 %     eval(['plot(Z',num2str(i),',ES',num2str(i),'(1,:,',num2str(sourceplot),',',num2str(mplot),'),',char(39),'-b',char(39),',',char(39),'LineWidth',char(39),',2);'])
485 %
486 %     % Plot backward "add" wave
487 %     eval(['plot(Z',num2str(i),',ES',num2str(i),'(2,:,',num2str(sourceplot),',',num2str(mplot),'),',char(39),'-g',char(39),',',char(39),'LineWidth',char(39),',2);'])
488 %
489 %     % Plot forward "r" component of "self" wave
490 %     eval(['plot(Z',num2str(i),',E',num2str(i),'r',part(sourceplot),'_p(',num2str(mplot),',:),',char(39),'--b',char(39),');'])
491 %
492 %     % Plot backward "r" component of "self" wave
493 %     eval(['plot(Z',num2str(i),',E',num2str(i),'r',part(sourceplot),'_m(',num2str(mplot),',:),',char(39),'--g',char(39),');'])
494 %
495 %     % Plot forward "b" component of "self" wave
496 %     %eval(['plot(Z',num2str(i),',E',num2str(i),'b',part(sourceplot),'_p(',num2str(mplot),',:),',char(39),'.-b',char(39),');'])
497 %
498 %     % Plot backward "b" component of "self" wave
499 %     %eval(['plot(Z',num2str(i),',E',num2str(i),'b',part(sourceplot),'_m(',num2str(mplot),',:),',char(39),'.-g',char(39),');'])
500 %
501 %     legend('E_S^a^d^d^,^+','E_S^a^d^d^,^-','E_S^r^,^+','E_S^r^,^-','E_S^b^,^+','E_S^b^,^-')
502 %
503 %     %eval(['line([Z',num2str(i),'(1),Z',num2str(i),'(1)]',',[-1,1],',char(39),'LineStyle',char(39),',',char(39),':',char(39),',',char(39),'Color',char(39),',',char(39),'k',char(39),')'])
504 % end
505 % box on;
506 % title(['Additional and Self (r-comp.) Electric Fields for m=',num2str(mplot)])
507 % xlabel('z (m)')
508 % ylabel('E')
509 % hold off;
510
511
512 % Plot total squared scattered field for specific mode order
513 % h4 = figure(4);
514 % eval(['ymax=','max(abs(ES',num2str(NLlayer_index),'(1,:,',num2str(sourceplot),',',num2str(mplot),')+ES',num2str(NLlayer_index),'(2,:,',num2str(sourceplot),',',num2str(mplot),')+E',num2str(NLlayer_index),'r',part(sourceplot),'_p(',num2str(mplot),',:)+E',num2str(NLlayer_index),'r',part(sourceplot),'_m(',num2str(mplot),',:)).^2);'])
515 % hold on;
516 % for i=1:numlayers
517 %     % Plot total |E|^2 (adds "self" and "add" waves)
518 %     eval(['plot(Z',num2str(i),',abs(ES',num2str(i),'(1,:,',num2str(sourceplot),',',num2str(mplot),')+ES',num2str(i),'(2,:,',num2str(sourceplot),',',num2str(mplot),')+E',num2str(i),'r',part(sourceplot),'_p(',num2str(mplot),',:)+E',
```

```
num2str(i),'r',part(sourceplot),'_m(',num2str(mplot),',:)).^2,',char(39),'-r',char↙
(39),',',char(39),'LineWidth',char(39),',2);'])
%
%     legend('|E_S^T|^2')
%
%     eval(['line([Z',num2str(i),'(1),Z',num2str(i),'(1)]',',[0,ymax],',char↙
(39),'LineStyle',char(39),',',char(39),':',char(39),',',char(39),'Color',char(39),',',↙
char(39),'k',char(39),')'])
% end
% line([Zend(1),Zend(1)],[0,ymax],'LineStyle',':','Color','k')
% plot(Z0,abs(BscatterVm(sourceplot,mplot)*exp(-1i*k01s*Z0)).^2,'-r','LineWidth',2);
% plot(Zend,abs(FscatterVm(sourceplot,mplot)*exp(1i*k02s*zend)).^2,'-r','LineWidth',↙
2);
% box on;
% title(['Total Squared Field for m=',num2str(mplot)])
% xlabel('z (m)')
% ylabel('Normalized |E|^2')
% eval('axis([Z0(1) Zend(end) 0 ymax])')
% hold off


f5 = figure(5);
hold on
color = ['b' 'g' 'r' 'c' 'm' 'y' 'k' 'b' 'g' 'r' 'c' 'm' 'y' 'k' 'b' 'g' 'r' 'c' 'm'↙
'y' 'k'];
color = repmat(color,1,50);
clear ES0;
ES = zeros(2,101,numlayers+1,mnumber);
ESa = zeros(2,101,numlayers+1,mnumber);
ESb = zeros(2,101,numlayers+1,mnumber);
ES0 = zeros(2,101,mnumber);
ES0a = zeros(2,101,mnumber);
ES0b = zeros(2,101,mnumber);

for m = 1:mnumber
    for i=1:numlayers
        % Plot total |E| (adds "self" and "add" waves)

        % Compute total E-field for source term 1 (A) and source term 2 (B)
        % for layer i: ESx(forward or backward,z_value,layer_index,m_value)
        eval(['ESa(1,:,',num2str(i),',',num2str(m),')=ES',num2str(i),'(1,:,1,',↙
num2str(m),')+E',num2str(i),'ra_p','(',num2str(m),',:);'])
        eval(['ESa(2,:,',num2str(i),',',num2str(m),')=ES',num2str(i),'(2,:,1,',↙
num2str(m),')+E',num2str(i),'ra_m','(',num2str(m),',:);'])
        eval(['ESb(1,:,',num2str(i),',',num2str(m),')=ES',num2str(i),'(1,:,2,',↙
num2str(m),')+E',num2str(i),'rb_p','(',num2str(m),',:);'])
        eval(['ESb(2,:,',num2str(i),',',num2str(m),')=ES',num2str(i),'(2,:,2,',↙
num2str(m),')+E',num2str(i),'rb_m','(',num2str(m),',:);'])
        %eval(['ESb(:,',num2str(i),',',num2str(m),')=ES',num2str(i),'(1,:,2,',↙
num2str(m),')+ES',num2str(i),'(2,:,2,',num2str(m),')+E',num2str(i),'rb_p','(',num2str↙
(m),',:)+E',num2str(i),'rb_m','(',num2str(m),',:);'])

        % Compute total E-field for forward (1) and backward (2) waves for
        % layer i: ES(forward or backward,z_value,layer_index,m_value)
         eval(['ES(1,:,',num2str(i),',',num2str(m),')=ES',num2str(i),'(1,:,1,',↙
num2str(m),')+ES',num2str(i),'(1,:,2,',num2str(m),')+E',num2str(i),'ra_p','(',num2str↙
(m),',:)+E',num2str(i),'rb_p','(',num2str(m),',:);'])
         eval(['ES(2,:,',num2str(i),',',num2str(m),')=ES',num2str(i),'(2,:,1,',↙
num2str(m),')+ES',num2str(i),'(2,:,2,',num2str(m),')+E',num2str(i),'ra_m','(',num2str↙
(m),',:)+E',num2str(i),'rb_m','(',num2str(m),',:);'])
          %eval(['ES(1,:,',num2str(i),',',num2str(m),')=ES',num2str(i),'(1,:,1,',↙
num2str(m),')+ES',num2str(i),'(1,:,2,',num2str(m),')+E',num2str(i),'ra_p','(',num2str↙
(m),',:)+E',num2str(i),'rb_p','(',num2str(m),',:)+E',num2str(i),'ba_p','(',num2str↙
(m),',:)+E',num2str(i),'bb_p','(',num2str(m),',:);'])
          %eval(['ES(2,:,',num2str(i),',',num2str(m),')=ES',num2str(i),'(2,:,1,',↙
num2str(m),')+ES',num2str(i),'(2,:,2,',num2str(m),')+E',num2str(i),'ra_m','(',num2str↙
(m),',:)+E',num2str(i),'rb_m','(',num2str(m),',:)+E',num2str(i),'ba_m','(',num2str↙
(m),',:)+E',num2str(i),'bb_m','(',num2str(m),',:);'])

        % Compute total E-field in layer i
        eval(['EST(:,',num2str(i),',',num2str(m),')=ES(1,:,',num2str(i),',',num2str↙
(m),')+ES(2,:,',num2str(i),',',num2str(m),');'])

        %eval(['plot(Z',num2str(i),',abs(EST',num2str(i),'(:,',num2str(m),')).^2,',↙
char(39),'-',color(m),char(39),',',char(39),'LineWidth',char(39),',2);'])
        eval(['plot(Z',num2str(i),',abs(EST(:,',num2str(i),',',num2str(m),')),',char↙
(39),'-',color(m),char(39),',',char(39),'LineWidth',char(39),',2);'])

        eval(['line([Z',num2str(i),'(1),Z',num2str(i),'(1)]',',[0,1.2*max(max(max↙
(abs(EST(:,:,:))))],',char(39),'LineStyle',char(39),',',char(39),':',char(39),',',char↙
(39),'Color',char(39),',',char(39),'k',char(39),')'])
    end
```

```
574
575     ES(1,1:length(zend),numlayers+1,m) = FscatterVmT(m)*exp(1i*k02s*zend);
576     ES(2,1:length(zend),numlayers+1,m) = 0*exp(1i*k02s*zend);
577     ESa(1,1:length(zend),numlayers+1,m) = FscatterVm(1,m)*exp(1i*k02s*zend);
578     ESa(2,1:length(zend),numlayers+1,m) = 0*exp(1i*k02s*zend);
579     ESb(1,1:length(zend),numlayers+1,m) = FscatterVm(2,m)*exp(1i*k02s*zend);
580     ESb(2,1:length(zend),numlayers+1,m) = 0*exp(1i*k02s*zend);
581
582     ES0(1,1:length(z0),m) = 0*exp(1i*k01s*z0);
583     ES0(2,1:length(z0),m) = BscatterVmT(m)*exp(1i*k01s*z0);
584     ES0a(1,1:length(z0),m) = BscatterVm(1,m)*exp(1i*k01s*z0);
585     ES0a(2,1:length(z0),m) = 0*exp(1i*k01s*z0);
586     ES0b(1,1:length(z0),m) = BscatterVm(2,m)*exp(1i*k01s*z0);
587     ES0b(2,1:length(z0),m) = 0*exp(1i*k01s*z0);
588
589     plot(Z0,abs(ES0(2,1:length(z0),m)+ES0(1,1:length(z0),m)),strcat('-',color(m)))
590     plot(Zend,abs(ES(2,1:length(zend),numlayers+1,m)+ES(1,1:length(zend),↙
numlayers+1,m)),strcat('-',color(m)))
591 end
592 line([Zend(1),Zend(1)],[0,1.2*max(max(max(abs(EST↙
(:,:,:))))))],'LineStyle','':'','Color','k')
593 box on;
594 title('Absolute Value of Field')
595 xlabel('\itz \rm(m)')
596 ylabel('\itNormalized |E_S| \rm(arb. units)')
597 eval('axis([-0.25e-7 d(end)+0.25e-7 0 1.2*max(max(max(abs(EST(:,:,:))))))])')
598 hold off
599
600
601 % COMPUTE WEIGHTING FACTORS FOR SCATTERING CROSS SECTIONS
602 % ************************************************************************
603 clear Eif;
604 clear Eib;
605 eval(['z=z',num2str(NLlayer_index),';'])
606 eval(['Eif=Ef',num2str(NLlayer_index),';'])
607 eval(['Eib=Eb',num2str(NLlayer_index),';'])
608 eval(['dz=z',num2str(NLlayer_index),'(2)-z',num2str(NLlayer_index),'(1);'])
609 for m = 1:mnumber
610     eval(qm_string);
611     eval(wm_string);
612     eval(ws_string);
613     eval(a_string);
614     eval(b_string);
615
616     functi1 = (Eif+Eib).*conj(ES(1,:,NLlayer_index,m)).*(a*exp(1i*qm*z)+b*exp(-1↙
i*qm*z));
617     functi2 = (Eif+Eib).*conj(ES(2,:,NLlayer_index,m)).*(a*exp(1i*qm*z)+b*exp(-1↙
i*qm*z));
618     y1(m) = trapz(functi1);
619     y2(m) = trapz(functi2);
620     bose(m) = (1/(exp(hbar*wm/(kb*temperature))-1))+1;
621     %plot(m,y,color(m))
622 end
623 %figure(6)
624 %bar(1:mnumber,bose.*abs(dz*y1).^2,0.4,'b')
625 %title('Scattering Efficiency (FS)')
626 %xlabel('m')
627 %figure(7)
628 %bar(1:mnumber,bose.*abs(dz*y2).^2,0.4,'g')
629 %title('Scattering Efficiency (BS)')
630 %xlabel('m')
631 f8 = figure(8);
632 %bar(1:mnumber,bose.'.*abs(squeeze(ES0(2,31,:))).^2,0.4,'g')
633 bar(1:mnumber,abs(squeeze(ES0(2,31,:))).^2,0.4,'g')
634     xlabel('\itMode order')
635     ylabel('\itScattering intensity \rm(arb. units)')
636     title('Backward Scattering')
637     xlim([0 mnumber+0.5])
638 f9 = figure(9);
639 %bar(1:mnumber,bose.'.*abs(squeeze(ES(1,1,end,:))).^2,0.4,'b')
640 bar(1:mnumber,abs(squeeze(ES(1,1,end,:))).^2,0.4,'b')
641     xlabel('\itMode order')
642     ylabel('\itScattering intensity \rm(arb. units)')
643     title('Forward Scattering')
644     xlim([0 mnumber+0.5])
645
646 weight_B = abs(squeeze(ES0(2,31,:))).^2;
647 weight_F = abs(squeeze(ES(1,1,end,:))).^2;
648
649 weight_B = weight_B/sum(weight_B);
650 weight_F = weight_F/sum(weight_F);
651
```

```
652 end
653 beep
654
655 if save_switch == 1
656     export_fig(f1,[EPS_save_path,'/',data_name,' (',sim_type,') - ','Incident Field.↙
eps'],'-eps','-transparent','-nocrop')
657     export_fig(f5,[EPS_save_path,'/',data_name,' (',sim_type,') - ','Scattered Field↙
Abs Val.eps'],'-eps','-transparent','-nocrop')
658     export_fig(f8,[EPS_save_path,'/',data_name,' (',sim_type,') - ','Back Scatter.↙
eps'],'-eps','-transparent','-nocrop')
659     export_fig(f9,[EPS_save_path,'/',data_name,' (',sim_type,') - ','Forward↙
Scatter.eps'],'-eps','-transparent','-nocrop')
660
661     saveas(f1,[FIG_save_path,'/',data_name,' (',sim_type,') - ','Incident Field.↙
fig'],'fig');
662     saveas(f5,[FIG_save_path,'/',data_name,' (',sim_type,') - ','Scattered Field Abs↙
Val.fig'],'fig');
663     saveas(f8,[FIG_save_path,'/',data_name,' (',sim_type,') - ','Back Scatter.↙
fig'],'fig');
664     saveas(f9,[FIG_save_path,'/',data_name,' (',sim_type,') - ','Forward Scatter.↙
fig'],'fig');
665
666     model_report{1} = ['Sample Thickness = ',sample_thickness,'-A'];
667     model_report{2} = ['Experiment = ',exp_number];
668     model_report{3} = ['Data Name = ',data_name];
669     model_report{4} = ['Simulation type = ',sim_type];
670     model_report{5} = ['Wavelength = ',num2str(l0)];
671     model_report{6} = a_string;
672     model_report{7} = b_string;
673     model_report{8} = qm_string;
674     model_report{9} = wm_string;
675     model_report{10} = ['Temperature = ',num2str(temperature)];
676
677     FID = fopen(model_report_save_path,'w+');
678     fprintf(FID,'%s\n',model_report{:});
679     fclose(FID);
680 end
681
682
683 % Use this code if you want to check single layer on substrate with Loudon
684 % results (from Alburqueque et. al 1979)
685 % ************************************************************************
686 % ks2 = ws*n02/c;
687 % ks = ws*n/c;
688 % ks0 = ws*n01/c;
689 %
690 % P1 = 1./((ks-ks2)*(ks-ks0)*exp(2*1i*ks*d(1))-(ks+ks2)*(ks+ks0));
691 % P21 = ks0^2*A1/(eps0*((qm+k(1))^2-ks^2));
692 % P31 = (ks-ks2)*(qm+k(1)+ks)*(exp(2*1i*ks*d(1))-exp(1i*(qm+k(1)+ks)*d(1)));
693 % P41 = (ks+ks2)*(qm+k(1)-ks)*(1-exp(1i*(qm+k(1)+ks)*d(1)));
694 % P1*(P21*(P31+P41))
695
696
697 % n_ITO = 1.7203 + 1i*0.01206;
698 % n_SiO2 = 1.4496;
699 % n_PEDOT = 1.44317 + 1i*0.05748;
700 % n_P3 = 2.05 + 1i*0.04808154;
701 % n_Ca = 2.45 + 1i*2.5413;
702 % n_Al = 1.45625 + 1i*7.76198;
703
704 %n = [n_ITO n_PEDOT n_P3 n_Ca n_Al n_Al];
```

Bibliography

[1] C. V. Raman and K. S. Krishnan. A New Type of Secondary Radiation. *Nature*, 121(3048):501–502, March 1928.

[2] G. Abstreiter, M. Cardona, and A. Pinczuk. Light Scattering by Free Carrier Excitations in Semiconductors. In Manuel Cardona and Gernot Guntherodt, editors, *Light Scattering in Solids IV*, chapter 2, pages 5–150. Springer-Verlag, New York, 1 edition, 1984.

[3] G. Abstreiter, R. Trommer, M. Cardona, and A. Pinczuk. Coupled plasmon-LO phonon modes and Lindhard-Mermin dielectric function of n-GaAs. *Solid State Communications*, 30(11):703–707, June 1979.

[4] A. Mooradian and A. McWhorter. Polarization and Intensity of Raman Scattering from Plasmons and Phonons in Gallium Arsenide. *Physical Review Letters*, 19(15):849–852, October 1967.

[5] A. Mooradian and G. Wright. Observation of the Interaction of Plasmons with Longitudinal Optical Phonons in GaAs. *Physical Review Letters*, 16(22):999–1001, May 1966.

[6] R. Kersting, J. N. Heyman, G. Strasser, and K. Unterrainer. Coherent plasmons in n-doped GaAs. *Physical Review B*, 58(8):4553–4559, 1998.

[7] M. Hase, S. Nakashima, K. Mizoguchi, H. Harima, and K. Sakai. Ultrafast decay of coherent plasmon-phonon coupled modes in highly doped GaAs. *Physical Review B*, 60(24):526–530, 1999.

[8] G. C. Cho, T. Dekorsy, H. J. Bakker, R. Hövel, and H. Kurz. Generation and Relaxation of Coherent Majority Plasmons. *Physical Review Letters*, 77(19):4062–4065, November 1996.

[9] M. P. Hasselbeck, L. A. Schlie, and D. Stalnaker. Coherent plasmons in InSb. *Applied Physics Letters*, 85(25):6116, 2004.

[10] P. Nozières and D. Pines. Electron Interaction in Solids. The Nature of the Elementary Excitations. *Physical Review*, 109(4):1062–1074, February 1958.

[11] J. Ruvalds. Are there acoustic plasmons? *Advances in Physics*, 30(5):677–695, October 1981.

[12] O. Entin-Wohlman and H. Gutfreund. Acoustic plasmons and superconductivity. I. The role of exchange. *Journal of Physics C: Solid State Physics*, 17(6):1071–1084, February 1984.

[13] J. Ruvalds and L. M. Kahn. Superconductivity in A-15 compounds. *Physics Letters A*, 70(5-6):477–479, April 1979.

[14] Y. Ishii and J. Ruvalds. Acoustic plasmons and cuprate superconductivity. *Physical Review B*, 48(5):3455–3463, August 1993.

[15] A. Bill, H. Morawitz, and V. Z. Kresin. Acoustic Plasmons in Layered Systems and the Phonon-Plasmon Mechanism of Superconductivity. *Journal of Low Temperature Physics*, 117(3/4):283–287, 1999.

[16] P. Longe and S. M. Bose. Acoustic plasmon exchange in multilayered systems: II. application to high-T c superconductors. *Journal of Physics: Condensed Matter*, 4(7):1811–1818, February 1992.

[17] G. Canright and G. Vignale. Superconductivity and acoustic plasmons in the two-dimensional electron gas. *Physical Review B*, 39(4):2740–2743, February 1989.

[18] G. Santoro and G. Giuliani. Acoustic plasmons in a conducting double layer. *Physical Review B*, 37(2):937–940, January 1988.

[19] A. Pinczuk, J. Shah, and P. Wolff. Collective Modes of Photoexcited Electron-Hole Plasmas in GaAs. *Physical Review Letters*, 47(20):1487–1490, November 1981.

[20] B. Diaconescu, K. Pohl, L. Vattuone, L. Savio, P. Hofmann, V. M. Silkin, J. M. Pitarke, E. V. Chulkov, P. M. Echenique, D. Farías, and M. Rocca. Low-energy acoustic plasmons at metal surfaces. *Nature*, 448(7149):57–9, July 2007.

[21] K. Pohl, B. Diaconescu, G. Vercelli, L. Vattuone, V. M. Silkin, E. V. Chulkov, P. M. Echenique, and M. Rocca. Acoustic surface plasmon on Cu(111). *EPL (Europhysics Letters)*, 90(5):57006, June 2010.

[22] S. Ji. Park and R. E. Palmer. Acoustic Plasmon on the Au(111) Surface. *Physical Review Letters*, 105(1):016801, July 2010.

[23] A. Politano, A. R. Marino, V. Formoso, D. Farías, R. Miranda, and G. Chiarello. Evidence for acoustic-like plasmons on epitaxial graphene on Pt(111). *Physical Review B*, 84(3):033401, July 2011.

[24] J. Pitarke, V. Nazarov, V. Silkin, E. Chulkov, E. Zaremba, and P. Echenique. Theory of acoustic surface plasmons. *Physical Review B*, 70(20):205403, November 2004.

[25] L. M. Jiji. *Heat Conduction*. Springer Berlin Heidelberg, Berlin, 3rd edition, 2009.

[26] J. D. Jackson. *Classcial Electrodynamics*. John Wiley & Sons, Inc., 3rd edition, 1999.

[27] D. Pines. *Elementary excitations in solids*. Perseus, Reading, 3rd edition, 1999.

[28] J. Sólyom. Electronic response to external perturbations. In *Fundamentals of the Physics of Solids Volume 3 - Normal, Broken-Symmetry, and Correlated Systems*, pages 61–138. Springer Berlin Heidelberg, Berlin, Heidelberg, 2010.

[29] N. Mermin. Lindhard Dielectric Function in the Relaxation-Time Approximation. *Physical Review B*, 1(5):2362–2363, March 1970.

[30] G. F. Bertsch and R. A. Broglia. Line boradening and the decay of oscillations. In *Oscillations in Finite Quantum Systems*, chapter 9, pages 148–170. Cambridge University Press, Cambridge, 1st edition, 2005.

[31] M. Combescot and P. Nozières. Condensation of excitons in germanium and silicon. *Journal of Physics C: Solid State Physics*, 5(17):2369–2391, September 1972.

[32] M. Combescot and P. Nozières. The dielectric constant and plasma frequency of p-type Ge like semiconductors. *Solid State Communications*, 10(3):301–305, February 1972.

[33] J. Young and P. Kelly. Many-body treatment of hot-electron scattering from quasiequilibrium electron-hole plasmas and coupled plasmon-longitudinal-optic-phonon modes in GaAs. *Physical Review B*, 47(11):6316–6329, March 1993.

[34] W. Bardyszewski. The dielectric function of holes in semiconductors of zinc-blende structure. *Solid State Communications*, 57(11):873–876, March 1986.

[35] R. J. Goldston and P. H. Rutherford. *Introduction to Plasma Physics, Volume 1*. Institute of Physics Publishing, Bristol, 4th edition, 1995.

[36] D. Gammon, B. Shanabrook, and D. Katzer. Excitons, phonons, and interfaces in GaAs/AlAs quantum-well structures. *Physical Review Letters*, 67(12):1547–1550, September 1991.

[37] W. Hayes and R. Loudon. *Scattering of Light by Crystals*. John Wiley & Sons, New York, 1st edition, 1978.

[38] M. V. Klein. Electronic Raman Scattering. In Manuel Cardona, editor, *Light Scattering in Solids VIII*, volume 8, chapter Ch 4, pages 147–204. Springer, Berlin, 1975.

[39] S. Chen and M. Kotlarchyk. Time-Dependent Perturbation Theory, Transition Probabilities, and Scattering. In *Interaction of Photons and Neutrons With Matter: An Introduction*, chapter 6, pages 165–186. World Scientific Pub Co Inc, Singapore, 1 edition, 1998.

[40] P. M. Platzman and P. A. Wolff. *Waves and interactions in solid state plasmas*. Academic Press, New York, 1st edition, 1973.

[41] H. Callen and T. Welton. Irreversibility and Generalized Noise. *Physical Review*, 83(1):34–40, July 1951.

[42] R. Loudon. Theory of lineshapes for normal-incidence Brillouin scattering by acoustic phonons. *Journal of Physics C: Solid State Physics*, 11(2):403–417, January 1978.

[43] R. Kubo. The fluctuation-dissipation theorem. *Reports on Progress in Physics*, 29(1):255–284, January 1966.

[44] P. Platzman. Incoherent Scattering of Light from Anisotropic Degenerate Plasmas. *Physical Review*, 139(2A):A379–A387, July 1965.

[45] F. Blum. Inelastic Light Scattering from Semiconductor Plasmas in a Magnetic Field. *Physical Review B*, 1(3):1125–1135, February 1970.

[46] D. C. Hamilton and A. L. McWhorter. Raman Scattering from Spin-Density Fluctuations in n-GaAs. In George B. Wright, editor, *Light Scattering Spectra of Solids*, chapter 4, pages 309–316. Springer-Verlag, Berlin, 1st edition, 1969.

[47] B. Varga. Coupling of Plasmons to Polar Phonons in Degenerate Semiconductors. *Physical Review*, 137(6A):A1896–A1902, March 1965.

[48] P. Y. Yu and M. Cardona. *Fundamentals of Semiconductors*. Springer-Verlag, New York, 4th edition, 2010.

[49] H. Nather and L. G. Quagliano. Inelastic light scattering in highly excited GaAs. *Journal of Luminescence*, 30(1-4):50–64, February 1985.

[50] A. Pinczuk, G. Abstreiter, R. Trommer, and M. Cardona. Resonance enhancement of Raman scattering by electron-gas excitations of n-GaAs. *Solid State Communications*, 30(7):429–432, May 1979.

[51] A. Pinczuk, L. Brillson, E. Burstein, and E. Anastassakis. Resonant Light Scattering by Single-Particle Electronic Excitations in n-GaAs. *Physical Review Letters*, 27(6):317–320, August 1971.

[52] M. Cardona. Folded, confined, interface, surface, and slab vibrational modes in semiconductor superlattices. *Superlattices and Microstructures*, 5(1):27–42, January 1989.

[53] S. Richard, F. Aniel, and G. Fishman. Energy-band structure of Ge, Si, and GaAs: A thirty-band kp method. *Physical Review B*, 70(23):235204, December 2004.

[54] L. C. Lew Yan Voon and M. Willatzen. *The k.p method*. Springer Berlin Heidelberg, Berlin, 1st edition, 2009.

[55] O. Jepson and O. K. Anderson. The electronic structure of h.c.p. Ytterbium. *Solid State Communications*, 9(20):1763–1767, October 1971.

[56] P. E. Blöchl. Improved tetrahedron method for Brillouin-zone integrations. *Physical Review B*, 49(23):16223–16233, June 1994.

[57] O. V. Yazyev, E. N. Brothers, K. N. Kudin, and G. E. Scuseria. A finite temperature linear tetrahedron method for electronic structure calculations of periodic systems. *The Journal of chemical physics*, 121(6):2466–70, August 2004.

[58] Mathworks. integral2, 2013.

[59] G. Dresselhaus, A. Kip, and C. Kittel. Cyclotron Resonance of Electrons and Holes in Silicon and Germanium Crystals. *Physical Review*, 98(2):368–384, April 1955.

[60] N. Nintunze and M. A. Osman. Hole drift velocity in the warped band model of GaAs. *Semiconductor Science and Technology*, 10(1):11–17, January 1995.

[61] E. G. Marason. Laser dye DCM: CW, synchronously pumped, cavity pumped and single-frequency performance. *Optics Communications*, 37(1):56–58, April 1981.

[62] Coherent. *Operator's Manual: The Coherent Mira Seed Laser*. Coherent, Santa Clara, 2002.

[63] Coherent. *Operators Manual: RegA 9050 Modelocked Laser*. Coherent, Santa Clara, 2002.

[64] T. B. Norris. Femtosecond pulse amplification at 250 kHz with a Ti:sapphire regenerative amplifier and application to continuum generation. *Optics Letters*, 17(14):1009, July 1992.

[65] Coherent. *Operator's Manual: The Coherent Model 9800/9850 Optical Parametric Amplifier (OPA)*. Coherent, Santa Clara, 2002.

[66] M. K. Reed, M. K. Steiner-Shepard, and D. K. Negus. Widely tunable femtosecond optical parametric amplifier at 250 kHz with a Ti:sapphire regenerative amplifier. *Optics Letters*, 19(22):1855, 1994.

[67] R. Boyd. *Nonlinear Optics*. Academic Press, Amsterdam, 3rd edition, 2008.

[68] J. Armstrong, N. Bloembergen, J. Ducuing, and P. Pershan. Interactions between Light Waves in a Nonlinear Dielectric. *Physical Review*, 127(6):1918–1939, September 1962.

[69] A. Monmayrant, S. Weber, and B. Chatel. A newcomer's guide to ultrashort pulse shaping and characterization. *Journal of Physics B: Atomic, Molecular and Optical Physics*, 43(10):103001, May 2010.

[70] D. J. Kane and R. Trebino. Characterization of arbitrary femtosecond pulses using frequency-resolved optical gating. *IEEE Journal of Quantum Electronics*, 29(2):571–579, 1993.

[71] O. Svelto. Transient Laser Behavior. In *Principles of Lasers*, chapter 8. Springer US, Boston, MA, 2010.

[72] J. Li, J. Chen, D. A. Reis, S. Fahy, and R. Merlin. Optical Probing of Ultrafast Electronic Decay in Bi and Sb with Slow Phonons. *Physical Review Letters*, 110(4):047401, January 2013.

[73] D. Wang, Y. Ren, X. Liu, J. Furdyna, M. Grimsditch, and R. Merlin. Light-induced magnetic precession in (Ga,Mn)As slabs: Hybrid standing-wave Damon-Eshbach modes. *Physical Review B*, 75(23):233308, June 2007.

[74] J. Zhao, A. Bragas, D. Lockwood, and R. Merlin. Magnon Squeezing in an Antiferromagnet: Reducing the Spin Noise below the Standard Quantum Limit. *Physical Review Letters*, 93(10):107203, September 2004.

[75] T. E. Stevens, J. K. Wahlstrand, J. Kuhl, and R. Merlin. Cherenkov radiation at speeds below the light threshold: phonon-assisted phase matching. *Science (New York, N.Y.)*, 291(5504):627–30, January 2001.

[76] A. Bartels, T. Dekorsy, H. Kurz, and K. Kohler. Coherent control of acoustic phonons in semiconductor superlattices. *Applied Physics Letters*, 72(22):2844, 1998.

[77] R. Merlin. Generating coherent THz phonons with light pulses. *Solid State Communications*, 102(2):207–220, 1997.

[78] D. L. Mills and K. R. Subbaswamy. Surface and Size Effects on the Light Scattering Spectra of Solids. In E. Wolf, editor, *Progress in Optics, Voume 19*, chapter 2. North Holland Publishing Company, Amsterdam, 1981.

[79] M. Trigo, A. Fainstein, B. Jusserand, and V. Thierry-Mieg. Finite-size effects on acoustic phonons in GaAs/AlAs superlattices. *Physical Review B*, 66(12):125311, September 2002.

[80] J. Groenen, F. Poinsotte, A. Zwick, C. Sotomayor Torres, M. Prunnila, and J. Ahopelto. Inelastic light scattering by longitudinal acoustic phonons in thin silicon layers: From membranes to silicon-on-insulator structures. *Physical Review B*, 77(4):045420, January 2008.

[81] C. M. S. Torres, A. Zwick, F. Poinsotte, J. Groenen, M. Prunnila, J. Ahopelto, A. Mlayah, and V. Paillard. Observations of confined acoustic phonons in silicon membranes. *Physica Status Solidi (C)*, 1(11):2609–2612, November 2004.

[82] J. He, B. Djafari-Rouhani, and J. Sapriel. Theory of light scattering by longitudinal-acoustic phonons in superlattices. *Physical Review B*, 37(8):4086–4098, March 1988.

[83] T. Figielski. Photostriction Effect in Germanium. *physica status solidi (b)*, 1(4):306–316, 1961.

[84] L. A. A. Pettersson, L. S. Roman, and O. Inganas. Modeling photocurrent action spectra of photovoltaic devices based on organic thin films. *Journal of Applied Physics*, 86(1):487, 1999.

[85] D. S. Bethune. Optical harmonic generation and mixing in multilayer media: analysis using optical transfer matrix techniques. *Journal of the Optical Society of America B*, 6(5):910, May 1989.

[86] N. Hashizume, M. Ohashi, T. Kondo, and R. Ito. Optical harmonic generation in multilayered structures: a comprehensive analysis. *Journal of the Optical Society of America B*, 12(10):1894, October 1995.

[87] J. E. Sipe. New Green-function formalism for surface optics. *Journal of the Optical Society of America B*, 4(4):481, April 1987.

[88] D. Strauch and B. Dorner. Phonon dispersion in GaAs. *Journal of Physics: Condensed Matter*, 2(6):1457–1474, February 1990.

[89] Y. Yan, E. B Gamble, and K. A. Nelson. Impulsive stimulated scattering: General importance in femtosecond laser pulse interactions with matter, and spectroscopic applications. *The Journal of Chemical Physics*, 83(11):5391, 1985.

[90] T. E. Stevens. *Ultrafast dynamics of low energy elementary excitations in semiconductors*. PhD thesis, University of Michigan, 2000.

[91] T. Stevens, J. Kuhl, and R. Merlin. Coherent phonon generation and the two stimulated Raman tensors. *Physical Review B*, 65(14):144304, March 2002.

[92] T. Pfeifer, T. Dekorsy, W. Kütt, and H. Kurz. Generation mechanism for coherent LO phonons in surface-space-charge fields of III-V-compounds. *Applied Physics A Solids and Surfaces*, 55(5):482–488, November 1992.

[93] A. Sabbah and D. Riffe. Femtosecond pump-probe reflectivity study of silicon carrier dynamics. *Physical Review B*, 66(16):1–11, October 2002.

[94] D. Kim and P. Yu. Hot-electron relaxations and hot phonons in GaAs studied by subpicosecond Raman scattering. *Physical Review B*, 43(5):4158–4169, February 1991.

[95] K. Singwi and M. Tosi. Interaction of Plasmons and Optical Phonons in Degenerate Semiconductors. *Physical Review*, 147(2):658–662, July 1966.

[96] A. Kuznetsov and C. Stanton. Coherent phonon oscillations in GaAs. *Physical Review B*, 51(12):7555–7565, March 1995.

[97] K. El Sayed, R. Binder, D. Scott, and S. Koch. Undamping of acoustic plasmons in nonequilibrium plasmas. *Physical Review B*, 47(16):10210–10216, April 1993.

[98] D. Scott, R. Binder, M. Bonitz, and S. Koch. Multiple undamped acoustic plasmons in three-dimensional two-component nonequilibrium plasmas. *Physical Review B*, 49(3):2174–2176, January 1994.

[99] P. M. Donaldson, H. Strzalka, and P. Hamm. High sensitivity transient infrared spectroscopy: a UV/Visible transient grating spectrometer with a heterodyne detected infrared probe. *Optics express*, 20(12):12761–70, June 2012.

[100] K. Ishioka, A. K. Basak, and H. Petek. Allowed and forbidden Raman scattering mechanisms for detection of coherent LO phonon and plasmon-coupled modes in GaAs. *Physical Review B*, 84(23):235202, December 2011.